University of Alberta

A Rich New Approach to Determining the Structure and Dynamics of the Milky Way Galaxy

by

Tyler J. Foster 

A thesis submitted to the Faculty of Graduate Studies and Research in partial fulfillment of the requirements for the degree of Doctor of Philosophy

Department of Physics

Edmonton, Alberta
Spring 2004

Your file Votre référence
ISBN: 0-612-96266-0
Our file Notre référence
ISBN: 0-612-96266-0

Abstract

This work will present a new method aimed toward explaining long-standing and foundational problems in Galactic astronomy that descend from the uncertain dynamics in the Galaxy's second quadrant. The overall method is based on a mathematical model of the cumulative H I column density with Galactocentric radius. This model, when confronted with radio-wavelength H I data from the Canadian Galactic Plane Survey (CGPS), is successful in reproducing the large-scale distribution of H I in the Galactic disk. The method's cardinal technique is the fitting of the model to the observational data. This step provides three fundamental outputs for a given direction: the predicted run of neutral hydrogen column density with distance, the relationship between velocity and distance (the velocity field), and parameters that describe the smooth large-scale structure of the Milky Way's thin H I disk. This thesis begins by fully developing and describing the method. The method's accuracy as a distance indicator for individual astronomical objects is tested, and new distances are derived for 30 H II regions in the Galactic plane across the second quadrant, in the range $90° \leq \ell \leq 140°$. The method's importance to studies of astronomical objects is demonstrated in the second part (Chapters 3 and 4), where new reddenings and distances to a collection of objects near ℓ=93 ° are calculated, and are shown to be nearly one-half of those predicted from Galactic kinematics. The astrophysical characteristics of the supernova remnant 3C434.1 and its surrounding H I shell that descend from a proper distance calculation are presented. The fifth chapter exhibits the method's ability to predict the velocity field in a given direction. Selected velocity fields from across the CGPS Phase I ($90° \leq \ell \leq 140°$)

are derived. General characteristics of the H I velocity fields are consistent with a falling rotation curve combined with the effects of a spiral arm potential ascribed to the Perseus Arm. The magnitude of the field's deviation from flat circular rotation is observed to have a strong latitude dependence, and probably arises due to non-axisymmetric motions induced by the Perseus Spiral Arm. The thesis concludes with a look at future research directions.

"I hope I die before I get old." -The Who, 1965

Acknowledgements

This work is a testimony to the company and counsel of people with whom I am fortunate to be involved. Dr. David Routledge is always supportive: from finance for travel opportunities and equipment, to allowing my independence, to offering his patience, friendship and understanding. Dr. Tom Landecker has encouraged and supported my work in a similarly exceptional manner. These persons' words of praise and interest in my research are flattering and very much appreciated. I cannot express how fortunate I feel to have had these honorable people guide me in their role as a supervisory team.

Dr. Douglas Hube's continued friendship through the years and trust is dear to me, and Dr. Brian Martin's years of encouragement, sound advice and friendship have positively influenced me personally and professionally. I can truly say this thesis would not have come to be without these two people in my life. Dr. Sharon Morsink has always welcomed my theoretical questions with a smile and a thoughtful answer, and her wisdom in all practical matters that a student must attend to was valuable.

Albert Van Steenbergen's brilliant computer skills have saved me many hours of unnecessary labor, and his steadfast friendship is important to me. The staff of DRAO were always gracious and helpful. Charles Kerton, Chris Brunt and Lewis Knee made me feel like a colleague and important member of the team. Their incredible mastery of their fields are the finest resources I have had available to me. In particular, Roland Kothes' encouragement and expertise have been constant and have helped guide me into academic maturity. His friendship will always be valued.

My friend Ian Blokland patiently shared his enviable knowledge and talent for theoretical physics with me. My father's support is important to me. Finally, Marie's love and patience are inspiring of confidence and success.

Table of Contents

List of Tables

List of Figures

List of Symbols and Abbreviations

α, δ (J2000)	Right ascension & declination for 2000.0
$'$	Angular measurement unit in arcminutes
$''$	Angular measurement unit in arcseconds
^{12}CO	λ =2.6 mm (ν=115.3 GHz) line from $^{12}C^{16}O$
Σ-D	Radio surface brightness vs diameter relation
A_V	Extinction in V-band magnitudes
CCD	Charge-Coupled Device
CGPS	Canadian Galactic Plane Survey
Copernicus	Ultraviolet-band orbiting astronomical observatory
DRAO	Dominion Radio Astrophysical Observatory
$E(B-V)$	Colour excess, or reddening (magnitudes)
EM	Emission measure (cm^{-6} pc)
FBS	Reference to Fich, Blitz, & Stark (1989, ApJ, 342, 272)
FCRAO	Five Colleges Radio Astronomy Observatory
FWHM	Full-Width at Half Maximum
$H\alpha$, $H\beta$	Optical H recombination lines (Balmer series)
$H158\alpha$	Radio H (ν=1651.541 MHz) recombination line
H I	Neutral hydrogen
H II	Ionized hydrogen
H_2	Molecular hydrogen
HISA	Neutral hydrogen (H I) Self Absorption
HIPPARCOS	Stellar parallax orbiting observatory
IR	Infrared
IRAS	Infrared Astronomical Satellite
IRAF	Image Reduction & Analysis Facility software
ISM	Interstellar Medium

Jy	Jansky unit (10^{-26} W m^{-2} Hz^{-1})
keV	10^3 electron-volts
kpc	10^3 parsecs
$L_\odot$	Solar luminosity
LC	Stellar Luminosity Class
LOS	Line of sight
$M_\odot$	Solar mass
mag	Unit of magnitude
mJy	10^{-3} Jansky
MSX	Midcourse Space Experiment IR satellite
Myr	10^6 years
N II	Ionized nitrogen
n	Number density (cm^{-3})
NRAO	National Radio Astronomy Observatories (United States)
OB	Stellar spectral classes O & B
pc	Unit of parsec
PROS	Post-Reduction Off-line Software for X-ray data analysis
PSF	Point Spread Function
PSPC	Position Sensitive Proportion Counter detector aboard ROSAT
R_0	Distance of Sun from Galactic centre (kpc)
ROSAT	Roentgen Satellite orbiting X-ray observatory
Sh	Sharpless' designation of optical H II region
SNR	Supernova Remnant
ST	DRAO Synthesis Telescope
SWB	Stellar Wind Bubble
TASS	Two-Armed Spiral Shock model of Roberts (1972)
UBV	Photometric colour system (Johnson & Morgan, 1953, ApJ, 117)
UV	Ultraviolet
V	Visual magnitude in UBV system
V	Luminosity Class V (main sequence)
X	Airmass
$Z_\odot$	Height of Sun above Galactic midplane (pc)

Chapter 1

Introduction

1.1 Tracing the Neutral Hydrogen Through the Outer Galaxy

This work presents the author's invention of a new technique that allows one to obtain much useful information about the Galaxy's structure and motions. With it, one may calculate distances to objects in the Galactic plane, determine the functional relation between line of sight (LOS) velocity and distance, and model the density distribution of Galactic neutral hydrogen (H I). The technique was created out of the author's knowledge of optical and radio astronomical techniques, and was originally based on stellar distances and reddenings (e.g. Gathier, Pottasch, & Pel 1978). Many long evenings were spent observing deep fields toward distant objects which needed a distance measure, before it was discovered that extending the reddening-distance relation to large distances ($\geq$2 kpc) with stellar observations was impossible (due to the Malmquist bias). Observations were traded for a model of the reddening-distance relation that assumed a flat, uniform-density disk of dust. This model initially proved too simplistic for directions into the Galactic midplane, and was completely reworked to account for symmetric and asymmetric components (e.g. the warp) of the complex H I disk. The new model of column density versus distance was found to be very comparable to observed H I-velocity spectra, and a multiple parameter χ^2-minimization procedure produced excellent fits. The fitting achieves two things: a distance measurement for any object with a known LOS velocity, and a fitted model of large-scale Galactic structure as traced by H I.

The entire technique has been named simply "the distance method" by my colleagues, as our mutual need for an accurate astronomical distance tool is what spurred the method's development and boosted its popularity. The name is sound, and the reader will see that the method at its heart is a mass model of Galactic H I and its rotation, that happens to be capable of calculating distances to individual objects. The writing follows a practical philosophy, one that offers the reader enough detail to apply the method in their own research and reproduce the results herein.

The usefulness of a multi-wavelength approach to astronomical study, particularly in combining optical and radio observations of objects, is demonstrated

in this thesis as well. In the early phases of its development the distance method was a truly multi-wavelength recipe, which calculated distances using extinction due to Galactic dust. This dust was traced using Canadian Galactic Plane Survey (CGPS) 21 centimetre-wave radio continuum and line data, millimetre-wave ^{12}CO line data from the Columbia ^{12}CO survey (Dame et al. 2001) and the Five Colleges Radio Astronomy Observatory Outer Galaxy Survey (FCRAO, Heyer et al. 1998), the author's own broadband (UBV) and narrowband ($H\alpha$,$H\beta$) optical observations, and the infrared dust maps of Schlegel et al. (1998). A multi-wavelength approach is more necessary and profitable as astronomical research confronts increasingly complex problems. Still, publications of research on radio objects seldom include an optical component, or even attempts at optical observations. The success of the study herein shows that this broad approach should be taken more often, and that an individual astronomer need not specialize in a single window of the wide electromagentic spectrum showering our planet.

The modern distance method has been distilled down to a kernel of modeling the H I distribution through the large-scale thin-disk component of H I in the Galaxy. H I emission in data from the Canadian Galactic Plane Survey (CGPS, Taylor et al. 2003) is used in the method. The CGPS is an international collaboration to map all of the major interstellar components of the Milky Way at a common resolution: neutral atomic gas, molecular gas, ionized gas, dust grains, and relativistic plasma. For many of these constituents, angular resolution is improved over previous studies by more than a factor of 10. The principal goal of the project is astrophysical research into all the major ISM components that make up our Galaxy by the creation of a database of panoramic, high resolution images. The basis of this survey is the $\sim$1′ angular resolution mosaics of radio continuum and line data produced at the Dominion Radio Astrophysical Observatory (DRAO). Astronomers at the DRAO and a consortium of astronomers from universities across Canada have completed two phases of observations for the CGPS. The first covers Galactic longitudes[1] $74.2° \leq \ell \leq 147.3°$, and extends in latitude $-3.6° \leq b \leq +5.6°$ at 1420 MHz, and $-6.7° \leq b \leq +8.7°$ at 408 MHz. The second phase extends Phase I limits to ℓ=63° (lower longitude end) and ℓ=175°

[1]For definitions of longitude ℓ and latitude b see Figure 1.1.

(higher longitude end), and adds a high-latitude rectangle $100° \leq \ell \leq 117°$ that reaches to b=18°. Detailed plans for Phase III observations have already been made.

1.2 Motivation

The business of applying mathematical models to explain observations and structure of the Galaxy is very active in the field of astrophysics today. Excellent models of many Galactic constituents have appeared in the literature. A dust distribution model fit to far infrared (240 μm) observations comes from Drimmel & Spergel (2001). This model has recently been extended to predict the extinction to any point in the Galactic disk (Drimmel et al. 2003), as many prior models of interstellar extinction are designed to do (e.g. Hakkila et al. 1997, Méndez & van Altena 1998, and Chen et al. 1999). A model of the distribution of free electrons fitted to pulsar dispersion measures and Galactic H II regions comes from Taylor & Cordes (1993), and more recently Cordes & Lazio (2002). The neutral hydrogen distribution in the inner Galaxy ($R < R_0$) was modeled by Malhotra (1995), while that in the outer Galaxy was published by Diplas & Savage in 1991. A two-component (spheroidal bulge/halo, and disk) mathematical model was fit to star-counts by Ortiz & Lépine (1993), and a more recent synthetic model of the stellar population in the Galactic disk comes from Robin et al. (2003).

1.2.1 Background

The above summarizes a selection of models of the Milky Way disk. A dependence common to all previous attempts at modeling the observed 21 cm H I distribution is that they rely on a pre-existing method of distance calculation. For the inner Galaxy, Malhotra (1995) makes use of emission at the tangent points, from which the Galactocentric distance is straightforwardly $R = R_0 sin(\ell)$. The work of Diplas & Savage (1991), the three-dimensional model of Nakanishi & Sofue (2003), and most other attempts at determining the distribution of H I in the outer Galaxy rely on the *kinematic method of distance calculation*, which pre-

supposes knowledge of the Galactic rotation curve. Merrifield (1992) solves for the parameterized distance R/R_0 using the variation in apparent thickness of the H I layer from direction to direction at constant radii. There has been *no* research published on H I distribution models of the Milky Way that does not rely on distance methods other than these.

Figure 1.1 graphically illustrates some conventions and terminology used throughout this thesis. The Sun rotates with velocity θ_0 about the Galactic centre, which is located R_0 kiloparsecs (kpc) towards $\ell = 0°$. The LOS velocity of an object a distance r from the Sun (Galactic coordinates R, ℓ, b and purely circular orbital velocity $\theta(R)$) is defined as the LOS velocity component of θ minus that of θ_0:

$$\begin{aligned} v_{obj} &= (\theta(R)\, cos(\pi/2 - \ell - \phi) - \theta_0 cos(\pi/2 - \ell))\, cos(b) \\ &= (\theta(R)\, (sin(\phi)\, cos(\ell) + cos(\phi)\, sin(\ell)) - \theta_0 sin(\ell))\, cos(b) \end{aligned} \tag{1.1}$$

Notice in Fig. 1.1 that $r cos(\pi/2 - \ell) = r sin(\ell) = R sin(\phi)$, and also that $R cos(\phi) = R_0 - r cos(\ell)$, so that Eqn. 1.1 becomes:

$$v_{obj} = R_0 \left(\frac{\theta(R)}{R} - \frac{\theta_0}{R_0} \right) sin(\ell)\, cos(b) \tag{1.2}$$

which is the fundamental equation of Galactic structure analysis (Burton 1988). Via the H I line one observes v_{obj}, and assuming foreknowledge of the Galactic rotation law $\theta(R)$, one can find the object's *kinematic distance* R in terms of constants R_0 and θ_0. For example, the widely accepted "flat" rotation law[2] ($\theta(R) = \theta_0$) gives a kinematic distance:

$$\frac{R}{R_0} = \left(1 + \frac{v_{obj}}{\theta_0 sin(\ell)\, cos(b)} \right)^{-1} \tag{1.3}$$

from which one finds the heliocentric distance r from the cosine law:

$$R^2 = R_0^2 + r^2 cos^2(b) - 2 R_0 r cos(b)\, cos(\ell) \tag{1.4}$$

[2]A flat rotation curve beyond a certain radius has been observed for many external galaxies.

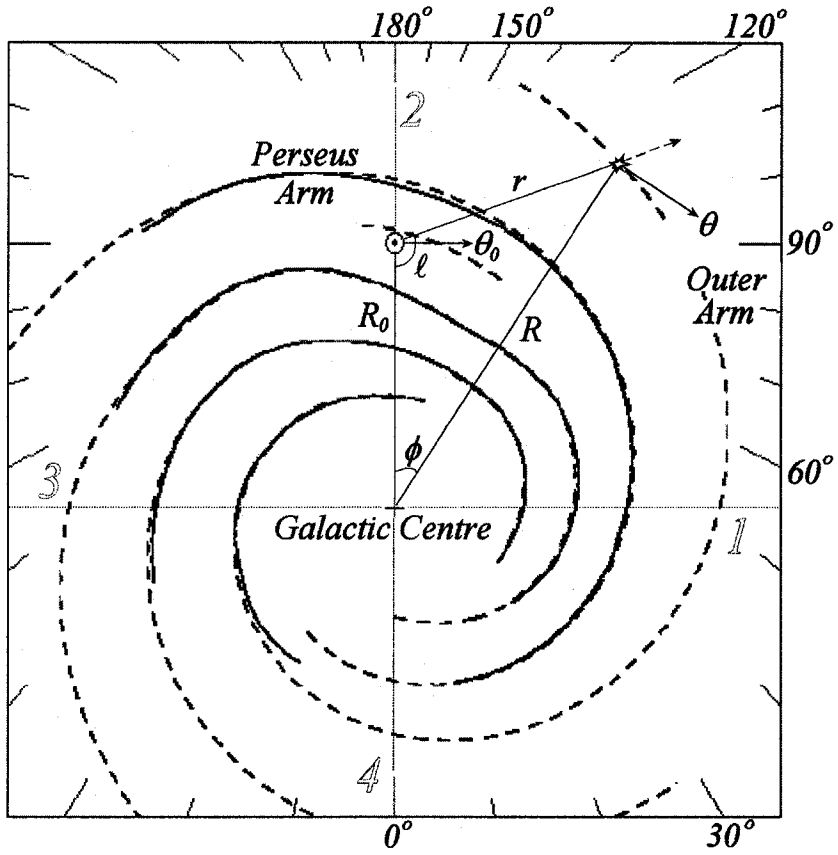

Figure 1.1: A face-on illustration of the Milky Way Galaxy, and definitions of Galactic longitude ℓ, Galactocentric azimuth ϕ, heliocentric distance r, and Galactocentric distances R and R_0. Galactic latitude b is positive for lines of sight with vertical components out of the page, and is negative for components into the page. The direction ℓ=110°, b=0° towards an object in the Outer Spiral Arm (labelled) a distance r from the Sun (and R from the Galactic centre), with circular orbital velocity $\theta(R)$, is shown. The Sun's position (marked as $\odot$) is R_0 with circular velocity θ_0, and it is located within a minor "spur" (dashed line near $\odot$) known as the Local Arm. Positive Galactic latitudes b are for lines of sight directed out of the page, and negative latitudes for those into the page. The major quadrants of the Milky Way (1 through 4) are shown. The spiral arm structure in the figure is from the model of Cordes & Lazio (2002), where dashed spiral arms are uncertain extrapolations.

1.2.2 The Origin of Non-Circular Motions

The work contained within these pages was intended to resolve the so-called Second-Quadrant Problem[3] where kinematic distances based on the above flat rotation model of the Milky Way are significantly different from stellar distances. This creates an apparent rift between the optical spiral arm (traced by luminous OB stars, and H II regions) and the arm traced by neutral hydrogen. We review the likely cause.

Density Wave Theory

A kinematic distance to a packet of H I gas for example, presupposes that the gas is free from systematic streaming motions, a gross oversimplification of the environment within the spiral arms (see Fig. 1.2), where many objects of interest lie. H I and other matter encountering a spiral density wave (e.g. Lin, Yuan, & Shu 1969) will be affected by the gravitational potential of the arm's concentration of matter, and their once-circular orbits are weakly constrained to follow the pitch angle of the arm itself (Fig. 1.2). The arm is maintained (matter is conserved) by the entry of this gas, and the similar migration of gas and stars from out the far-edge. Massive luminous O & B stars (and their surrounding H II regions) generally do not have a sufficient lifespan to fully migrate through an arm, and hence they provide very good tracers of spiral structure. Fig. 1.2 shows the location of newly formed stars for a spiral arm whose gravitational field is 5% of the axisymmetric field. As they are marshaled along by the arm, these objects and the neutral gas inevitably must gain streaming motions (of order 10 km s^{-1}, Lin et al. 1969) towards the Sun. Migrating through the arm, the kinematically-derived distance to a packet of H I can no longer be accurate, as the LOS velocity does not fully descend from circular orbiting motion. However, the potential well of the density wave alone does not completely account for the 20-30 km s^{-1} deviation from circularity observed for many second quadrant objects (e.g. see Chapters 2 & 4). These substantial deviations are explained by the presence of a shock in the potential minimum of the density wave.

The streaming motions imparted to an H I packet entering the arm's poten-

[3]See Fig. 2.1, Chapter 2 for a graphical display of this problem.

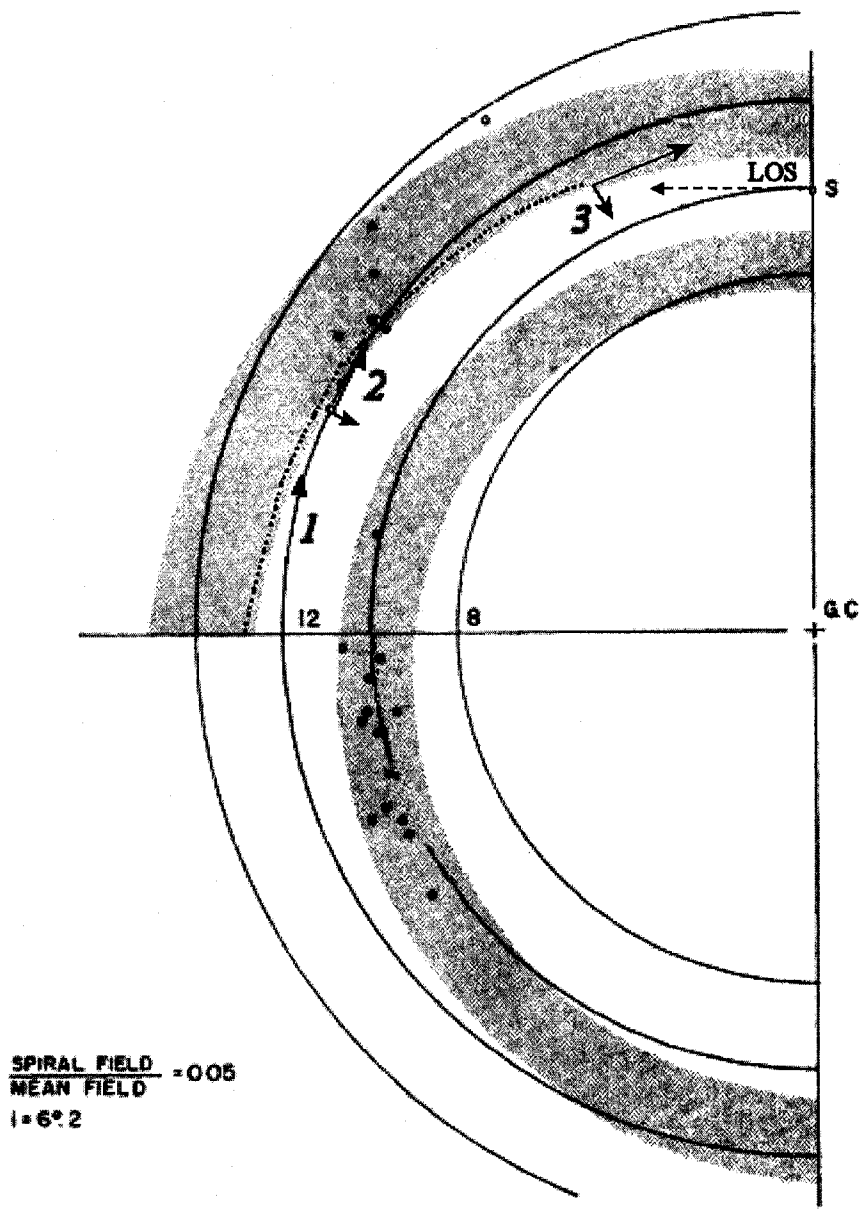

Figure 1.2: A view of spiral structure calculated from density wave theory (Figure 7 in Lin at al. 1969, modified here). The spiral arms (grey hatched regions) are well traced by luminous stars of known age (dots). Circles of constant radii about the Galactic centre (GC) are shown, and the Sun here is at R_0=10 kpc (although the modern value is 7-8 kpc, Reid 1993). A packet of gas with velocity dictated by its circular rotation at Region 1 (labelled) enters the arm at Region 2 and is slowed by the arm's gravitational field, its orbit falling slightly towards the Galactic centre. In this way it is weakly constrained to follow the pitch angle of the arm (here 6°). A shock is envisioned by Roberts (1972) to form in the density wave's potential minimum (inner-edge of the gaseous arm, dotted line). This further affects the H I, which at Region 3 (observed from the Sun) would appear to be moving towards the Sun *faster* than the LOS velocity component of its circular rotation.

tial well are likely to be higher than the local sound speed, and the calculations of Roberts (1972) indicate the formation of a shock on the arm's inner edge. The compressed gas within the shock enhances the original imposed gravitational field of the background density wave. Indeed, this shock may be the trigger necessary for the collapse of H I clouds entering the arm, and the subsequent formation of stars. As we have a view of the Perseus Arm's inner edge, this would be the natural place to look for a spiral shock, and indeed, the velocity fields calculated by the author's method in Chapter 5 show evidence for one.

1.3 Assumptions and Prior Knowledge

In the new method, we are trading a model of Galactic rotation (in the kinematic method) for an H I mass model, and we end up trading assumptions as well. We no longer assume that motions of the gas arise purely from its response to the axisymmetric field. Rather more basically, we assume that on a large scale velocity is monotonic (single-valued) for increasing distance. In other words, we assume that *most of the gas* in an H I spectrum is found at a LOS velocity consistent with some decreasing function of its distance from the Sun. This is not just a blind assumption, but one that is very well justified by the observed relationship between ^{12}CO line velocities and stellar distances for H II regions (see Fig. 1.3). It is very apparent in this figure that a smooth decreasing velocity field describes this relationship very well.

As the method relies upon a smooth velocity field to map a density model onto an H I profile, a second implicit assumption must be that the structure observed in H I spectra is primarily due to density variations in the gas, and to a much lesser extent, kinematical effects. The work of Burton & Bania (1974) showed that, under the elementary assumption of a gaseous disk with uniform density and temperature, H I profiles in the 2nd quadrant could be reproduced (to within a scale factor) by only moderate perturbations in just the velocity field. Of course, it is not physically realistic to expect the disk to be isotropic, but it is equally unlikely that a purely circular velocity field prevails, and spatial density variations *alone* determine the shape of the profiles.

As a matter of course (dictated by the first assumption), we proceed with

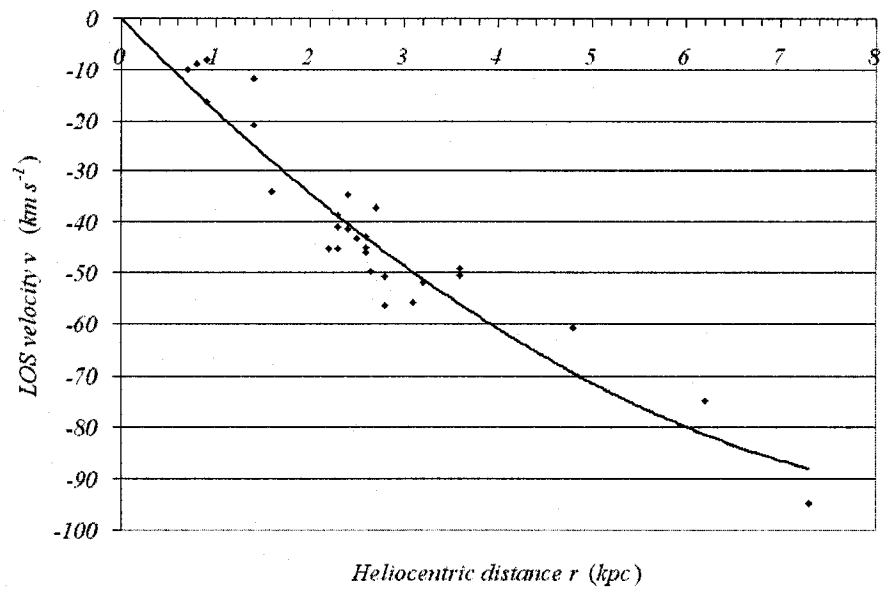

Figure 1.3: The relationship between ^{12}CO emission line velocity and photometric distance (independent of velocity) for 29 H II regions in the second quadrant ($90° \leq \ell \leq 140°$). Some of the scatter is attributed to the sample's wide range of longitudes. The velocities were measured by the author using ^{12}CO data from the Columbia CO survey (Dame et al. 2001) and the FCRAO Outer Galaxy Survey (Heyer et al. 1998). A Gaussian function was fitted to the velocity profile of CO emission that is spatially associated with each H II region. Distances are from the catalogue of Fich, Blitz, & Stark (1989).

the premise that density contrasts are responsible for the broadest structure in H I spectra. We keep our density model as simple as possible, and do not adjust the model to fit narrow "spikes" and deep troughs in H I spectra, features commonly observed[4].

1.4 Summary of Research

Section 1.2.2 above summarizes the major forces suspected to be at work in the Galactic disk and spiral arms. Perseus Arm objects with LOS velocities that are blueshifted from circular ones by 20-30 km s^{-1} are observed throughout the 2^{nd} quadrant, evidently affected by these forces. Since the exact magnitudes of the non-circular motions are unknown, the attack on the Second-Quadrant Problem has been kept independent of any rotation curve.

The body of the text in this work begins with Chapter 2, which is a detailed development of the H I column density model used in the new distance calculation method. The approach begins similar to Drimmel & Spergel's (2001) mass distribution model of dust, where distance is treated as a variable. I continue by numerically integrating the H I density model to measure the cumulative hydrogen column density N_{HI}. My new method also takes advantage of the available velocity information, and what the method constructs is in fact a relationship between line of sight velocity (v) and heliocentric distance (r).

Next in Chapter 2, the new distance method is tested as just that: a *distance method*. Distances calculated for 29 outer-Galaxy H II regions are compared with distances known from photometric distances of resident stars within. This benchmarking is an extremely important step which helps to justify otherwise unprovable assumptions intrinsic to the method (such as the existence of a monotonic velocity-distance relation). The conclusion of this test is that a smooth relation between v and r maps the H I column density model to the observed velocity distribution of H I well, and predicts correct distances for objects at specific velocities. Such a $v(r)$ relation is fundamental to circular rotation, which is shown to be largely obeyed by our Galaxy by velocity crowding seen in H I

[4]For this reason, the fitting procedure is not automated but interactive, and a final fit is not determined by a minimized χ^2 alone, but also by the judiciousness of the astronomer.

spectra near ℓ=0° and ℓ=180°.

A method that can predict accurate distances has profound effects on individual object studies, especially on those to which ascribing an accurate distance previously remained a challenge. The thesis' next chapters (Chapter 3 and 4) describe a study of a supernova remnant (SNR) found to be evolving within a stellar wind bubble (SWB), and presents new reddenings and distances to all objects in the region near ℓ=93°, b=0°. The purpose of this work's presence in the text is two-fold. First, it is intended to show the reader how fundamental a proper distance calculation is to the determination of the physical and dynamical properties of individual objects in the Galaxy. Second, the quality of information we are able to measure for objects in this area shows the benefits of a multi-wavelength approach. These two chapters bring together radio, optical, and X-ray astronomical data in a symphonic way.

The fifth major chapter shows a basic output of the distance method, the determination of the relationship between v and heliocentric distance r (referred to hereafter as the velocity field). The chapter presents new one-dimensional velocity fields for given directions into the plane, and explores their properties and applications. With the predicted velocity fields from the method, one can remap the Galactic Warp into velocity space, determine values for the Oort constants, and reconstruct the Galactic rotation curve by imposing the assumption of circularity (i.e. the observed velocities arise completely from circular rotation). The chapter concludes by discussing results from this step and caveats to the approach.

A final, brief summary of the work concludes the thesis. This final chapter summarizes the accomplishments of the work, expands on future directions and ideas, and shows the overall contribution that the work has already made to the field of Galactic astronomy.

The first two chapters are material published in the Astrophysical Journal (Chapter 2) and Astronomy & Astrophysics (Chapter 3). Chapter 4 contains unpublished work, and much of the material in Chapter 5 has been presented at the Fifth Boston University Astrophysics conference *Milky Way Surveys: The Structure and Evolution of Our Galaxy*, and appears published in the proceedings for that conference. Each chapter is preceded by a detailed summary of

the work and its results. It is the sincerest hope that this thesis will serve the reader in his/her pursuits of astronomical science, whether in optical or radio wavelengths, perhaps in both.

Bibliography

[1] Burton, W. B. 1988, in Galactic and Extragalactic Radio Astronomy, eds. G. L. Verschuur & K. I. Kellermann, Springer-Verlag, New York, 295

[2] Chen, B., Figueras, F., Torra, J., Jordi, C., Luri, X., & Galadí-Enríquez, D. 1999, Astronomy & Astrophysics, 352, 459

[3] Cordes, J. M., & Lazio, T. J. W. 2002, Astro-ph archive 0207156

[4] Dame, T. M., Hartmann, Dap, & Thaddeus, P. 2001, Astrophysical Journal, 547, 792

[5] Diplas, A., & Savage, B. D. 1991, Astrophysical Journal, 377, 126

[6] Drimmel, R., Cabrera-Lavers, A., & López-Corredoira, M. 2003, Astronomy & Astrophysics, 409, 205

[7] Drimmel, R., & Spergel, D. 2001, Astrophysical Journal, 556, 181

[8] Fich, M., Blitz, L., & Stark, A. A. 1989, ApJ, 342, 272

[9] Gathier, R., Pottasch, S. R., & Pel, J. W. 1986, Astronomy & Astrophysics, 157, 171

[10] Hakkila, J., Myers, J. M., Stidham, B. J., & Hartmann, D. H. 1997, Astronomical Journal, 114, 2043

[11] Heyer, M. H., Brunt, C., Snell, R. L., Howe, J. E., Schloerb, F. P., & Carpenter, J. M. 1998, Astrophysical Journal Supplement, 115, 241

[12] Malhotra, S. 1995, Astrophysical Journal, 448, 138

[13] Méndez, R., & van Altena, W. 1998, Astronomy & Astrophysics, 330, 910

[14] Nakanishi, H., & Sofue, Y. 2003, Publications of the Astronomical Society of Japan, 55, 191

[15] Ortiz, R., & Lépine, J. R. D. 1993, Astronomy & Astrophysics, 279, 90

[16] Reid, M. J. 1993, ARA&A, 31, 345

[17] Robin, A. C., Reylé, C., Derrière, S., & Picaud, S. 2003, Astronomy & Astrophysics, 409, 523

[18] Schlegel, D. J., Finkbeiner, D. P. & Davis, M. 1998, Astrophysical Journal, 500, 525

[19] Taylor, A. R., Gibson, S. J., Peracaula, M., Martin, P. G., Landecker, T. L., Brunt, C. M., Dewdney, P. E., Dougherty, S. M., Gray, A. D., Higgs, L. A., Kerton, C. R., Knee, L. B. G., Kothes, R., Purton, C. R., Uyaniker, B., Wallace, B. J., Willis, A. G., & Durand, D. 2003, Astronomical Journal, 125, 3145

[20] Taylor, J. H., & Cordes, J. M. 1993, Astrophysical Journal, 411, 674

Chapter 2

A New Distance Technique for Galactic Plane Objects

Foreword

This chapter introduces the method of H I study described throughout this thesis. All text in this chapter appears in publication in the Astrophysical Journal, December 2003, vol. 598, no. 2. My supervisor Dr. David Routledge appears as second author.

Figure 2.1 in the paper highlights the so-called "Second Quadrant problem", where an object's line of sight velocity v_{obj} yields an unrealistically high distance, when calculated with the widely accepted flat rotation curve of Fich, Blitz & Stark (1989). These distances place many objects near the edge of the Galaxy ($R \sim 14$ kpc, Robin et al. 1992). The problem is not necessarily one of an inaccurate rotation curve, as the observed velocities may include other contributions than simply the LOS component of an object's orbital velocity. However, if a spiral shock were to be responsible for this (see Roberts 1972), very high radial velocities (e.g. for Sh127, $v_{obj} = -95$ km s^{-1}) would return kinematic distances nearer to the truth, as a "shocked" flat rotation curve returns to flatness at some distance from the shock front. This is not observed in Figure 2.1.

Figure 2.11 shows the resolution to the problem, at least with respect to spectrophotometric distances (which have problems of their own). The paper concludes that the photometric distances in Fich, Blitz & Stark are moderately too high.

It is notable that values of photometric distances increase to unphysical values with higher longitude (e.g. see the distances of Chini & Wink, 1984). The importance of the contribution the author's new distance method makes is already being shown. The author believes that with increasing longitude the total reddening of exciting stars becomes more dominated by the dust in shells encircling these H II regions, and that using the typical value of 3.1 for reddening parameter $R_V = A_V/E(B-V)$ (which applies only to dust in the smooth foreground ISM) causes an over-estimate in the distance modulus. The new distance method will show this, and allow calculation of new values for the reddening parameter R_V. A paper with R. Kothes (DRAO) is in preparation on this important exploitation of the distance method derived herein.

Abstract

We present a new method based on H I column densities for determination of distances within the disk of the Galaxy. The technique is useful for all Galactic plane objects including H II regions and supernova remnants (SNRs) provided a line of sight velocity can be assigned to the object. Our method uses λ21 cm spectral line data to find the atomic hydrogen column density to an object, and beyond it to the Galactic edge. A model of the smooth large-scale Galactic distribution of H I material seen in emission (which principally traces the smooth structure of the Galaxy) is constructed. Our model accounts for scale-height flaring with increasing Galactocentric radius, and includes the Galactic Warp, which is prominent in the first and second quadrants of the Galaxy. The model's ability to trace the observed distribution of H I is demonstrated on lines of sight towards SNR DA530 (ℓ=93.3°, b=7°) and H II region Sh121 (ℓ=90.2°, b=1.7°). We then apply the new technique to 29 Sharpless H II regions with known photometric distances across the second quadrant. We measure line of sight velocities for the H II regions from associated ^{12}CO emission, using 1 arcminute resolution ^{12}CO(J=1-0) data from the Canadian Galactic Plane Survey. Our distance method yields distances to these objects that are consistent with their photometric distances, and which are markedly smaller than the kinematic distances found from a flat Galactic rotation curve.

2.1 Introduction

Obtaining distances to H II regions and supernova remnants in the outer Galaxy is fraught with difficulties. Observations of exciting stars associated with H II regions can be attempted to find the object's *photometric* distance, but near the Galactic plane success is increasingly unlikely beyond 2 kpc, as the effect of interstellar obscuration is pronounced at low latitudes. Alternatively, line-of-sight (LOS) velocities from H I or CO associated with the objects of interest can be used to measure their *kinematic* distances. However, the kinematic method of distance determination is ultimately dependent on the model of Galactic rotation one subscribes to, and normally assumes both a smooth velocity distri-

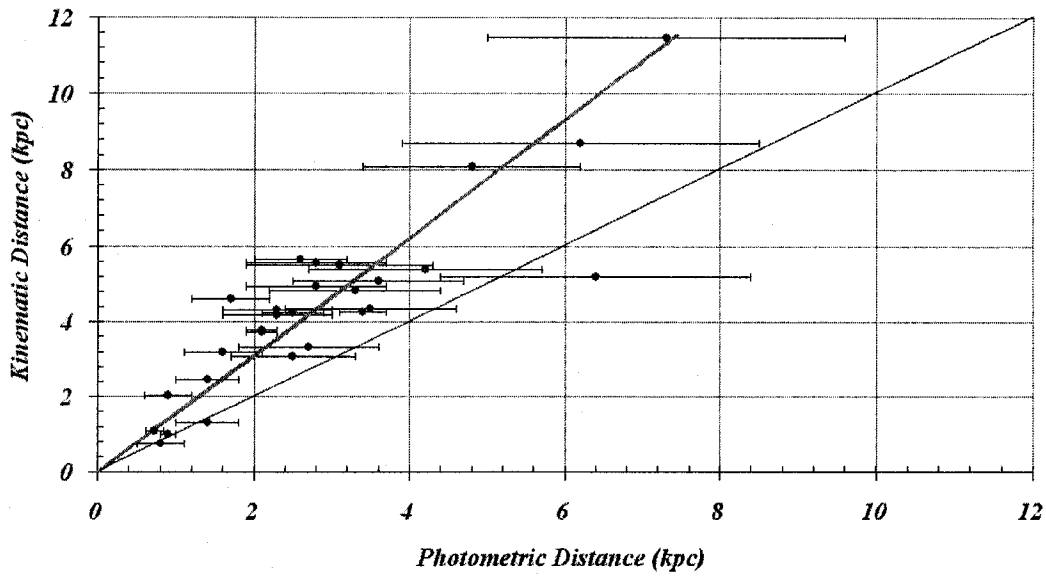

Figure 2.1: Comparison of kinematic and photometric distances to 28 H II regions in the Galactic plane region across 90° < ℓ <140°. The plot illustrates a fundamental inconsistency between distances calculated kinematically from a widely used flat rotation curve (FBS, 1989) and the photometric distances used by them. A 1:1 correlation (thin black line) is not found; the kinematic distances are larger than photometric ones by 1.6:1 across this longitude range (thick grey regression line).

bution along the line of sight and that observed velocities arise due to purely circular Galactic motion. Figure 2.1 illustrates the fundamental inconsistency of kinematic distances with other established methods. The correlation is clearly far from unity between photometric distances to second quadrant H II regions from the catalogue of Fich, Blitz & Stark (1989, hereafter FBS), and kinematic distances calculated by using ^{12}CO velocities listed for each nebula with the flat Galactic rotation curve derived by those authors (R_0=8.5 kpc, θ_0=220 km s^{-1}).

No other reliable distance method for supernova remnants and distant H II regions exists, which is unfortunate in light of the multitude of such objects now imaged with high resolution, e.g. in the Canadian Galactic Plane Survey (CGPS, Taylor et al. 2003).

The new technique described here is similar in concept to the optical extinction-

distance method, used principally to find distances to nearby (less than 2 kpc) planetary nebulae (e.g. Gathier et al. 1986). However, this classical method relies solely upon reddening-distance relations derived from photometric or spectral observations of stars in the direction of interest. Many problems can arise in this approach, especially for distant and/or highly reddened nebulae. A sufficient number of field stars near to the nebula must be observed to find a useful range of data to construct a reddening-distance relation. Stars up to 5 degrees away from the target must often be included, but can introduce significant errors due to the patchy distribution of dust and the effect of this on observed stellar colours. The scatter in individual stars about a common curve increases significantly with larger reddenings and distances, as does an observational bias towards less-reddened, though distant stars (often giants) which will dominate one's sample. Thus, deriving a reliable relationship between extinction and distance from samples of stars becomes nearly impossible for large distances.

In this work, we present an original distance method that is independent of Galactic kinematics, but is based instead on atomic hydrogen column densities. With a known value of H I column density to the Galactic edge $N_{HI}(r = \infty)$ and a model of the smooth, large-scale distribution of hydrogen atoms $N_{HI}(r, \ell, b)$, one can match an object's measured column density N_{HI} with a distance calculated from the model (see Fig. 2.2). We develop this into a new tool for finding accurate distances to objects in the Galactic plane (see Sec. 2.2). CGPS H I and ^{12}CO line data are used to measure velocities, column densities and Galactic model parameters for target objects. We fully demonstrate the method's results on 29 H II regions from the catalogue of FBS, all of which have known spectrophotometric distances and lie in the second quadrant ($90° < \ell < 140°$) near the Galactic plane ($-3.5° < b < 5°$). An important feature of our method is its applicability to supernova remnants (SNR), notoriously difficult objects for which to find distances. With H I emission and absorption spectra derived from CGPS data, atomic hydrogen column densities to SNR's with known line of sight velocities can now be found with excellent accuracy. We demonstrate the method on the SNR DA530 (ℓ=93.3°, b=7°) in Sec. 2.2.

The aim of this paper is to present our distance technique in detail, deriving non-kinematic distances for Galactic objects, and comparing these with pho-

tometric distances and also with kinematic distances derived from the widely used flat model of Galactic rotation.

2.2 Constructing A Model of the Galactic H I Distribution

We now begin the construction of a model density profile $n(r, \ell, b)$ of neutral hydrogen atoms, which is necessary to calculate the expected LOS variation of cumulative H I column density in a chosen direction:

$$N_{HI}(r, \ell, b) = \int_0^r n(r', \ell, b) dr' \tag{2.1}$$

The pioneering work of Parenago (1945) led to the first model of reddening $E(B-V)$ distribution with distance. Méndez and van Altena (1998) proposed a similar extinction model (hereafter M&vA model) for Galactic latitudes outside the plane $|b|$ >5°. Chen et al. (1999) reproposed the M&vA model, based on colour-excesses to the Galactic edge, $E(B-V)(r = \infty)$, found from the all-sky reddening maps of Schlegel et al. (1998). However, at low Galactic latitudes ($|b|$ <5°) contamination from point sources can dominate the measured reddening, and the Schlegel maps cannot measure an accurate value of $E(B-V)(r = \infty)$, a parameter necessary for the Chen model.

The above models rest on simplistic assumptions concerning the large-scale density profile throughout the Galaxy, giving a profile that decays *only* away from the plane:

$$n(r, b) = n_0 exp(-|Z(r, b)|/h_z) \tag{2.2}$$

where $Z(r, b)$ is the height of the LOS above the midplane, r is heliocentric radius, and h_z is the scale height of the dust. The M&vA model assumes a flat midplane; thus, an LOS with Galactic latitude b has a height above the disk $Z(r, b) = Z_\odot + r sinb$, where $Z_\odot$ is the height of the Sun above the midplane. The form of this model of material distribution therefore includes only the density variation with increasing height above a flat disk.

Unfortunately, the functional form of such extinction-distance models pre-

dicts nonsensical extinction rates for low latitudes ($|b|$ <10°), and zero increase in extinction per unit distance for lines of sight directly into the Galactic plane ($b = 0$).

We proceed to derive a new density model based on neutral hydrogen column densities N_{HI}. In the final model, we express Galactocentric radius R in terms of heliocentric distance r using $R^2(r, \ell, b) = R_0^2 + r^2 cos^2\,(b) - 2R_0 r cos\,(\ell)\,cos\,(b)$, where we use R_0=8.0±0.5 kpc (Reid 1993).

We begin by modifying the height distribution law of Eqn. 2.2 to the form $sech^2\,(Z(r,b)/h_z)$, which is Spitzer's (1942) solution for the z-profile of a self-gravitating isothermal disk. Values for the parameter h_z have been determined by many authors, most falling within a canonical range of 100 pc $\leq h_z \leq$ 200 pc. However, observations have shown that the thickness of the H I layer increases with Galactocentric radius beyond the solar circle. It is therefore proper to model the H I disk's z-structure with a linearly increasing scale height:

$$h_z(r, \ell, b) = h_0 + h'\,(R(r, \ell, b) - R_0) \tag{2.3}$$

where the flaring of the H I layer is set to begin at the Solar Galactocentric radius R_0. The rate of increase h' of the H I layer's half-thickness with distance is calculated by Merrifield (1992), whose method shows a rate of about 31 pc/kpc beyond R_0. For the purposes of this paper, we adopt a value of h'=30 pc/kpc for our model of the H I density variation with height. We also begin with a half-thickness of h_0~200 pc at the Sun's position (e.g. Merrifield 1992), but note that other authors have found it to be higher (e.g. Diplas & Savage 1991).

The density of neutral material in the Galactic disk decays with Galactocentric radius as well. We admit an exponentially varying radial component of the density law to the height distribution:

$$n(r, \ell, b) = n_0 exp\,(-(R(r, \ell, b) - R_0)/h_R)\,sech^2\,((Z_\odot + r sinb)/h_z(r, \ell, b)) \tag{2.4}$$

where h_R is the scale length in R of the density in the H I disk. Values for h_R in the literature range from $0.25R_0$ to $0.36R_0$ from Diplas & Savage (1991), up to $0.49R_0$ (Merrifield 1992). We begin with an intermediate value of $0.35R_0$ (2.8 kpc for R_0=8 kpc), and determine h_R for individual longitudes by the method

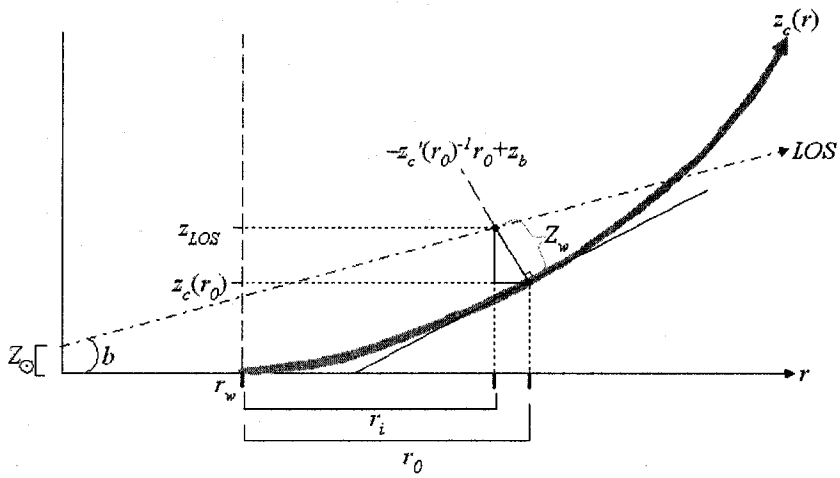

Figure 2.2: An illustrative diagram of the geometry used in finding the height of the line of sight above the warping midplane (Z_w) as a function of r. Note how the line of sight (labelled LOS) passes through the midplane.

in Sec. 2.2.2.

The above expression models the axisymmetric density profile across the disk. To be a useful reflection of the true Galactic distribution of H I, we must include non-axisymmetric features. One such structure is the Galactic Warp, the bend in the gas layer in the H I disk, which is a prominent feature in the first and second quadrants. The height of a LOS above the warping midplane will change in a non-linear fashion as distance increases. The LOS will eventually intersect the dense middle disk, pass through it, and exit into the lower density portions under the disk. This has a noticeable effect on the shape of $n(r, \ell, b)$, and hence the distances derived to those objects found within the warped part of the plane. Accounting for the Warp, the form of the height of a given LOS above the warped disk, $Z_w(r, \ell, b)$ (valid for heliocentric distances beyond that at which the Warp begins, r_w, see Fig. 2.2) is thus more complex than $Z(r, b)$ in Eqn. 2.4, which remains valid for $r < r_w$.

Previous authors' models of the Warp's figure are based on H I velocities, and hence usually on kinematic distances. We avoid prejudicing our model in this way, and begin with a form similar to that of Binney & Merrifield's (1998) kinematic-based equation, but for a given ℓ we leave the Galactocentric radius

in the plane at which the Warp starts (R_w) as a free parameter (but we assume $R_w > R_0$). Our expression for the height of the warping midplane is thus general:

$$z_c(R,\phi) = \frac{R-R_w}{6} sin\phi + 0.3\left(\frac{R-R_w}{6}\right)^2 (1-cos2\phi)\,, R \geq R_w \qquad (2.5)$$

where ϕ is Galactocentric azimuth (see Fig. 1.1), and is related to Galactocentric radius R by $sin\phi/r = sin\ell/R$. We then express Eqn. 2.5 as $z_c(r_0,\ell)$, where $r_0 = r - r_w$, and derive solutions for $Z_w(r,\ell,b)$ from the geometry of the system (see Fig. 2.2), which gives:

$$Z_w^2(r,\ell,b) = (r_0 - r_i)^2 + (z_{LOS} - z_c(r_0,\ell))^2\,, r \geq r_w \qquad (2.6)$$

where $z_{LOS} = Z_\odot + (r_w + r_i)tanb$, and r_i is the distance at which the sight line z_{LOS} intersects a line normal to the warped plane that passes through $z_c(r_0)$:

$$r_i = \frac{z_c(r_0) + (z_c'(r_0))^{-1} r_0 - (Z_\odot + r_w tanb)}{tanb + (z_c'(r_0))^{-1}} \qquad (2.7)$$

and $z_c'(r_0)$ is $dz_c(R,\phi)/dR$ evaluated at r_0. For our determination of the distance from the Sun at which the Warp begins (r_w), see Sec. 2.2.2.

The new expression for the density encountered along a line of sight above the plane is:

$$n(r,\ell,b) = n_0 exp\left(-(R(r,\ell,b) - R_0)/h_R\right) sech^2\left(-Z(r,\ell,b)/h_z(r)\right) \qquad (2.8)$$

where:

$$Z(r,\ell,b) = \begin{cases} Z_w(r,\ell,b),\ r \geq r_w \\ Z_\odot + r sinb,\ r < r_w \end{cases} \qquad (2.9)$$

For $Z_\odot$ we subscribe to a value of 15 pc, a reasonable mean from many recent determinations in the literature tabulated by Humphreys & Larsen (1995). Eqn. 2.8 models the axisymmetric distribution of absorbing material, but accounts for the Galactic Warp as well.

Finally, we account for the most conspicuous non-axisymmetric density structures along lines of sight in the plane, those present in the spiral arms. For

second-quadrant lines of sight into the plane, most H I spectra prominently show the Perseus spiral arm, which appears as a 20-30 km s^{-1} wide quasi-Gaussian feature in velocity. The breadth of this feature is likely dominated by differential rotation across the arm, with a small contribution from turbulent motion within the gas (~8 km s^{-1}). We assume that the spatial distribution of H I material through an arm is approximately Gaussian in form, and that the observed velocity width roughly reflects the spatial width of the arm along the LOS. We therefore model the radial density variation due to the Perseus arm as a Gaussian function with centre at Galactocentric radius R_m, whose profile is most narrow (width w_{arm}) along a line connected to the Galactic centre:

$$n_{arm}(r,\ell,b) = n_{0,arm} exp\left(-(R(r,\ell,b) - R_m)^2/w_{arm}^2\right) sech^2\left(-Z(r,\ell,b)/h_{z,arm}\right) \tag{2.10}$$

where we have assigned to the arm its own height constant $h_{z,arm}$. That the Sun lies within a minor spiral segment (the "Local Arm") is suggested by Georgelin & Georgelin (1976), and neutral hydrogen belonging to this structure appears as a relatively narrow (12-20 km s^{-1}) emission line at velocities near 0 km s^{-1} in CGPS H I spectra. Unlike the Perseus Arm, we cannot easily determine the density distribution of the foreground material from this line, as turbulent motions undoubtedly contribute a significant amount to the local feature's velocity width and may vary strongly with direction because of our location within the Local Arm. We choose not to include a specific model component devoted to this feature here[1] and instead allow the model to trace only the smooth axisymmetrically distributed local H I.

The final density profile resulting from our model (normalized to unity at $R = R_0$) is therefore:

$$\begin{aligned} n(r,\ell,b)/n_0 = & \; exp\left(-(R - R_0)/h_R\right) sech^2\left(-Z(r,\ell,b)/h_z(r)\right) \\ & + \frac{n_{0,arm}}{n_0} exp\left(-(R - R_m)^2/w_{arm}^2\right) sech^2\left(Z(r,\ell,b)/h_{z,arm}\right) \end{aligned} \tag{2.11}$$

where of course $R \equiv R(r,\ell,b)$, and the coefficient $n_{0,arm}/n_0$ represents the ratio

[1]The addition of a minor model component that accounts for the Local Arm H I is discussed in Chapter 5.

of the density within the Perseus Arm to that of the smooth ISM material at R_0 and $Z_\odot$. This is estimated for each direction (see Fig. 2.3) from the CGPS H I spectrum by calculating the ratio of the brightness temperature at the Perseus Arm's peak to the mean brightness temperature at zero velocity[2]. Using Eqn. 2.11 in Eqn. 2.1, we find numerical solutions for the cumulative column density along the LOS towards a given source as a function of distance. In our representation of the solutions of Eqn. 2.1 (column density - distance relations), we scale the models to reach the column density observed at the Galactic edge, $N_{HI}(r = \infty)$, in the limit of large r. Sec. 2.2.1 gives our method of determination of $N_{HI}(r = \infty)$ and N_{HI}. Our relations are effectual for all latitudes (including b=0°), unlike the dust models of M&vA (1998), and Chen et al. (1999).

2.2.1 Determining the H I Column Density to Objects and to the Galactic Edge

The most important parameters to obtain for our model are the H I column density to a given source (expressed as N_{HI}), and the column density to the Galactic edge $N_{HI}(r = \infty)$.

It is customary to express the brightness B at frequency ν of an extended radio source by its *brightness temperature* T_b, which, from the Rayleigh-Jeans Law for a blackbody is $T_b = c^2 B/2k\nu^2$. For an isolated Galactic H I cloud at velocity v with a uniform Boltzmann temperature T_s and optical depth $\tau(v)$, the observed brightness temperature is $T_b(v) = T_s\,(1 - exp\,(-\tau(v)))$[3]. The following relation defines the LOS *column density*:

$$N_{HI}(\mathrm{cm}^{-2}) = 1.823 \times 10^{18} T_s \int^{v_{obj}} \tau(v)dv \qquad (2.12)$$
$$\simeq 1.823 \times 10^{18} \int^{v_{obj}} T_b(v)dv,\ \tau(v) \ll 1$$

[2]This is a difficult estimate to make, as the local spur H I is never too far from $v = 0$ km s^{-1}. However the brightness temperature at the velocity origin is offset from the peak of the local material, which is usually nearer to -10 km s^{-1}. The calculated ratio across $90° \geq \ell \geq 140°$ is typically greater than 1 but never more than 2.

[3]This is the solution to the equation of radiative transfer for an isothermal cloud; see Gibson et al. 2000

So long as absorption of background emission by foreground gas is minimal (i.e. the optical depth of the H I is $\tau \ll 1$), emission from all H I along the column will reach our telescope, and $T_b(\mathrm{K}) \propto n(\mathrm{cm}^{-3})$. Eqn. 2.12 is an expression of this proportionality and assumes that the H I column is optically thin.

With an observed H I emission profile towards the source, one integrates the emission over all velocity channels to obtain $N_{HI}(r = \infty)$, or using the source velocity v_{obj} as the upper limit, to obtain the column density to the source N_{HI}.

Comparing Eqn. 2.12 with Eqn. 2.1 illuminates two major assumptions we make throughout this work: (i) on a large scale, LOS velocity is monotonic with heliocentric distance, and (ii) the H I in emission profiles is optically thin and traces the smooth large-scale distribution of thin-disk H I.

We now discuss the latter assumption. Generally, Eqn. 2.12 underestimates the total column density of neutral hydrogen, since cooler, optically thick gas has low brightness and is essentially not included in a column density obtained by integrating H I emission alone. Optically thick H I is indeed present throughout the ISM and is sometimes seen in self-absorption, but is cold and dense, and is predominantly found on smaller angular scales than emission (Gibson et al. 2000). H I column densities measured from absorption can include a large contribution from these small-scale clumps of cold H I, but these clumps do not trace the overall smooth distribution of H I found populating the ISM. The ubiquity of H I emission in the Galactic disk suggests that emission almost certainly does trace this distribution (Burton 1988), and we therefore use H I emission alone to follow the smooth component of interstellar neutral hydrogen. We employ Eqn. 2.12 in finding $N_{HI}(r = \infty)$ for our models, and N_{HI} for our distance estimates[4].

We use λ21 cm H I data observed with the 7-element Synthesis Telescope at the Dominion Radio Astrophysical Observatory (DRAO), data obtained as part of the CGPS (Taylor et al. 2003). The angular resolution achieved by the interferometer at 1420 MHz varies with position in the sky as $1' \times 1'\mathrm{cosec}(\delta)$. Spatial frequency components corresponding to large scale H I features are not observed

[4]It is important to realize that as long as N_{HI} and $N_{HI}(r = \infty)$ are both found consistently by integration of H I emission, optically thick H I that is present along the LOS will not affect these density models, so long as it does not appear strongly in emission spectrum.

due to lower limits on the antenna spacing, but are observed with the 26 metre paraboloid at DRAO, and incorporated into the data to create the final 256 channel mosaiced data cube, with channels resolving 1.3 km s^{-1} of velocity and separated by 0.82 km s^{-1}. The uncertainty in the brightness temperature calibration of each mosaiced H I image is $\pm 10\%$.

Values for $N_{HI}(r = \infty)$ and N_{HI} for a given H II region or SNR are measured in the following way. The mean brightness temperature of H I seen in emission is derived from within a box centred on the source and large enough to include much of its surroundings, but excluding the source itself. In this way, we avoid including H I physically associated with the source (e.g. surrounding shells), and not part of the large-scale distribution of H I material along the LOS.

The measurement of the column density between the Sun and the object by integration of H I emission to the object's velocity v_{obj} assumes that all material in the integration range is truly foreground. This assumption may fail, as velocity inversions are known to exist within the Perseus spiral arm, where shocked material on the near side of the arm exhibits more negative velocities than material physically behind it. Generally, however, this assumption is well justified. Velocity-reversed gas that has been shocked will have been compressed into a denser and optically thick "wall" of material, and will not contribute strongly in pure emission spectra. Where opportune we do check this assumption by comparing absorption profiles with those from emission, but this is possible only towards sources whose continuum emission is seen absorbed by foreground H I. If material at more positive velocities than the source is seen absorbing the source's emission, then it is deemed to be foreground, and velocities corresponding to that material are included in the integration limits to find the column density to the object (Eqn. 2.12).

2.2.2 The Essence of the Method; Two Examples

The steps of our new method are shown in a flowchart in Figure 2.3. Briefly, one begins by finding an object's LOS velocity v_{obj}, and uses H I data to measure the column density to that object N_{HI} and to the Galactic edge in its direction $N_{HI}(r = \infty)$. A model of the cumulative H I column density versus LOS dis-

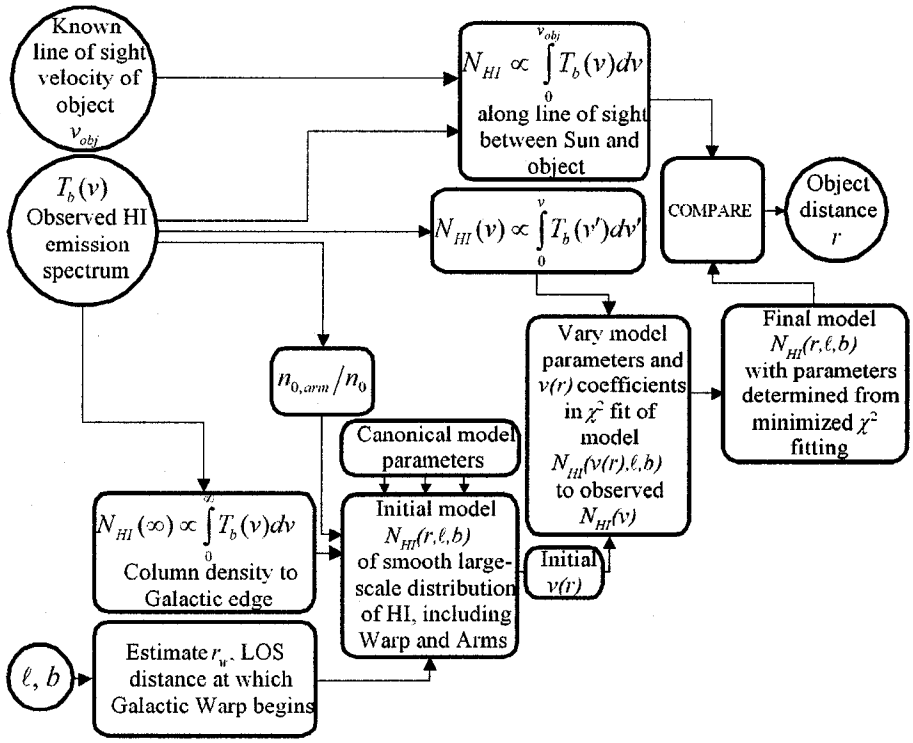

Figure 2.3: A flowchart of the major steps in our distance method. Inputs and outputs of the method are circled, and the method's steps are boxed.

tance $N_{HI}(r, \ell, b)$ is constructed via numerical solutions to Eqn. 2.1, by using Eqn. 2.11 with reasonable initial parameters, and the measured value of column density to the Galactic edge. This model is transformed to velocity space using a velocity-to-distance mapping function, and parameters of this and N_{HI} are varied until the model is a good fit to the overall form of integrated column density versus velocity $N_{HI}(v)$ that is observed in the H I data. Using the satisfactory set of parameters, one simply returns to the spatial distribution model $N_{HI}(r, \ell, b)$, and finds the distance appropriate for the object's measured foreground column density, N_{HI}.

We first demonstrate the fit of our model to the observed $N_{HI}(v)$ towards a LOS at a relatively high latitude, and the distance it calculates for a nearby SNR. H I spectral line data have been obtained by Landecker et al. (1999) toward the SNR DA530 (ℓ=93.3°, b=7°, $v_{obj} = -12$ km s^{-1}). DA530 lies outside the coverage

of the CGPS, and these pre-CGPS H I data are comprised of 128 channel maps with a velocity coverage of 55 km s^{-1} $> v >$ -155 km s^{-1}, with channels separated by 1.65 km s^{-1}. The line data were obtained with the Synthesis Telescope at DRAO, and are more fully described by Landecker et al. (1999).

The LOS toward DA530 provides a relatively undisturbed proving ground for testing our model. Sight lines at this latitude are significantly far from the plane, and do not encounter most of the Perseus Arm material. Non-circular motions associated with the arm's spiral shock are expected to be minimal. Thus, H I along this LOS will be primarily smooth, axisymmetrically distributed gas, and the only non-axisymmetric feature expected to contribute is the Galactic Warp, which will cause the LOS to pass through the disk.

Figure 2.4 displays the observed H I data (open circles), plotted as cumulative column density with LOS velocity $N_{HI}(v)$, calculated via:

$$N_{HI}(v)(\mathrm{cm}^{-2}) = 1.823 \times 10^{18} \int_0^v T_b(v')dv' \tag{2.13}$$

Using the H I data toward DA530, the above expression yields $N_{HI}(r = \infty)$=4.38 $\times 10^{21}$ cm^{-2}. Via Eqn. 2.11 and Eqn. 2.1, a model of $N_{HI}(r)$ for this direction with this termination value is constructed (Fig. 2.5).

For our initial determination of the heliocentric distance at which the midplane begins warping (r_w), we use the Leiden-Green Bank H I survey from Burton (1985). Towards ℓ=93° Burton's data show that for velocities beyond about -25 km s^{-1} the plane bends upward. Using R_0=8.5 kpc and θ_0=220 km s^{-1}, this is a kinematic LOS distance of 4.0 kpc. However, it is likely that H I material that traces the Warp has non-circular velocities, and that the Warp begins much closer to us than this. To estimate the distance r_w, we adjust the kinematic distance downwards by a factor of 1.6 (from Fig. 2.1) to obtain r_w $\sim$2.5 kpc, and allow a generous uncertainty of $\pm$0.5 kpc.

If we naively transform distance to velocity using a flat Galactic rotation curve (with R_0=8.0 kpc, and θ_0=220 km s^{-1}) and plot our model alongside the observed $N_{HI}(v)$, a remarkably good correlation is observed (Fig. 2.4). This suggests that, at least for this relatively high latitude direction, a flat rotation curve with these values closely describes the line of sight velocity field, and

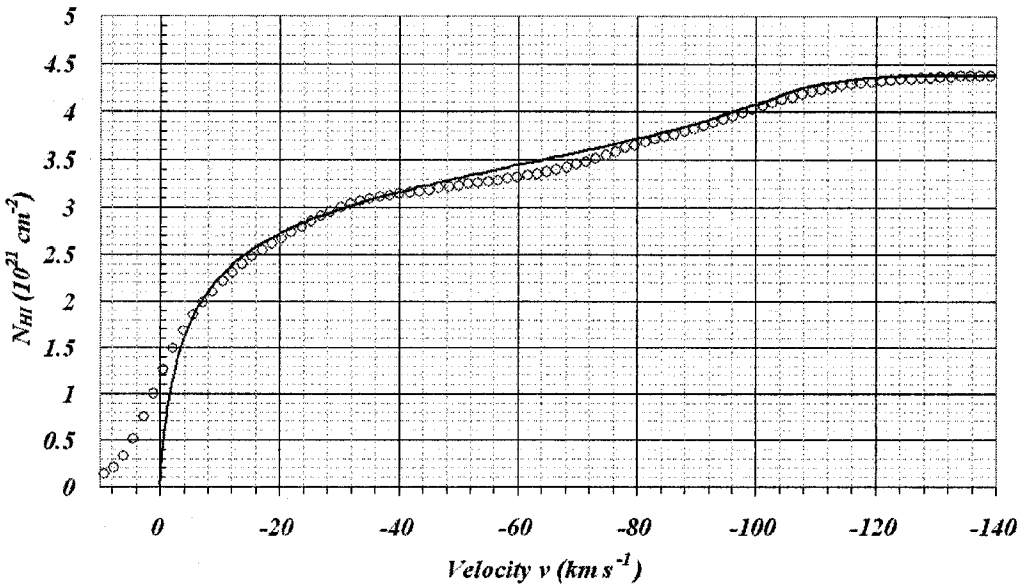

Figure 2.4: The observed curve of cumulative H I column density (calculated via Eqn. 2.13 and plotted as open circles) with LOS velocity towards the SNR DA530 (ℓ=93.3°, b=7°). Our model of $N_{HI}(v(r), \ell, b)$ is also plotted (solid line), after transforming to LOS velocity using a flat model of Galactic rotation (with R_0=8 kpc, θ_0=220 km s^{-1}). The simple distance-velocity mapping gives good results in this relatively high-b case.

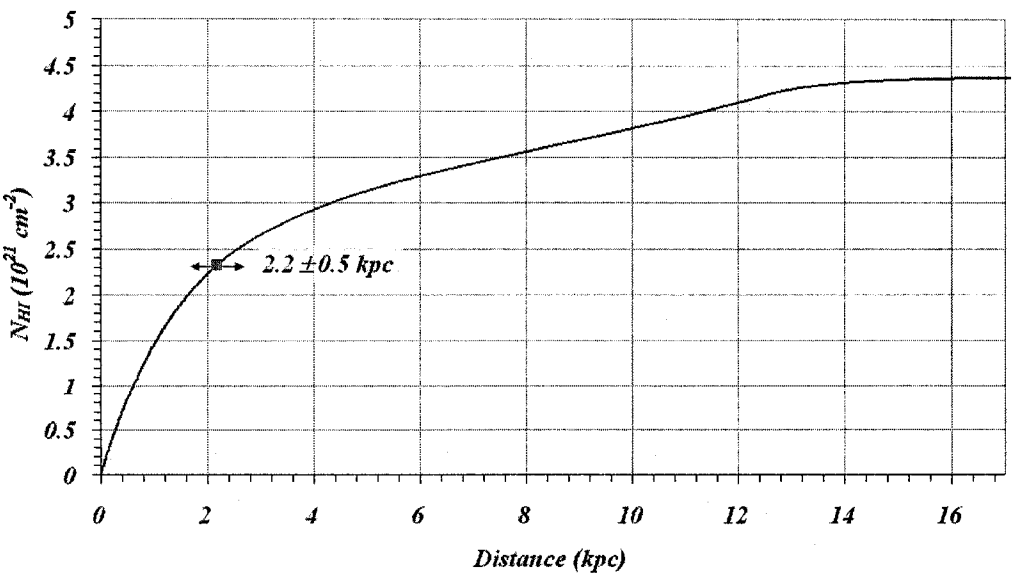

Figure 2.5: The column density versus distance model $N_{HI}(r, \ell, b)$, showing the column depth to DA530 due to neutral hydrogen and the corresponding distance: 2.2 ± 0.5 kpc. See text, Sec. 2.2.

non-circular motions are indeed small.

Integrating to $v = -12$ km s^{-1} in Eqn. 2.11, we find the column density of H I in emission to SNR DA530 to be N_{HI}=2.31 $\pm$ 0.23 $\times$ 10^{21} cm^{-2}. As seen in Fig. 2.5, the distance corresponding in our model to this column density is 2.2 $\pm$ 0.5 kpc, essentially equivalent to the 2.3 kpc predicted by the flat model of Galactic rotation used in Fig. 2.4.

As a second example, we descend closer to the midplane and look at the H I distribution towards H II region Sharpless 121 (ℓ=90.23°, b=1.72°). As catalogued by FBS, the photometric distance to this nebula is 4.8 $\pm$ 1.4 kpc, which FBS have adjusted 25% downward from the original 6.4 kpc of Chini & Wink (1984). FBS also catalogue the ^{12}CO LOS velocity for Sh121 as $v_{obj} = -61$ km s^{-1}. Assuming this velocity is due solely to circular velocities about the Galactic centre, a kinematic distance of 8.2 kpc follows.

Figure 2.6 shows the observed H I emission (open circles) and absorption spectrum (solid line) towards Sh121. The H I emission spectrum is the mean brightness temperature measured in a 0.5° by 0.5° box centred on Sh121. The absorption ($T_{on} - T_{off}$) profile to Sh121 is very weak, but shows that material at velocities more positive than -42 km s^{-1} is absorbing emission from Sh121, and is therefore foreground to the nebula. However, between -42 km s^{-1} and -58 km s^{-1}, $T_{on} - T_{off}$ fluctuates about zero. The weakness of the absorption profile here makes it difficult to judge a location for this gas, so we assume it to be foreground, and add this uncertainty (which totals 0.86$\times$10^{21} cm^{-2}) to that of our measured column density to Sh121, which is calculated as N_{HI}=5.89$\pm$1.04$\times$10^{21} cm^{-2}. Integrating the spectrum in Fig. 2.6 with Eqn. 2.12 indicates a column density of $N_{HI}(r = \infty)$=1.07$\pm$0.11$\times$10^{22} cm^{-2} to the Galactic edge.

Figure 2.7 shows the observed $N_{HI}(v)$ towards Sh121 (open triangles). We begin with a model of $N_{HI}(r, \ell, b)$, made with similar parameters to those used in Fig. 2.5, but now include the Perseus Spiral Arm. A ratio of $n_{0,arm}/n_0$ $\sim$1.3 is estimated from the H I spectrum in Fig. 2.6, and we place the arm's centre initially at R_m=9.6 kpc (e.g. Georgelin & Georgelin 1976), with a width w_{arm}=0.5 kpc and scale height $h_{z,arm}$=0.2 kpc. Transforming $N_{HI}(r, \ell, b)$ to velocity-space with the flat rotation curve of FBS (with R_0=8.5 kpc and θ_0=220 km s^{-1}), we plot the resulting model in Fig. 2.7 (solid dark line) alongside the observed cumula-

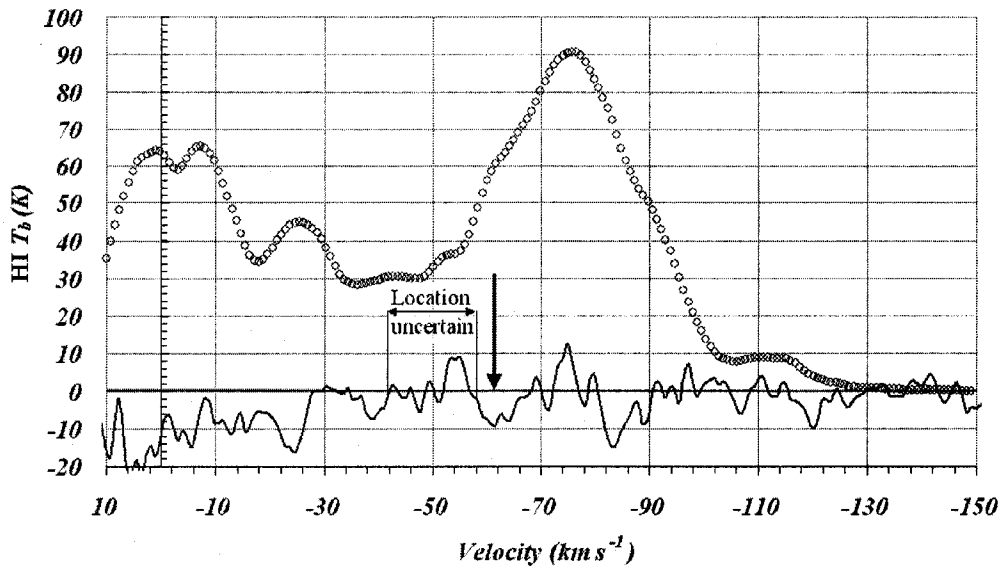

Figure 2.6: The observed H I emission and absorption spectra towards H II region Sh121 (ℓ=90.2°, b=1.7°). Emission is plotted as open circles, and absorption ($T_{on} - T_{off}$) as a solid line. The LOS velocity of ^{12}CO emission associated with Sh121 (-61 km s^{-1}) is marked with a bold arrow. The location (foreground or background relative to Sh121) of H I in the range -42 km s^{-1} $< v <$ -58 km s^{-1} is uncertain, and we assign this uncertainty to the column depth to Sh121. There is an absorption feature seen at -83 km s^{-1} which is most likely shocked H I in an expanding shell surrounding Sh121 (e.g. Kothes & Kerton 2002), and not related to smoothly distributed Galactic H I. H I data are from the CGPS (Taylor et al. 2003).

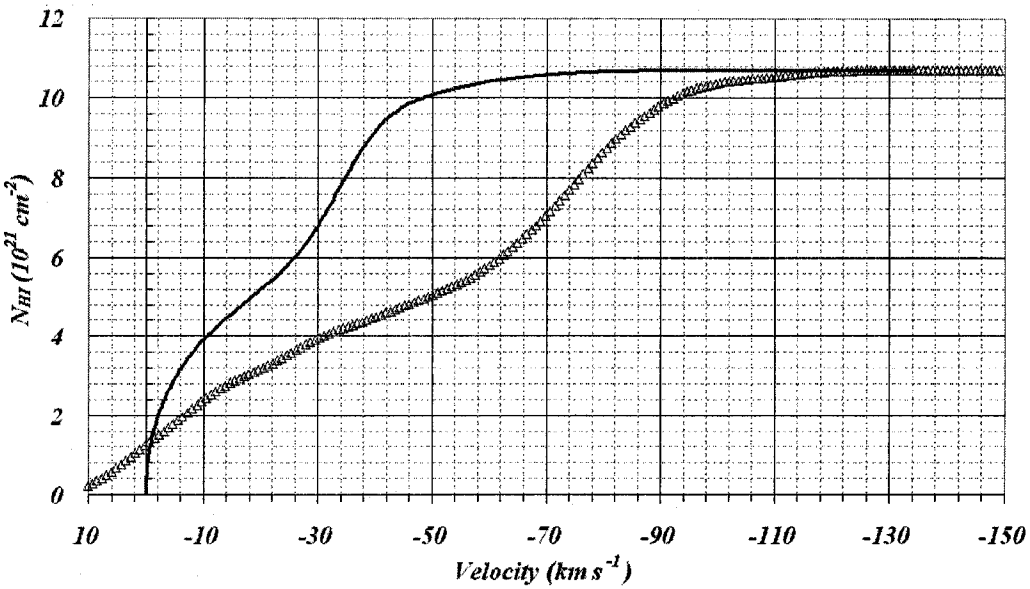

Figure 2.7: The observed cumulative H I column density versus velocity relation $N_{HI}(v)$ towards Sh121 (open triangles), plotted alongside our model of $N_{HI}(v(r), \ell, b)$ (solid line) which has been mapped to velocity space using the flat rotation curve of Fich, Blitz & Stark (1989, with R_0=8.5 kpc, θ_0=220 km s^{-1}). The observed $N_{HI}(v)$ is not reproduced by using a flat rotation curve with these parameters, but requires instead an adjustable mapping between distance and velocity.

tive column density versus velocity $N_{HI}(v)$. The general shape of the model and observed distribution are similar, but obviously using the flat rotation curve of FBS to transform our model into velocity space fails to reproduce the observed $N_{HI}(v)$ relation in this direction.

To transform our model $N_{HI}(r, \ell, b)$ to velocity space, we define a function $v(r)$ to represent the observed velocity-distance relation and choose a cubic function for $v(r)$. In a least squares fitting routine, we allow both the coefficients of $v(r)$ *and* the parameters of the model $N_{HI}(r, \ell, b)$ to vary such that our resulting model $N_{HI}(v(r), \ell, b)$ most closely fits the observed cumulative column density-velocity relation $N_{HI}(v)$. This is accomplished by minimizing the value $\chi^2 = \sum (v_{obs} - v(r))^2 / \sigma_v^2$ where here we take $\sigma_v^2 = (1.3/2)^2 + 2.4^2$ km^2 s^{-2}, where 1.3 km s^{-1} is the velocity resolution of each H I channel map, and 2.4 km s^{-1} the

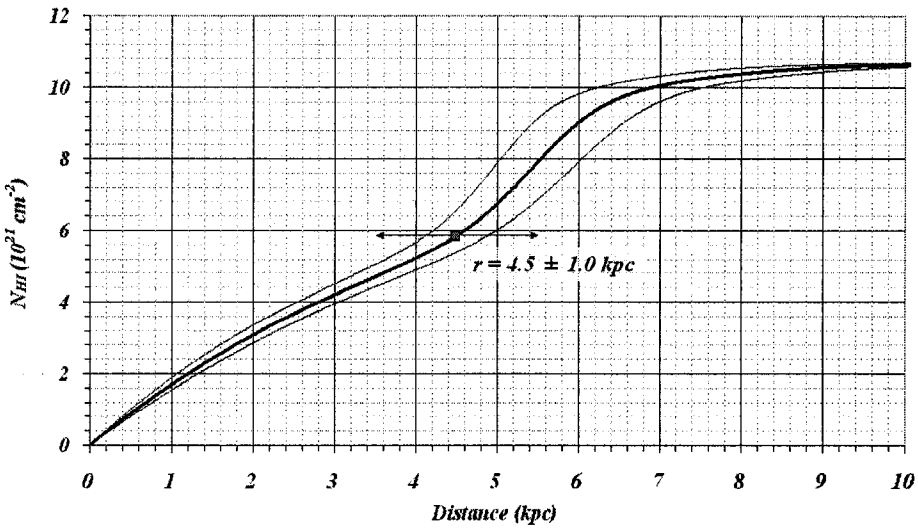

Figure 2.8: The model of cumulative column depth with distance $N_{HI}(r)$ towards ℓ=90.2°, b=1.7°, with the calculated distance to Sh121 (plus uncertainty) labelled. Models which span ±20% uncertainty in all parameters are shown, illustrating the comparatively large distance uncertainty that derives from errors in column densities N_{HI} and $N_{HI}(r = \infty)$. See text, Sec. 2.2.

width of the typical ^{12}CO line associated with an H II region (see Sec. 2.3). For H I spectral features near 0 km s^{-1} we cannot deduce information which describes the distribution of local material, so we give zero weight to data points with positive velocities (which are forbidden for circular rotation at longitudes greater than 90°), and also exclude those $N_{HI}(v)$ points with velocities at which local material is seen (typically 0 km s^{-1} $> v >$ −10 km s^{-1}).

A model of $N_{HI}(r, \ell, b)$ with parameters adjusted for H I towards Sh121 is shown in Fig. 2.8, with the distance to Sh121 produced by our model labelled: r=4.5 ± 1.0 kpc. To achieve a formally acceptable fit (reduced $\chi^2 = 1$) the model parameters did not require much adjustment from the values adopted in Sec. 2.2, and the axisymmetric parameters are similar to those used towards SNR DA530. The final parameters are listed in Table 2.1. We test our model's sensitivity to 20% variations in each of the parameters, and record (in Table 2.1) the resultant change in distance (Δr) for each. The total distance uncertainty for a 20% uncertainty in every parameter (except N_{HI} and $N_{HI}(r = \infty)$) is 0.4

kpc, or only 9% of the distance. The uncertainties in the object's N_{HI} and in $N_{HI}(r = \infty)$ contribute substantially more to the distance error than do those of the parameters.

Figure 2.9 shows the model $N_{HI}(v(r), \ell, b)$ fit to the observed data, and its first derivative, the model H I brightness temperature profile (Eqn. 2.11 mapped to velocity using $v(r)$ and expressed as brightness temperature, in units of Kelvin) overlaid with the original H I spectrum. Note that no attempt was made to fit the synthetic profile to the original spectrum: the profile's good correspondence to the original is evidence of the validity of our model $N_{HI}(r, \ell, b)$, and of the transformation function $v(r)$[5]. The distance to Sh121 produced by our model is in excellent agreement with FBS (1989). This H II region is clearly a resident of the Perseus Spiral Arm (see Figure 2.12 below).

We hereafter present results of the distance method applied to second-quadrant H II regions, and save for a future publication a discussion of the fitting analysis, the implications of the resulting transformation function $v(r)$, and the Galactic structure parameters that come from it.

2.3 Application to Outer Galaxy H II Regions in the Second Quadrant

We present new distances to 29 H II regions (see Tab. 2.2) that reside within the area of the CGPS (74.2°$\leq \ell \leq$147.3°, -3.6°$\leq b \leq$5.6°) observed to date. These nebulae were originally catalogued by Sharpless, and since then observations of each H II region's stellar tenants have added photometric distances for each. We use only regions with photometrically measured distances. Most are selected from the catalogue of FBS (1989), from which we ignore objects with only kinematic distances listed. We find model parameters for each direction (ℓ, b) using CGPS 21 cm H I line data, and use CGPS 2.6 mm ^{12}CO(J=1-0) line data to measure LOS velocities for each object. Finally, we show that our distances match the photometric distances currently held for the H II regions within the

[5]A discussion of the fitted velocity field $v(r)$ towards this direction is presented in Chapter 5.

Parameter	Symbol	Value	Δr (kpc)
Disk scale length in density	h_R	2.0 kpc	0.12
Scale height of H I layer at $R = R_0$	h_0	170 pc	0.05
Rate of increase of H I height with R	h'	30 pc kpc^{-1}	0.01
Radius of middle of Perseus Arm	R_m	9.73 kpc	0.27
Width of Perseus Arm	w_{arm}	0.4 kpc	0.17
Height of Perseus Arm	$h_{z,arm}$	0.2 kpc	0.01
Heliocentric distance Warp begins	r_w	2.5 kpc	0.1
Galactocentric radius of Sun	R_0	8 kpc	0.19
Height of Sun above midplane	$Z_\odot$	15 pc	0.01
Arm/Local density ratio	$n_{0,arm}/n_0$	1.3	-
H I column density to Galactic edge	$N_{HI}(r{=}\infty)$	$1.07 \pm 0.11{\times}10^{22}$ cm^{-2}	0.44
H I column density to Sh121	N_{HI}	$5.89 \pm 1.04{\times}10^{21}$ cm^{-2}	0.78

Table 2.1: Galactic H I distribution model parameters towards Sh121 (ℓ=90.23°, b=1.72°), obtained from the least-squares fit of our model to the observed cumulative distribution in velocity space, $N_{HI}(v)$. The column Δr demonstrates the sensitivity of our model to each parameter, and shows the response in distance (r=4.5 kpc) to a ±20% variation in each model parameter, and to the measured uncertainties in $N_{HI}(r = \infty)$ and N_{HI}.

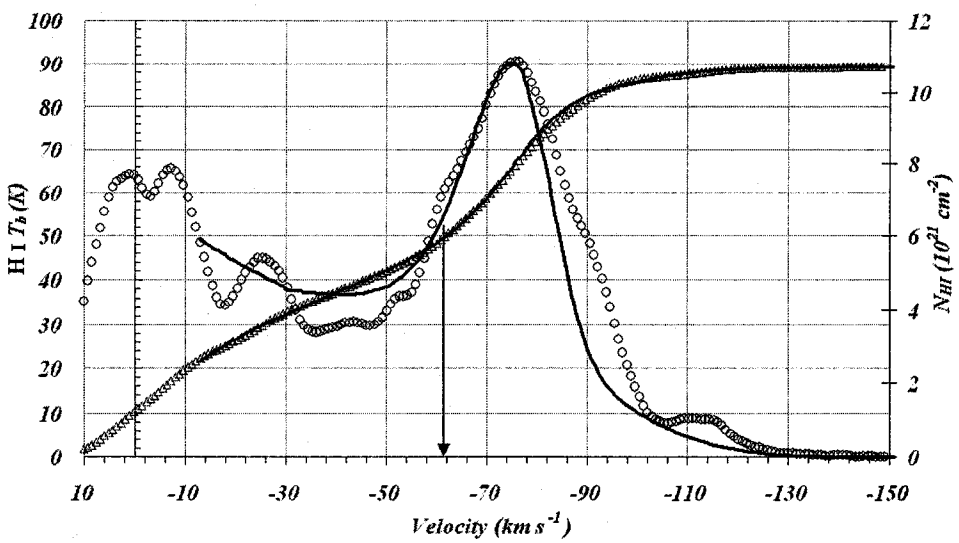

Figure 2.9: The observed cumulative $N_{HI}(v)$ (open triangles) and fitted model $N_{HI}(v(r), \ell, b)$ (solid line) towards Sh121. The quality of the fit is χ^2=1 (reduced chi-squared value). We also show the observed H I emission spectrum (open circles; see Fig. 2.5) with the synthetic H I profile (black solid line) calculated via our model of LOS H I density distribution (Eqn. 2.11). Data at velocities $v > -10$ km s^{-1} are given zero weight in fitting the model $N_{HI}(v(r))$ to the observed distribution $N_{HI}(v)$ (see Figure 2.6), and are therefore excluded. The LOS velocity of Sh121 is indicated (bold arrow). No attempt was made to fit the synthetic profile to the original emission spectrum.

uncertainties of both.

All objects in our sample are known to be associated with molecular material imaged in ^{12}CO emission. For longitudes greater than 102.2°, we confirm this association using ^{12}CO(J=1-0) spectral line emission data from the Five Colleges Radio Astronomy Observatory Outer Galaxy Survey (Heyer et al. 1998), reprocessed for addition to the CGPS database (Brunt et al. 2000). Only four H II regions in our list are found at $\ell < 102.2°$, and for these we use the radial velocities from FBS. A Gaussian function is fitted to each region's ^{12}CO spectral signature, and the object's systemic velocity is assigned as that of the function's peak. We use ^{12}CO velocities for the following reasons: 1) the velocity resolution of CO is typically sharper than other tracers (e.g. recombination line) and 2) ^{12}CO associated with H II regions is expected to be more spatially compact and less turbulent, minimizing the uncertainty in the observed velocity.

For each longitude, we assume that the Galactocentric distance at which the Warp begins (R_w) is constant with respect to the Galactic centre. We use our determination of r_w=2.5 ±0.5 kpc near ℓ=90°, and derive r_w for other directions from Eqn. 1.4 (see Chapter 1).

The errors in our distances (r(FR)) in Table 2.2 are *limit* errors, and are derived from uncertainties in the following parameters: N_{HI} (±10%), v_{obj}(± 2.4 km s^{-1}), $N_{HI}(r = \infty)$ (±10%), r_w (±0.5 kpc), h_R (±0.5 kpc), h_0 (±50 pc), and R_m (contributing ±0.5 kpc along the LOS). For example, allowing the uncertainty in scale length parameter h_R to be ±0.5 kpc (±20% for a scale length of 2.5 kpc, typical of our results) for individual lines of sight changes the distance to an object by only 5-10%. Varying parameters other than those above is not found to significantly change the distance measurement, so we ignore their contributions to δr. We measure a velocity dispersion for the ^{12}CO line associated with each H II region that is typically $\delta v = \pm 2.4$ km s^{-1}, and allow this to contribute to δN_{HI}, and hence the distance uncertainty as well. The bulk of the distance error descends from this, plus the ±10% uncertainty in the absolute brightness temperature calibration of the H I data, which affects both N_{HI} and $N_{HI}(r = \infty)$. The final uncertainty in distance due to all contributions is typically ±20%.

As demonstrated earlier towards Sh121, a fitting routine that minimizes the difference between the observed $N_{HI}(v)$ and model $N_{HI}(v(r), \ell, b)$ was performed

Sharpless Catalog no.	ℓ (°)	b (°)	v_{obj} km s^{-1}	N_{HI} 10^{21} cm^{-2}	N_{HI} $(r=\infty)$ 10^{21} cm^{-2}	r (FBS) kpc	r (Other) kpc (Ref.)	r (FR) kpc
121	90.23	1.72	−60.9	5.89	10.72	4.8±1.4		4.5±1.0
124	94.57	−1.45	−43.4	4.09	5.86	2.6±0.6		2.8±0.4
127	96.27	2.57	−94.7	7.99	9.44	7.3±2.3		6.0±1.5
128	97.56	3.16	−72.5	6.10	9.93	6.2±2.3	4.8 (3)	4.8±0.5
132	102.96	−0.8	−49.3	4.40	6.40	4.2±1.5	3.6 (1)	3.2±0.5
134	103.72	2.18	−16.3	2.34	8.26	0.9±0.3		1.3±0.4
135	104.59	1.37	−20.8	2.84	8.60	1.4±0.4		1.5±0.4
139	105.77	−0.15	−46.0	3.47	6.71	3.3±1.1	2.6 (2)	2.8±0.4
140	106.81	5.31	−8.1	1.80	6.03	0.9±0.1		1.0±0.3
142	107.28	−0.9	−41.4	2.94	6.10	3.4±0.3	2.4 (1)	2.4±0.3
152	108.75	−0.93	−50.6	4.30	6.35	3.6±1.1		2.8±0.4
154	109.17	1.47	−11.9	2.70	8.14	1.4±0.4		1.5±0.4
155	110.22	2.55	−10.0	2.02	8.95	0.7±0.1		0.9±0.3
156	110.11	0.05	−52.0	4.75	7.40	6.4±2.0	3.2 (3)	2.7±0.4
157	111.28	−0.66	−43.4	3.68	7.29	2.5±0.4		2.2±0.4
158	111.54	0.78	−56.4	5.60	7.56	2.8±0.9		3.2±0.6
159	111.61	0.37	−56.0	5.63	7.62	3.1±1.2		3.0±0.6
161	111.89	0.88	−50.7	4.81	7.56	2.8±0.9		2.9±0.6
162	112.23	0.24	−45.0	3.80	7.20	3.5±1.1	2.6 (4)	2.5±0.4
163	113.52	−0.57	−45.3	4.56	7.29	2.3±0.7		2.6±0.4
165	114.65	0.14	−34.0	3.16	7.57	1.6±0.5		1.9±0.4
169	115.79	−1.65	−41.0	3.32	6.48		2.3 (2)	2.3±0.2
170	117.57	2.26	−45.2	3.14	7.40	2.3±0.7	2.2 (1)	2.5±0.5
173	119.4	−0.84	−37.2	2.96	6.21	2.7±0.9		2.2±0.4
175	120.36	1.97	−49.9	4.02	8.26	1.7±0.5	2.7 (2)	2.7±0.4
177	120.63	−0.14	−34.6	2.88	7.68	2.5±0.8	2.4 (1)	2.0±0.3
190	133.71	1.21	−40.9	4.07	8.22	2.1±0.2	2.3 (1)	2.3±0.4
199	138.3	1.56	−38.6	4.28	8.27	2.1±0.2	2.3 (1)	2.2±0.4
202	139.99	2.09	−8.9	1.42	6.38	0.8±0.3		0.7±0.3

Table 2.2: The 29 Galactic H II regions used for this study, along with photometric distances and those predicted by our method. The velocities v_{obj} are those of ^{12}CO emission associated with the object, and are uncertain by typically ±2.4 km s^{-1}. Integrated column densities to each object are additionally uncertain by ±10%. Column 7 shows photometric distances from Fich, Blitz & Stark (FBS, 1989). Sh169 is not assigned a photometric distance by FBS, but is by Roberts (1972) and therefore is quoted in column 8 (Other), which shows other photometric distances from the literature differing from FBS. References for the other distances in column 8 are (1) Georgelin & Georgelin 1976, (2) Roberts 1972, (3) upper-limit method of Dewdney et al. 1991 (see Sec. 4), and (4) Humphreys 1978. Column 9 lists the results of our distance method (FR).

for each H II region. With a few exceptions, the majority of observed H I spectra cannot be fitted to the level $\chi^2 \approx 1$, as most spectra contain moderately bright and well-resolved H I structures that are not accounted for in the smooth features we model. However, in all directions, the overall shapes of the observed $N_{HI}(v)$ relations are consistent with our models.

Towards each object, we allow only the parameters h_R, h_0, R_m, h', $h_{z,arm}$ and w_{arm} to vary in the χ^2 minimizing process, and hold fixed r_w, R_0, and $Z_\odot$. It was found that values for the parameters h_R=2.5 kpc, h_0=200 pc and h'=30 pc kpc^{-1} produce a good starting fit for each line of sight, and the parameter $h_{z,arm}$ did not significantly vary from ~0.2 kpc. These parameters are nearly constant over our working range of 50° longitude, and they do not vary significantly between adjacent directions or wander towards unphysical or unreasonable values. In all cases it was found that the calculated distance to an object would change by very little compared to the uncertainty as the value of χ^2 approached a minimum; thus tuning the model parameters to precisely fit the model to the observed cumulative column density $N_{HI}(v)$ is not crucial for distance estimates, and for this study was not done.

Columns in Table 2.2 present the following information for each H II region: 1) Sharpless catalog number, 2) Galactic longitude, 3) Galactic latitude, 4) ^{12}CO LOS velocity, 5) H I emission column density to the object, 6) H I emission column density to the Galactic edge in this direction, 7) photometric distance and uncertainty from FBS (1989), 8) Other distances from referenced authors, and 9) our method's distance measurement and uncertainty.

2.4 Discussion and Conclusions

Figure 2.10 shows the greatly improved linear correlation between the photometric distances from FBS (1989) and distances calculated by our method (cf. Fig. 2.1). The correlation of our distances with those of FBS (the slope in Fig. 2.10) is 0.88:1, revealing a small conservative tendency in our distance measurements and/or an inherent overestimate in the FBS distances.

We find a few H II regions for which FBS distances do not agree with ours within the uncertainties. Most outstanding is Sh156 (ℓ=110.11°, b=0.05°, v_{obj} =

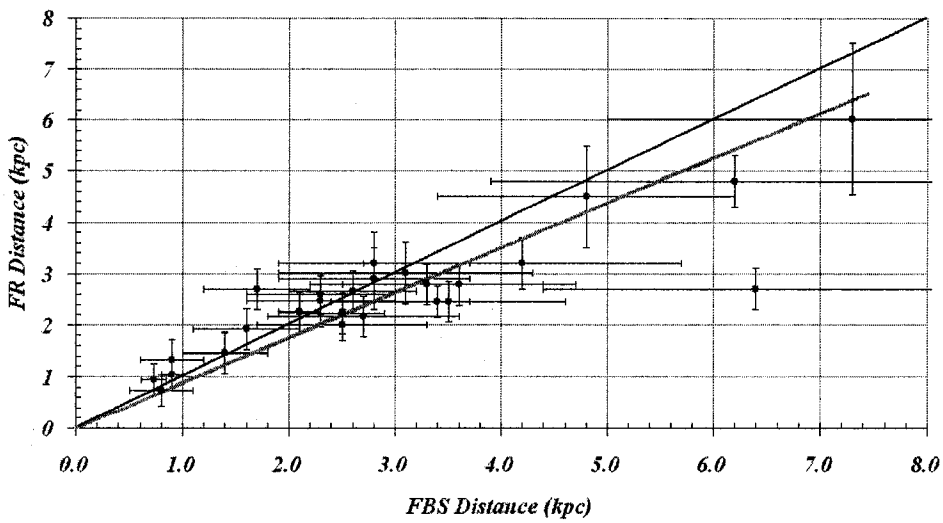

Figure 2.10: Comparison of 28 H II region distances calculated by our method (FR) with photometric distances of Fich, Blitz & Stark (1989). A line of slope unity is shown as a thin black line, and the mean correlation of 0.88:1 is observed in the thick grey regression line.

-52 km s^{-1}, r (FR)=2.7±0.4 kpc), which FBS list as 6.4±2.0 kpc from the Sun, exceeding even the kinematic distance (5.2 kpc). We have several reasons to be skeptical of their distance. Sh156 has been observed in ammonia emission by Wouterloot et al. (1988), who adopted a distance of 3.5 kpc. Using a technique originally suggested by Dewdney et al. (1991) as an estimator of stellar luminosity, and modified by Kerton (priv. comm. 2003) to give an upper limit on distances to H II regions, we estimate an upper-limit distance to Sh156. The technique requires that one measure both the ionizing luminosity (from the observed 21 cm radio flux density) and the total infrared luminosity (from flux densities in each of the four IRAS bands). Both values depend on the square of the source distance, hence the ratio of these observables is distance-independent. The well-established calibration of Lyman continuum photon fluxes for upper main-sequence stars (Panagia 1973) is used to find the absolute total luminosity of the exciting star. Kerton has extended the use of the above ratio to estimate distance, the underlying assumption being that all UV

photons from the embedded stellar flux are reprocessed into IR emission. One uses the absolute luminosity together with the apparent luminosity (calculated from either the 21 cm or IR data) to find distance. This estimate is an upper limit, since an error in the assumption would mean that some ionizing photons escape absorption by dust, causing the ratio of UV-to-IR flux (and hence the distance) to be overestimated. Assuming an electron temperature of T_e=10^4 K, we obtain an upper-limit distance of r=3.2 kpc for Sh156, one-half of the FBS distance, and much more consistent with our calculated value of 2.7±0.4 kpc.

Similarly outstanding is Sh128 (ℓ=97.56°, b=3.16°, v_{obj} = −72.5 km s^{-1}), reported by FBS to be 6.2±2.3 kpc distant. The radio-IR approach gives an upper limit of 4.8 kpc, consistent with our calculated value of 4.8±0.5 kpc.

Column 8 in Tab. 2.2 lists distances published by other authors (referenced) which differ from those adopted by FBS. Half of these distances are photometric, and are from Georgelin & Georgelin (1976). Generally, these distances are lower than the FBS values, and more consistent with our distances. Where no other distance for an H II region is found in the literature, we use that of FBS. Figure 2.11 shows the correlation between the distances of Column 8 (or Column 7 if Column 8 is blank) in Table 2.2, and ours. The scatter about a common line is less than in Fig. 2.10, and the correlation is closer to unity (0.94:1). We interpret these improved results as evidence that the distances of FBS are moderately too high.

As we do not include a model component to trace the Local Arm feature, the distances calculated for the very nearby objects will likely be upper limits. If H I near to the Sun is concentrated in a local feature (such as that included in the electron density model of Taylor & Cordes, 1993), then the true run of column density with distance will initially increase more rapidly with distance than predicted by our model, which traces only the smooth axisymmetric component of the local H I. This distance overestimation is not severe, however, and Table 2.2 shows that our distances to local (≤1 kpc) H II regions agree with their photometric estimates within the uncertainties in both.

All Perseus arm H II regions are found to be much nearer than their kinematic distances suggest. To explain this, it is instructive to refer to the Two-Arm Spiral Shock (TASS) model (Roberts 1972) for the Perseus spiral arm (see Chap-

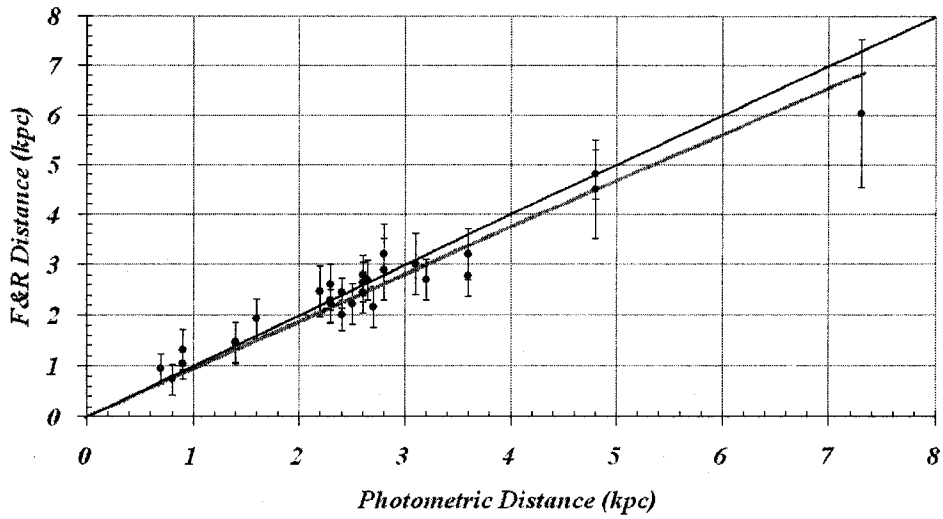

Figure 2.11: Same as Fig. 2.10, but with photometric distances from other authors (Column 8 in Table 2.2) replacing the FBS distances (where both exist). The overall scatter is much less, and the correlation (0.94:1) is improved.

ter 5, Fig. 5.4 for a schematic description). For example, in the direction of Sh156 ($\ell = 110°$) the shock is located roughly 2.7 kpc from the Sun (a spatial uncertainty of order $\pm$400 pc or greater is assigned by Roberts), and in LOS-velocity vs. distance plots, the shock and its effects stretch 1 kpc along the LOS. Our distance of 2.7$\pm$0.4 kpc for Sh156 places it within the influence of the Perseus Arm shock. Further, the observed LOS velocity of this H II region ($v_{obj} = -52$ km s^{-1}) places it directly atop the shock ridge predicted by Roberts' model of H I distribution towards ℓ =110°. A non-circular "shock" velocity of -23 km s^{-1} for Sh156 is predicted by our distance, and this is well explained by the TASS model towards ℓ=110-115° (Fig. 7 in Roberts' paper). Similar shock velocities of magnitude $\sim$19 to 23 km s^{-1} are found for other distant H II regions near this longitude (e.g. Sh152, Sh157 through Sh163).

Referring to Table 2.2 shows that the distances our method produces tend to divide the H II regions into two distinct distance groups: 1) "Local Arm" objects (0.7 kpc $\leq r \leq$1.5 kpc), and 2) "Perseus Arm" residents ($r \sim$2 kpc and greater). A plot of heliocentric distance versus longitude (Figure 2.12) shows this duality.

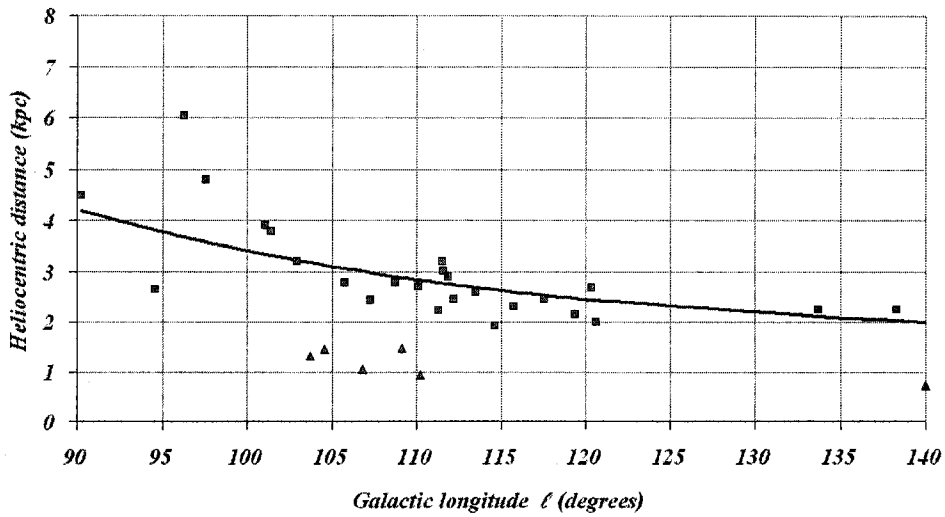

Figure 2.12: The spatial distribution of 29 H II regions with respect to the Sun throughout the longitude range 90° $< \ell <$140°. Heliocentric distances have been calculated using the method presented in this paper. Two distinct collections of nebulae are seen: local nebulae that cluster near the Sun are marked with filled triangles, while those belonging to the Perseus Arm are shown as filled squares. The solid line is a simple model of a logarithmic spiral arm (Eqn. 2.14 with pitch angle i=10°), and has not been fitted to the data.

The Perseus Arm grouping (group 2) is quite tight above ℓ=100°, and somewhat wider for the four regions at longitudes 90° $\leq \ell \leq$100° (see Fig. 2.12). To illustrate group 2, on Fig. 2.12 we overlay a simple model of a logarithmic spiral arm, calculated from:

$$R(\phi) = R(\phi_0) exp\left((\phi_0 - \phi) tan(i)\right) \tag{2.14}$$

where $R(\phi_0)$ is the arm's Galactocentric radius towards azimuth angle ϕ_0. We use $R(\phi_0)$ ~9.0 kpc towards ℓ=90° as in Roberts' TASS model (1972), and the pitch angle of the arm i is assumed constant at 10°. This model is not in any way further manipulated to fit the points in Fig. 2.12. The H II regions in group 2 are seen to be distributed evenly around this model of the Perseus Arm, a remarkable result that would seem to support the distances we measure, and the method in general.

This work is being continued by the authors, finding new distances for ob-

jects throughout the second quadrant, and using the technique to map the outer Galaxy's velocity field and its relation to distance, thereby revising the Galactic rotation curve.

The authors thank Tom Landecker of DRAO for his original encouragement and kind feedback on this work, and Chris Brunt, Charles Kerton, Lewis Knee and Roland Kothes (also of DRAO) for their interest and very helpful discussions throughout its development. We also thank Douglas Hube (University of Alberta) for thoughtful contributions so necessary to this project. The Dominion Radio Astrophysical Observatory is operated as a national facility by the National Research Council of Canada. The Canadian Galactic Plane Survey is a Canadian project with international partners, and is supported by a grant from the Natural Sciences and Engineering Research Council of Canada (NSERC). This work has been supported by NSERC operating grants to T. Landecker, D. Routledge, D. Hube, and S. Morsink. T. Foster has been supported by an NSERC Graduate Scholarship.

Bibliography

[1] Binney, J., & Merrifield, M. 1998, Galactic Astronomy, (New Jersey: Princeton University Press)

[2] Brunt, C. M., Ontkean, J., & Knee, L.B.G. 2000, BAAS, 197, 508

[3] Burton, W. B. 1988, in Galactic and Extragalactic Radio Astronomy, eds. G. L. Verschuur & K. I. Kellermann, Springer-Verlag, New York, 295

[4] Burton, W. B. 1985, A&AS, 62, 365

[5] Chen, B., Figueras, F., Torra, J., Jordi, C., Luri, X., & Galadí-Enríquez, D. 1999, A&A, 352, 459

[6] Chini, R., & Wink, J. E. 1984, A&A, 139, 5

[7] Dewdney, P. E., Roger, R. S., Purton, C. R., & McCutcheon, W. H. 1991, ApJ, 370, 243

[8] Diplas, A., & Savage, B. D. 1991, ApJ, 377, 126

[9] Fich, M., Blitz, L., & Stark, A. A. 1989, ApJ, 342, 272 (FBS)

[10] Gathier, R., Pottasch, S. R., & Pel, J. W. 1986, A&A, 157, 171

[11] Georgelin, Y. M., & Georgelin, Y. P. 1976, A&A, 49, 57

[12] Gibson, S. J., Taylor, A. R., Higgs, L. A., & Dewdney, P. E. 2000, ApJ, 540, 851

[13] Heyer, M. H., Brunt, C., Snell, R. L., Howe, J. E., Schloerb, F. P., & Carpenter, J. M. 1998, ApJS, 115, 241

[14] Humphreys, R. M. 1978, ApJS, 38, 309

[15] Humphreys, R. M., & Larsen, J. A. 1995, AJ, 110, 2183

[16] Kerton, Charles. 2003, private communication

[17] Kothes, R., & Kerton, C. 2003, A&A, 390, 337

[18] Landecker, T. L., Routledge, D., Reynolds, S. P., Smegal, R. J., Borkowski, K. J., Seward, F. D. 1999, ApJ, 527, 866

[19] Méndez, R., & van Altena, W. 1998, A&A, 330, 910 (M&vA)

[20] Merrifield, M. R. 1992, AJ, 103, 1552

[21] Panagia, N. 1973, AJ, 78, 92

[22] Parenago, P. P. 1945, Russian AJ, 22, 129

[23] Reid, Mark J. 1993, ARA&A, 31, 345

[24] Roberts, W. 1972, ApJ, 173, 259

[25] Robin, A. C., Crézé, M., & Mohan, V. 1992, ApJ, 400, L25

[26] Rohlfs, K., & Wilson, T. L. 1996, Tools of Radio Astronomy, (2nd ed.; Berlin: Springer-Verlag)

[27] Schlegel, D. J., Finkbeiner, D. P., & Davis, M. D. 1998, ApJ, 500, 525

[28] Spitzer, Lyman Jr. 1942, ApJ, 95, 329

[29] Taylor, J. H., & Cordes, J. M. 1993, ApJ, 411, 674

[30] Taylor, A. R., Gibson, S. J., Peracaula, M., Martin, P. G., Landecker, T. L., Brunt, C. M., Dewdney, P. E., Dougherty, S. M., Gray, A. D., Higgs, L. A., Kerton, C. R., Knee, L. B. G., Kothes, R., Purton, C. R., Uyaniker, B., Wallace, B. J., Willis, A. G., & Durand, D. 2003, AJ, 125, 3145

[31] Wouterloot, J. G. A., Walmsley, C. M., & Henkel, C. 1988, A&A, 203, 367

Chapter 3

The Galactic Plane Region near ℓ=93° II: A Stellar Wind Bubble Surrounding SNR 3C434.1

Foreword

This chapter demonstrates two accomplishments of this thesis. The usefulness of the method described in Chapter 2 is shown, calculating an accurate new distance for a newly discovered supernova remnant 3C434.1 (SNR)/stellar wind bubble pair. As well, the chapter demonstrates the benefit of combining radio and optical observations. All text in this chapter has been accepted for publication in the journal Astronomy & Astrophysics, 2003. Nothing has been modified from the original paper. My supervisor Dr. David Routledge, and colleague Dr. Roland Kothes (of DRAO) appear as co-authors.

The previously catalogued SNR 3C434.1 appears confined by a shell of neutral hydrogen, which is observed to have a very high systemic velocity ($v_{LOS} \sim -80$ km s^{-1}). Using the rotation curve of FBS (1989), this would indicate the SNR is at an extraordinary distance of 10 kpc (R=13.6 kpc) and has a physical span of 80 pc. However, it appears in velocity space at a similar velocity as the Perseus Spiral Arm which, as traced by H II regions, is 4-5 kpc away in this direction (e.g. Georgelin & Georgelin 1976). The SNR's progenitor (an O4 star) must have been born into an OB association formed in a spiral arm, and its remnant should appear there as well. An apparent conflict therefore exists between the kinematic distance and the "most likely" position. This conflict is resolved by the new distance of 5.2 kpc calculated here.

A cautionary note on the uncertainty of SNR distance calculators is worthwhile. The calibration for the controversial Σ-D method for estimating shell-type SNR distances has been derived by many authors (e.g. Clark & Caswell 1976), and disputed by others (e.g. Green 1984). A very recent determination comes from Case & Bhattacharya (1998), who have derived a new Σ-D relation with kinematic distances to Galactic SNRs (using the flat rotation curve of FBS 1989). This calibration also predicts 3C434.1 to be 5.2 kpc distant, but also suggests the nearby remnant DA530 ($\ell = 93.3°, b = 6.9°$) to be 6.6 kpc distant, nearly three times its kinematic distance and 800 pc out of the plane! Clearly, SNR distances are sufficiently unknown quantities that any distance method for them, no matter how welcome, should be approached with caution.

With a proper distance calculated to 3C434.1, the physics, dynamics and time

history of the H I shell that surrounds 3C434.1 is presented in great detail in the following original study. It is my hope to establish the usefulness of the distance method, particularly on SNR objects, and the inclusion of this research in these pages furthers this goal.

Abstract

New Canadian Galactic Plane Survey λ21 cm H I line observations towards supernova remnant (SNR) 3C434.1 (G94.0+1.0) are presented. We find a fragmented and thin-walled atomic hydrogen shell inside which the SNR is seen to be contained at $v \simeq -80$ km s^{-1}, which we report to be a highly evolved stellar wind bubble (SWB) associated with the remnant. A dark area in the midst of otherwise bright line emission is also seen near -71 km s^{-1}. An absorption profile to the extragalactic continuum source 4C51.45 (superimposed on the shell's north face) allows us to probe the shell's optical depth, kinetic temperature and expansion velocity. The material in the dark area has the same properties as material in the fragmented shell, suggesting that the dark area is actually the far-side "cap" of the shell seen absorbing emission from warm background gas, the first instance of H I Self Absorption (HISA) seen in such a structure. We show that the kinematic distance of 10 kpc derived from a flat Galactic rotation model is highly improbable, and that this bubble/SNR system is most likely resident in the Perseus Spiral Arm, lying 5.2 kpc distant. We model the SWB shell in three dimensions as a homologously expanding ellipsoid. Physical and dynamical characteristics of the bubble are determined, showing its advanced evolutionary state. Finally, from a photometric search for one or more stars associated with the SWB, we determine that three B0V stars and one O4V star currently inhabit this bubble, and that the progenitor of 3C434.1 was at latest also an O4 type star.

3.1 Introduction

The supernova remnant (SNR) 3C434.1 (ℓ=94°, b=1°) is one of two remnants in the Galactic plane region near ℓ=94°, and is seen among a collection of thermal objects. It appears as a radio continuum shell of radius 14 arcminutes, smaller than most shell-type remnants visible in the Canadian Galactic Plane Survey (CGPS, Taylor et al. 2003). The 21 cm continuum appearance of this object is similar to the neighboring H II region NRAO 655, discussed by Foster & Routledge (2001, Paper I). The space between these two objects appears filled by dim continuum emission, and the objects appear bridged by this nebulosity. We study the remnant's multi-wavelength appearance in emission and its relationship with NRAO 655 no further here, but in a future publication. In this present paper we report a thorough examination of the neutral material surrounding this SNR, and submit that it is in reality a distant SNR/Stellar Wind Bubble (SWB) pairing.

Stellar winds carve much of the sponge-like structure of neutral hydrogen observed in the interstellar medium. Most of the originators of these winds, including SNR precursors, tend to cluster in associations, and it is thus not surprising to find SNRs evolving into environments greatly modified by groups of massive stars. The legacies of OB star groups are large interstellar cavities, surrounded by expanding outer shells, whose edges are often delineated by swept-up neutral hydrogen, and are thus observable in the H I spectral line. We expect pairings of supernova remnants with H I shells cloaking OB associations to be particularly common within the Galactic spiral arms, where the SNR progenitors and their siblings have formed.

A fine example of a cavity evacuated by an OB cluster and containing an SNR formed within it is seen in the H I environment surrounding the nearby SNR G106.3+2.7 (Kothes et al. 2001). Those authors suggest the formation of the progenitor was triggered by the stellar winds and supernova explosions of cluster members.

We present the discovery of a distant shell of cold atomic hydrogen that surrounds 3C434.1, and show that it is likely an old SWB carved out mainly by two O-type stars, one of which was the progenitor of 3C434.1. The foreground col-

umn density is found and hence the distance to the shell and its linear extent, using the new distance technique of Foster and Routledge (2003) (see Sec. 3.3 below). The availability of high-resolution CGPS continuum and H I spectral line data allows observation of the bubble's physical structure, and for the first time neutral material of a stellar wind bubble is seen absorbing emission from warm H I gas behind it. The cold gas of the shell is also seen to absorb emission from the bright and auspiciously located radio continuum point source 4C51.45, allowing confirmation of parameters and expansion velocity calculated for the shell from emission data. The dynamics and time history of this SWB are modeled and discussed in detail. Finally, from deep UBV photometric observations of stars towards 3C434.1, four stars are identified as candidates for association with the SWB, and the physical effects of this cluster discussed.

3.2 Observations

3.2.1 1420 MHz HI Line Observations

The field of 3C434.1 was observed in the 1420 MHz continuum and 21 cm line with the Synthesis Telescope (ST) at the Dominion Radio Astrophysical Observatory (DRAO). The continuum and atomic hydrogen line observations were centred on (ℓ,b) = (93.47°, 1.00°) and are part of the CGPS, a project by a consortium of researchers from five countries to map a large segment of the northern Galactic plane in radio and infrared wavelengths at a resolution approaching 1 arcminute (Taylor et al. 2003). The field of view is 3.1 degrees at 21 cm to the 10% level. The FWHM of the beam achieved by the ST is $57'' \times 57''$ cosecδ in the 1420 MHz continuum. H I line images have 1.1 arcminute resolution in each of 256 channels, and are separated by 0.824 km s^{-1}, with a velocity resolution of 1.3 km s^{-1}. The H I line data have intensity uncertainty due to calibration of $\pm$10%, and the continuum data, $\pm$5%. Other relevant parameters of the telescope and data reduction procedures are given in Sec. 2.1 in Paper I, and further instrumental detail can be found in Landecker et al. (2000).

To depict ISM structures accurately in the CGPS radio continuum and H I line images (especially those of large angular size), missing short-spacing in-

formation is routinely added to each ST map. The data are obtained from the Effelsberg 21 cm Galactic Plane Survey (Reich et al. 1997) and an H I line survey of the plane made with the DRAO 25.6 m paraboloid (Higgs & Tapping 2000).

3.2.2 Optical Observations

On 2001 August 9, and 2001 November 18, 407 stars in a $27' \times 27'$ field towards ℓ=94°, b=1° (field 1) were observed with the 0.5 m optical telescope at the University of Alberta's Devon Astronomical Observatory (Foster et al. 1999). Two separate nights' observations were performed to compare the consistency and assess the final quality of the photometry. A second field (field 2) was also observed (332 stars towards $\ell = 93.70°, b = 1.45°$) for another study, and overlaps some of the SWB interior, and we include the field here. UBV filters with optimal passbands for CCDs (as determined by Bessel, 1990) were used. The low quantum efficiency of the CCD in the U-band (λ_U=365 nm) limits the faintest magnitude measured in the sample of stars, and to increase this limit, an average U-band frame was made from nine separate 600 second integrations. Each frame was taken at slightly different altitude (and hence airmass), and we have used the following technique to create a photometrically accurate single frame from many individual ones.

After basic CCD image processing (including removal of cosmic ray strikes and bad pixels), a uniform background level (in analog-digital units, or ADU) for each target frame is determined. This level is subtracted from individual frames. First-order extinction coefficients k'_λ (in units of ADU per unit airmass) for each wavelength are determined from observations of bright northern standard stars (Oja 1996). Stellar fluxes in each frame are then corrected to a common airmass X of zero by multiplying the frame by the factor $10^{k'_\lambda X_{observed}/2.5}$. In this way, the flux is corrected to extra-atmospheric values without affecting the background, which tends to be mostly due to auroral skyglow in our location. Each frame is shifted to a common centre, and a mean image (corrected for atmospheric extinction) is made.

This technique permits accurate photometry to be obtained for very faint stars with modest-sized telescopes: the limiting magnitude for our sample in-

creased to $m_V = 16.6$, compared to a limiting magnitude of $m_V = 14.6$ using a single 600 second U-band integration. Nine standard stars from Oja (1996) were also observed to derive coefficients and zero-point values for transformation of our magnitudes and colours to the Johnson system. Two of these stars (early A-type) were also used as extinction candles, and were observed at varying elevations throughout the night. Extinction and transformation coefficients were very well determined: mean absolute differences between the standard stars' published and measured V, $B-V$, and $U-B$ values are 0.032, 0.018, and 0.036 magnitude, respectively. As a further check of the quality of our photometry we identified 12 stars in field 1 and 24 stars in field 2, present in the Tycho Catalogue (Høg et al. 2000), as observed by HIPPARCOS. Mean absolute differences between DevonAO and Tycho photometric values (transformed to Johnson's system) were 0.11 mag and 0.13 mag in $B-V$ and V respectively (for field 1), and 0.18 mag and 0.15 mag (field 2).

The $U-B$ versus $B-V$ two-colour diagram was used, along with the reddening curve $E(U-B)/E(B-V) = 0.72+0.05E(B-V)$ and the optical parameter $R_V = A_V/E(B-V) = 3.1$ to derive unreddened colour indices. 93 of the 407 field 1 stars have uniquely determined dereddened colours, as do 83 of the 332 field 2 stars. These are principally O and B-type spectral classes. In determining their unreddened colours and distances, we used the colour index and absolute magnitude M_V calibration of hot stars tabulated in Cox (2000). Calibration for early-type stars is more certain than for cooler stars (Gathier et al., 1986), and less error in distance is introduced by uncertainties of a star's luminosity class. Nevertheless, one can expect at least ± 0.3 magnitudes of uncertainty in M_V for O and early B type stars (Russeil 2003). Luminosity Classes (LC) of the stars cannot be firmly determined with UBV photometry alone, although it is almost certain that the majority are LCV. For the purposes of finding candidate stars for association with the shell around 3C434.1 (see Sec. 3.5) we assume all stars are dwarfs.

3.3 A Shell of Neutral Hydrogen Around 3C434.1

In Fig. 3.1, we present a montage of velocity-channel images of neutral hydrogen towards ℓ=94°, b=1°. The angular resolution of each of these maps is 2 arcminutes. This H I is visible as a ring of emission surrounding the SNR's radio continuum boundary, in H I channel images between -76.5 km s^{-1} and -81.0 km s^{-1}, and has the appearance of a fragmented, roughly circular shell, containing the SNR. The ring's mean thickness is 2 arcminutes (measured from original 1′ resolution data). The radius of this feature is approximately 21 arcminutes, which is 7 arcminutes larger than the radius of the continuum shell of 3C434.1. Fig. 3.2 shows this size relationship well with H I emission summed over three individual channels, centred on -79.5 km s^{-1}.

Figure 3.2 shows the bubble's perimeter is fairly well defined around most of its eastern half. Its curvature is similar to the SNR's eastern boundary, and the remnant may be interacting with the material of the H I shell in this region. 3C434.1 is seen as a shell-type SNR in radio continuum, and such emission must be produced by interaction with a dense medium, in this case the inside edge of the H I bubble within which it is evolving. There is fairly good definition in the west edge as well especially at -79 km s^{-1} to -81.0 km s^{-1}, though the H I shell edge is similarly fragmented. We show in Sec. 3.4 that this elliptical ring of H I (see Figure 3.6) is most likely material accumulated by an expanding stellar wind bubble (SWB), formed by a cluster of early type stars (including the SNR's progenitor) and inside which 3C434.1 is evolving.

3.3.1 Absorption of Continuum Emission by the H I Shell

The radio source 4C51.45 ($\ell = 94.11°$, $b = 1.23°$) is seen fortuitously projected atop the northern limb of the SNR's continuum boundary (as shown by the contours of continuum emission in Figs. 3.1 & 3.2. We find a 21 cm integrated flux density of $S_{1420\ MHz}$=1.02±0.06 Jy. Its peak continuum brightness temperature ($T_{continuum}$=135 K) is higher than the mean brightness temperature of neutral hydrogen seen surrounding it and it is absorbed by the H I foreground. This source is projected on the face of the H I shell approximately 7 arcminutes south of the north edge. It can be seen to be absorbed out to large negative velocities,

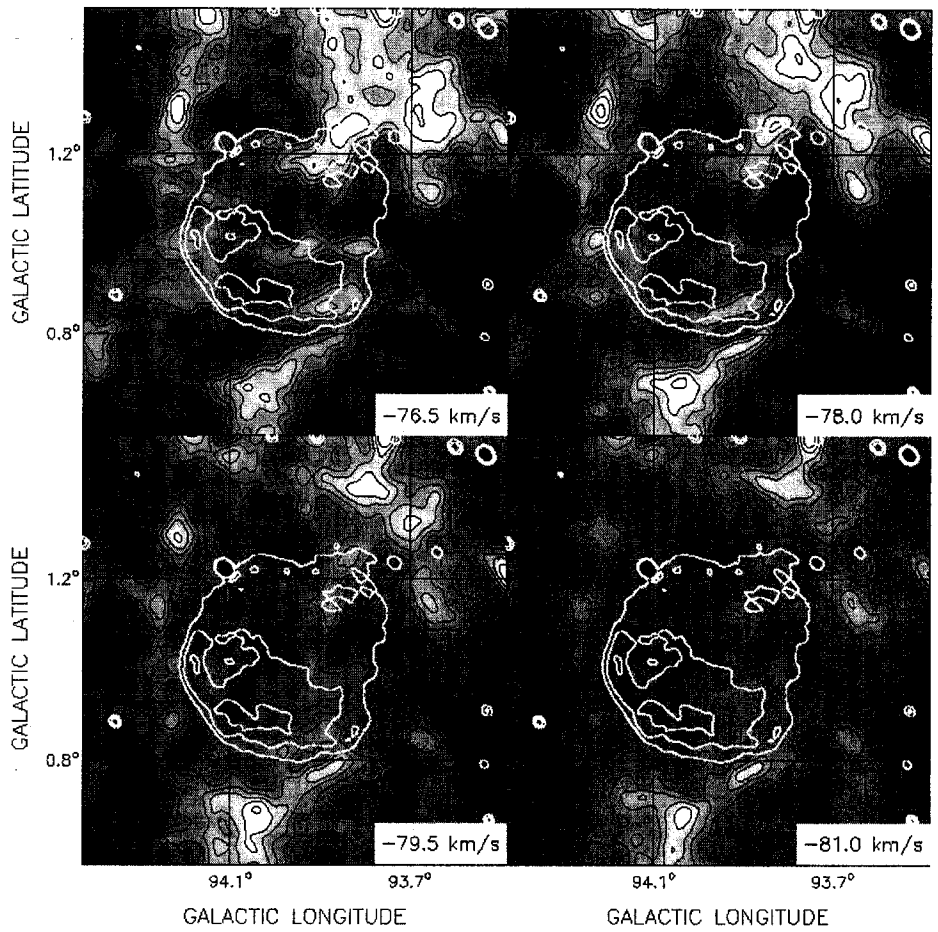

Figure 3.1: A montage of H I channel maps, spanning the LOS velocity range -76.5 km s^{-1} $\geq v \geq -81$ km s^{-1}. The velocity separation between channels is 1.5 km s^{-1}, and the image has been convolved to 2′ resolution. The eastern half of the roughly circular outline of the shell is seen in the first two channels, while the western half outline is seen better in the last two channels. H I contour levels (black lines) for the images are from -20 K to 25 K, incremented in 5 K steps. Greyscale values are from -20 Kelvin (black) to +20 Kelvin (white), with the average value for each channel subtracted first (from upper left to lower right, 52.9 K, 39.4 K, 27.6 K, and 19.3 K). The 21 cm continuum contour lines of 3C434.1 (9 K and 12 K) are shown in white.

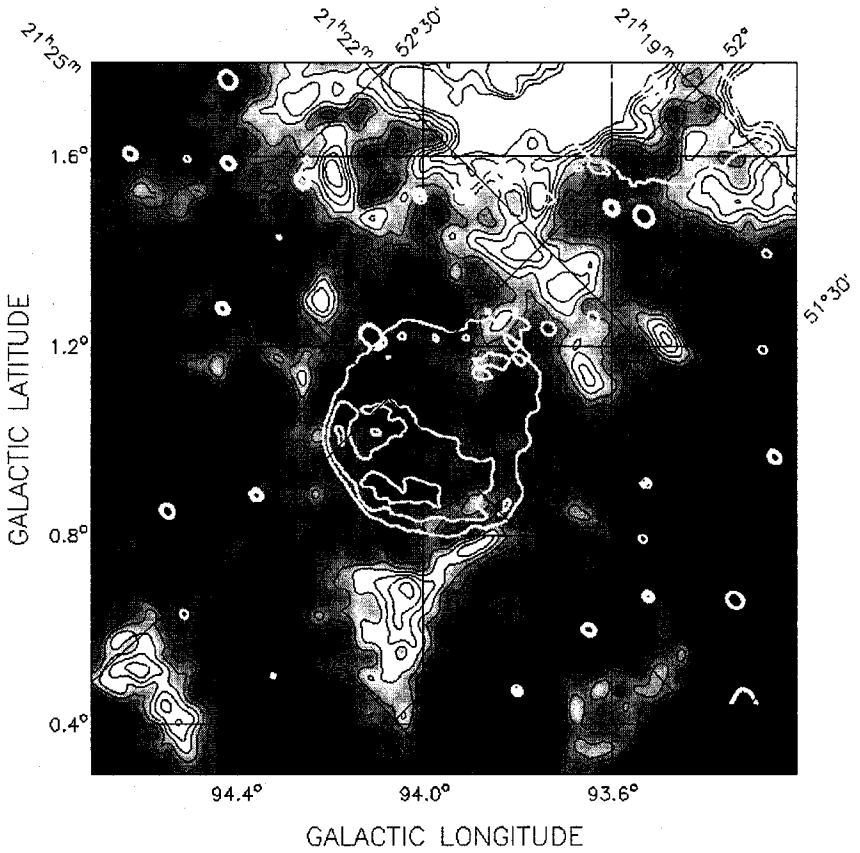

Figure 3.2: Average image of three channel maps at half resolution (2′) from −78 km s^{-1} to −81 km s^{-1}, with 21 cm continuum contours of 3C434.1 overlaid. H I line contour levels are from 24 K to 56 K in 4 K increments, and the greyscale is from 20 Kelvin (black) to 40 Kelvin (white). Both Galactic and equatorial (J2000) coordinates are shown.

suggesting it is extragalactic. For example, the 21 cm H I brightness temperature at the location of 4C51.45 decreases rapidly, showing that H I absorption is increasing, in the range of velocities shown in Fig. 3.1. Its unique location allows us to probe the structure of the SWB associated with 3C434.1.

The optical depth of H I in the line of sight (LOS) towards the north edge of 3C434.1 is calculated as follows:

$$\tau(v) = -ln\left(\frac{\Delta T_{line}(v)}{T_{continuum}} + 1\right) \tag{3.1}$$

where $\Delta T_{line} = T_{on-source} - T_{off-source}$ and $T_{continuum}$ is the continuum brightness temperature of the un-absorbed source (4C51.45). The H I brightness temperature value $T_{off-source}$ was calculated in each velocity channel from the mean emission in a 6 arcminute wide annulus (of inner radius 3 arcminutes) centred on 4C51.45, while $T_{on-source}$ was measured as the peak brightness temperature at the position of source 4C51.45.

H I emission and absorption ($\Delta T_{line}(v)$) brightness temperature profiles are shown in Figure 3.3, where values of the optical depth (τ) are shown on the right. The extended peak in emission between -35 and -75 km s^{-1} is caused by the Perseus Arm.

We believe the small absorption peaks at -70 km s^{-1} and -96 km s^{-1} are unrelated to large-scale features of Galactic structure, and most likely indicate where the LOS towards 4C51.45 encounters compressed H I in the back and front edges (respectively) of the aforementioned shell (see Sec. 4.2 below). The absorption peak near -81 km s^{-1} is likely a cold H I cloud which does not show in emission and is unassociated with 3C434.1, but is otherwise in the LOS towards 4C51.45.

In Fig. 3.4, a dark area is visible through several channels (centred on velocity -71 km s^{-1}), and is superimposed onto the brighter hemisphere of 21 cm synchrotron emission from 3C434.1. The figure shows that the radius of the dark area enlarges slightly in the first two velocity channels, and is constant thereafter with increasing velocity. This behaviour is what one would expect if the feature were the cap of an expanding bubble. This dark feature does resemble the eastern half of the continuum emission in shape. The mean 21 cm

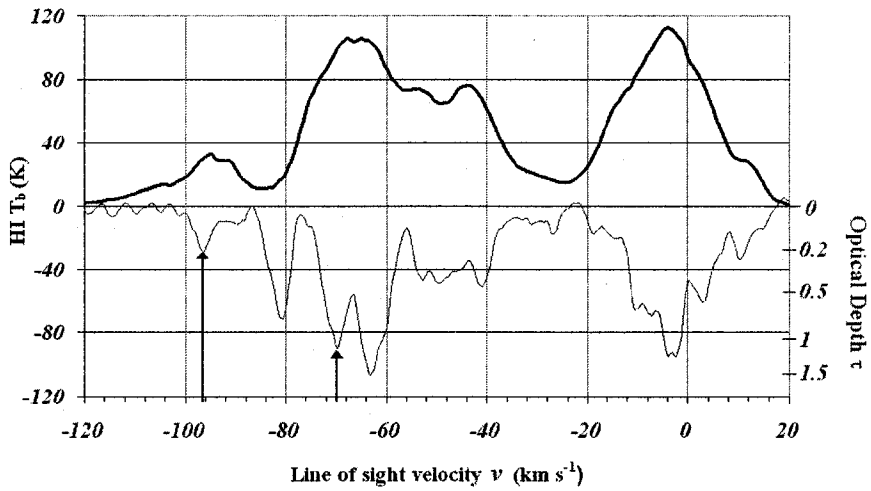

Figure 3.3: The average H I emission spectrum (thick black line) towards the SWB surrounding 3C434.1 is shown, along with the absorption profile $\Delta T = T_{on} - T_{off}$ (thin black line) towards source 4C51.45 (ℓ=94.11°, b=1.23°). The corresponding optical depth τ values are read off the right-hand vertical axis. The absorption peaks from the front (−96 km s^{-1}) and back (−70 km s^{-1}) of the H I shell edges are marked with arrows.

continuum brightness temperature of the SNR's eastern half is 12 K, not enough to be absorbed by H I in foreground channels, so the dark area cannot be the absorbed image of the SNR. However, the resemblance is striking enough to suggest that the SNR shell continuum emission is the result of an interaction with the far inside edge of the H I shell. In the following section, we show that this dark feature is most likely the end cap of the shell, and appears dark because it is absorbing line emission from a warm H I background behind it.

3.3.2 Self-Absorption of Background H I Emission by the Shell

Many small-angular-scale concentrations of cold material in the Perseus Arm are known to have optical depths of 1-2, and absorption of H I emission by cold H I is seen throughout the Perseus Arm. Such H I Self Absorption (HISA, Gibson et al. 2000) is only seen in spectral line images when cold foreground H I has similar velocity to the warm background H I, even though the warm material must be physically displaced (behind) with respect to the cold. Another criterion is that the background H I must be much warmer (and therefore brighter) than the foreground H I.

Fig. 3.3 shows the absorption profile $\Delta T(v) = T_{on}(v) - T_{off}(v)$ towards 4C51.45. Using the optical depth of the shell's near edge (τ_{-96}=0.24±0.04), one can find the Boltzmann (spin) temperature of the shell via Eqn. 3.2:

$$T_{spin} = \frac{T_{shell}}{(1 - e^{-\tau})} \tag{3.2}$$

where T_{shell} is the brightness temperature (above background) of the shell fragments. We find T_{shell}=17.3 (±14%) K, and T_{spin}=80±16 K for the ring comprising the shell's edge seen in Fig. 3.2 (summed channel map at v=−80 km s^{-1}).

If the dark area near −71 km s^{-1} in Fig. 3.4 is to be considered a self-absorbed portion of the SWB shell, two conditions must be met: a) the optical depth of the H I in this far-side cap should be comparable to that measured in the shell's near-side (−96 km s^{-1}), and b) the brightness temperature of the background gas must be much greater than the brightness temperature of gas comprising the shell.

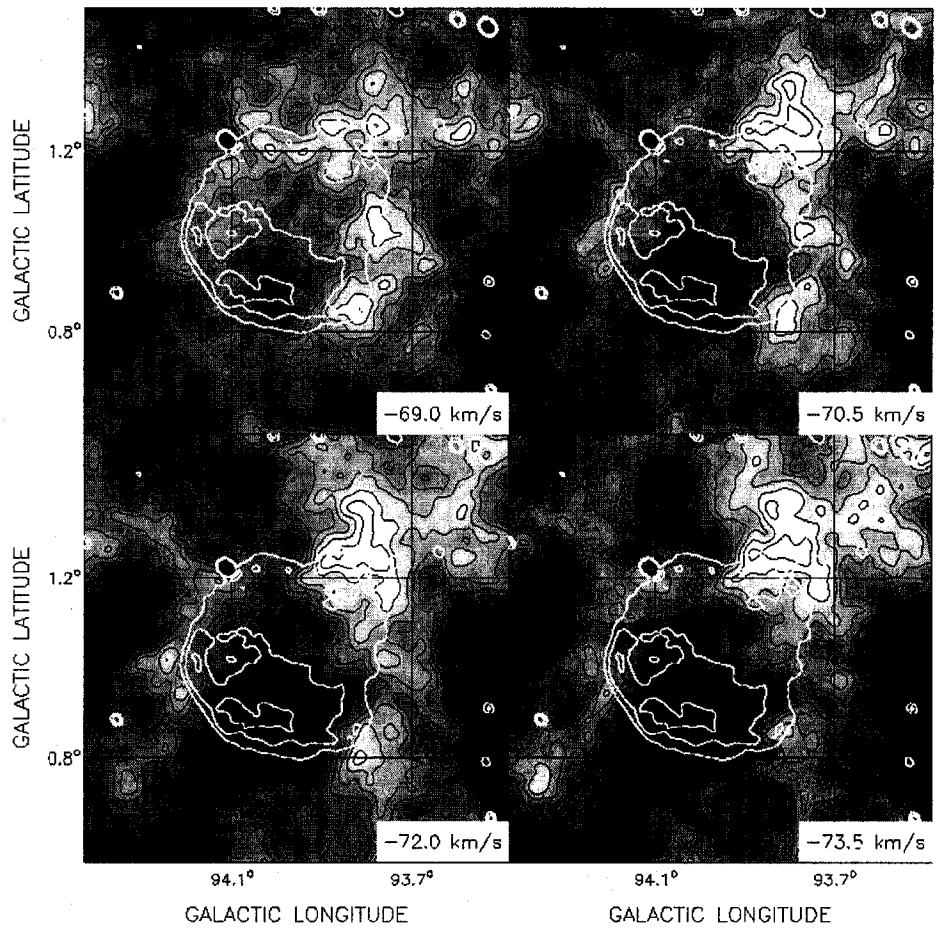

Figure 3.4: A montage of H I channel maps, spanning velocities -69.0 km s^{-1} $\geq$ v ≥ -73.5 km s^{-1}, showing the dark area (centred on $\ell = 94°$, $b = 0.9°$) described in Sec. 3.1 and 3.2. Resolution and channel separation are the same as in Fig. 3.1. The dark area appears within a generally uniform warm H I background, and is likely cold end-cap material of the shell absorbing this background emission. Contour levels and greyscale are the same as Fig. 3.1, with the following average values subtracted: 96.5 K, 92.2 K, 85.4 K, and 76.9 K.

From the brightness temperature of background emission seen at -70 km s^{-1} ($T_{off}(v = -70)$=98.8 K), and the average value of -27.2 K, from:

$$\Delta T_{darkfeature} = T_{on-darkfeature} - T_{off}(v = -70) \tag{3.3}$$

where $T_{on-darkfeature}$ is measured at several areas across the dark feature, we find:

$$\tau_{darkfeature} = -ln\left(\frac{\Delta T_{darkfeature}}{T_{off}(v = -70)} + 1\right) = 0.32 \pm 0.04 \tag{3.4}$$

The values of optical depth measured for material in the dark feature are therefore similar to those of the shell towards 4C51.45, and the first condition is met.

To determine the temperature of the background H I at $v = -70$ km s^{-1}, we separate the component of absorption due to the shell (optical depth similar to τ_{-96}) from that due to the unrelated material at $v = -70$ km s^{-1}. We subtract the absorption peaks ΔT, and find an optical depth of 0.60±0.17 for the remaining material by:

$$\tau = -ln\left(\frac{\Delta T(v = -70) - \Delta T(v = -96)}{T_{continuum}} + 1\right) \tag{3.5}$$

This assumes that at the location of 4C51.45, the shell's far-edge (-70 km s^{-1}) has similar optical depth to that in the near-edge (-96 km s^{-1}). The brightness temperature of the background (in velocity channel -70 km s^{-1}), together with this optical depth allows us to calculate the spin temperature of the background gas:

$$T_{background} = \frac{T_{off}(v = -70)}{(1 - e^{-\tau})} = 220 \pm 50 \text{ K} \tag{3.6}$$

which is much greater than the temperature of the shell. Thus, if the dark feature at -72 km s^{-1} is cold material within the SWB shell, the background emission is sufficiently warm to be absorbed by it, and the second condition is met. We henceforth will treat this dark feature as the end-cap of the far side of the SWB shell.

3.3.3 A Non-Kinematic Distance to the SWB

CTB104A and 3C434.1 are the only supernova remnants known in the Galactic plane vicinity of ℓ=94°. Until recently, their distances have been elusive, as have most supernova remnant distances. Uyaniker et al. (2002) kinematically determined the distance to CTB104A (G93.7−0.3) as 1.5±0.2 kpc, a reasonable value considering that the kinematic distance method is probably more valid for local objects than anywhere else (Foster & Routledge 2003). The large line of sight velocity of the SWB associated with 3C434.1 (~ -79 km s^{-1}) suggests it is very distant: with R_0=8.5 kpc and θ_0=220 km s^{-1}, a kinematic distance of 10 kpc follows. This value can almost certainly be dismissed as inaccurate because of the unreasonable physical parameters indicated for the supernova remnant (e.g. 80 pc diameter). On the basis of the Σ-D relationship, Mantovani et al. (1982) find a more reasonable range (3.8-6.4 kpc), though this highly disputed method overestimates the distance to CTB104A by nearly a factor of two.

The observed LOS velocity of the SWB surrounding 3C434.1 is within the velocity range occupied by the Perseus Spiral arm as seen in the H I emission spectrum (see Fig. 3.3), which crudely suggests that the system is at least as far as the centre of the Perseus arm, likely lying on the Arm's far edge. The large line of sight velocity of the system likely includes contributions from non-circular motions (e.g. the Spiral Shock, Roberts 1972), and does not accurately reflect the system's circular velocity from Galactic rotation, causing a severe overestimate of the kinematic distance.

To find a non-kinematic distance to our SNR/SWB system, we apply the new method of Foster & Routledge (2003; hereafter F&R) in the direction ℓ=94°, b=1°. The method of F&R begins with a model of the integrated H I column density versus distance $N_{HI}(r)$. After transforming to velocity space (using a velocity-to-distance mapping function $v(r)$ with variable parameters), the model is fitted to the observed cumulative $N_{HI}(v)$ with a χ^2 minimization method. Parameters of both the model $N_{HI}(r)$ and the mapping function $v(r)$ are allowed to vary until an acceptable fit is achieved. The results of this approach are both the model $N_{HI}(r)$ and the function $v(r)$ that together best reproduce the observed distribution $N_{HI}(v)$. The distance to an individual object for which a radial velocity is

known is then calculated with either result.

This new technique principally assumes that on a large scale, the observed line of sight velocity (for atomic hydrogen emission) is increasingly negative with distance. For H I in emission and in circular rotation, the assumption that distance is monotonic with velocity is fundamentally true. However, the HISA associated with the shell's end-cap shows that the warm emission throughout the field at -70 km s^{-1} is *physically behind* the shell. Thus, when calculating the column density N_{HI} to the SNR/SWB, integrating emission in all channels to the systemic velocity ~ -80 km s^{-1} may overestimate the true foreground column. Conversely, integrating only to an upper limit of v=-70 km s^{-1} (where the shell begins to appear in velocity space; see Fig. 3.6) may miss some foreground material appearing at greater negative velocities. We choose our upper limit as an intermediate velocity ~ -75 km s^{-1}, and believe this reasonably estimates the true foreground column density.

We thus integrate H I emission (shown in Fig. 3.3) alone to this velocity, and find the foreground H I column density to 3C434.1 to be N_{HI}=(1.04±0.10) $\times 10^{22}$ cm^{-2}. To the Galactic edge, we find $N_{HI}(r = \infty)$=(1.18±0.11) $\times 10^{22}$ cm^{-2}. The distance to the SNR/SWB that corresponds with N_{HI} is 5.2±1.1 kpc. Fig. 3.5 shows this distance predicted by the method's output of cumulative column density as functions of distance and velocity for this direction. Most of the distance uncertainty derives from uncertainties in N_{HI} and $N_{HI}(r = \infty)$.

3.4 Kinematic Model of the Expanding SWB

In the (ℓ, b) image in Fig. 3.6, a ring of H I emission is visible surrounding the SNR. This image shows the H I emission summed over four channels centred on -78.5 km s^{-1}. The H I ring has the appearance of a fragmented shell, possibly an expanding SWB surrounding the SNR. We searched for the corresponding elliptical "cross sections" of such an expanding shell in longitude-velocity and latitude-velocity images, and the results are shown in the (ℓ, v) and (b, v) plots in Fig. 3.6, respectively.

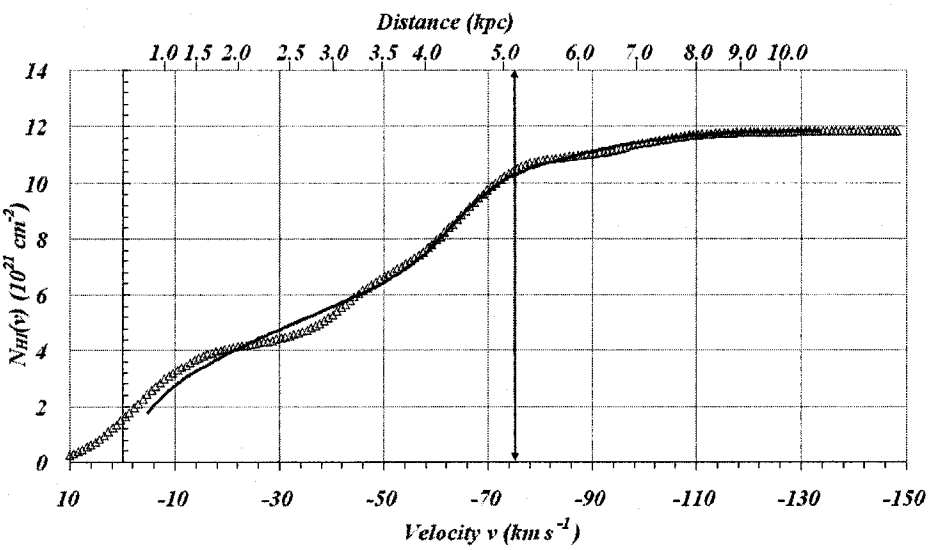

Figure 3.5: The observed cumulative column density-velocity relation $N_{HI}(v)$ (open triangles) towards ℓ=94°, b=1°. The fitted model $N_{HI}(v)$ is also shown (solid line). The distance-velocity relation $v(r)$ that results from the fit is used to determine the corresponding heliocentric distance (plotted on the top horizontal axis). The integration limit velocity (−75 km s^{-1}) to which we believe all H I emission between the SWB/SNR and the Sun is foreground is shown with an arrow. The SWB/SNR distance predicted by the fitted model $N_{HI}(v(r))$ is r=5.2±1.1 kpc.

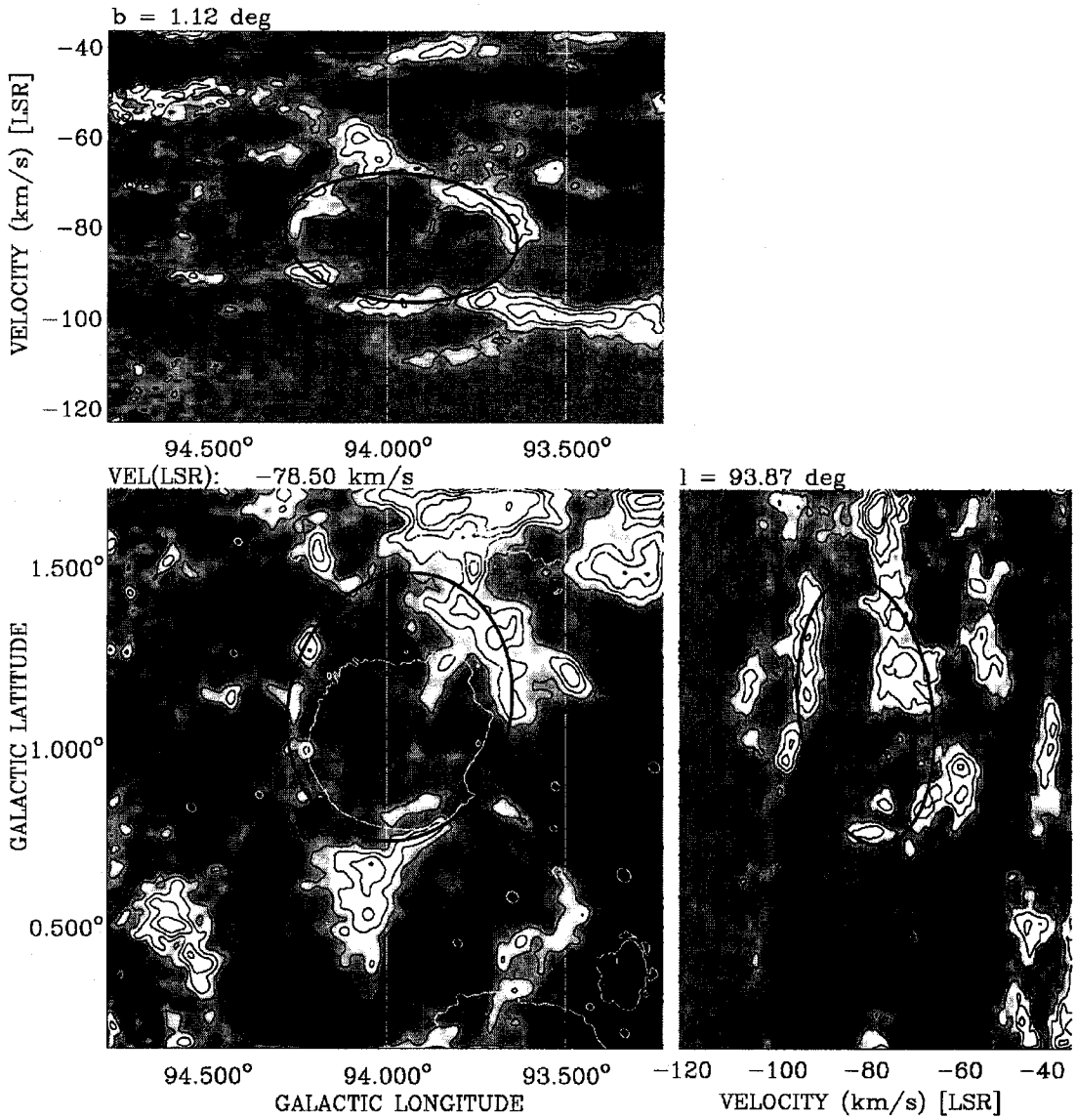

Figure 3.6: Three views of the elliptical shell model (thick black ellipses) fitted to the observed HI emission patterns of the shell, in (ℓ, b), (ℓ, v), and (b, v) HI images. The continuum outline of the supernova remnant is shown (white contour).

3.4.1 The Expanding SWB Observed in HI Emission

The (ℓ, b), (ℓ, v), and (b, v) H I emission patterns seen in Fig. 3.6 are crudely compatible with a spherical H I shell of radius $\simeq 21'$ centred on $(\ell, b)\simeq(93.97°, 1.10°)$, having a systemic velocity $v_{sys} \simeq -80$ km s^{-1}, and a radial expansion velocity given by half its extent in velocity, i.e. $v_e \simeq 13$ km s^{-1}. However, the (ℓ, b) outline of the H I shell is actually elliptical, and the (ℓ, v) and (b, v) outlines are also slightly skewed. This suggests that rather than being spherical, the expanding H I shell may in fact be *ellipsoidal*, and that the ellipsoid is inclined with respect to our line of sight.

A simple kinematic model for an expanding ellipsoid was constructed for the H I shell. The objective of creating the model was to reproduce the appearance of the (ℓ, b), (ℓ, v), and (b, v) "sections" through the ellipsoidal shell which are recognizable in Fig. 3.6. To minimize the number of free parameters, the ellipsoid was allowed only two parameters of size: a semimajor axis a_1 and a semiminor axis a_2. The ellipsoid is assumed to have a circular cross-section; the nomenclature implies that it is prolate, though it could equally well be oblate. The major axis can be rotated in yaw (ϕ) and pitch (ψ) as shown in Fig. 3.7. The observer is located on the z-axis; hence Galactic coordinates ℓ and b correspond to $-x$ and y, respectively. As shown, positive ϕ yaws the ellipsoid's major axis counterclockwise as seen from above, while positive ψ pitches the end of its major axis upwards which is closest to the observer.

In the kinematic model, a shell of one voxel thickness is created which occupies all voxels satisfying

$$\frac{x'^2}{a_2^2} + \frac{y'^2}{a_2^2} + \frac{z'^2}{a_1^2} = 1 \tag{3.7}$$

The ellipsoid is oriented relative to the observer through the relations:

$$x = x'cos\phi + 0 + z'sin\phi = b_{11}x' + b_{12}y' + b_{13}z' \tag{3.8}$$

$$y = x'sin\phi sin\psi + y'cos\psi - z'cos\phi sin\psi = b_{21}x' + b_{22}y' + b_{23}z' \tag{3.9}$$

$$z = -x'sin\phi cos\psi + y'sin\psi + z'cos\phi cos\psi = b_{31}x' + b_{32}y' + b_{33}z' \tag{3.10}$$

For simplicity, each voxel of the shell is assigned an expansion velocity directed

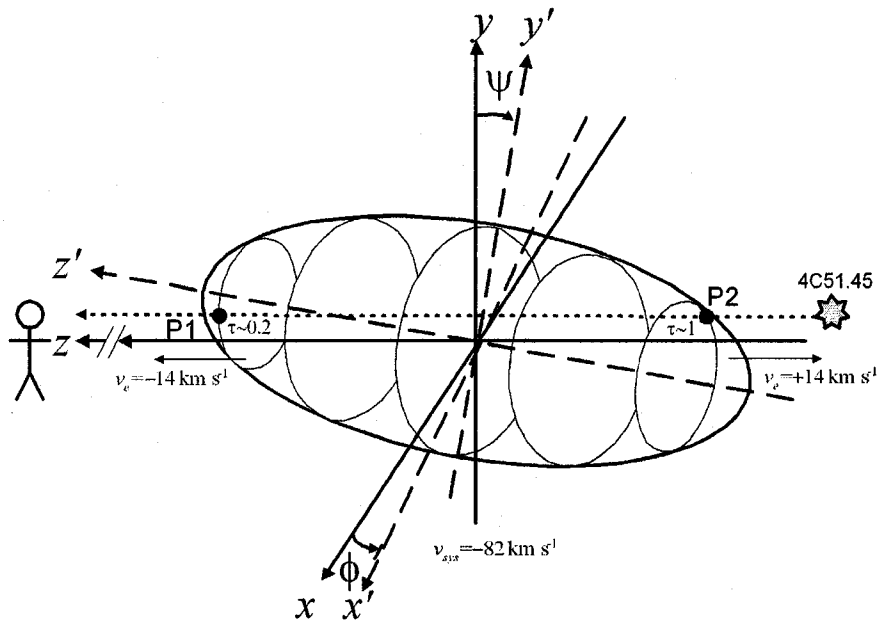

Figure 3.7: Sketch of the model H I shell's orientation and geometry, showing the viewing angles ϕ and ψ (defined in Sec. 3.4.1) and points of intersection (P1, P2) between the shell and the LOS towards background continuum source 4C51.45 (shown by the star symbol). The ellipticity of the model is exaggerated.

radially outward from the origin of the ellipsoid, with the magnitude of the expansion velocity assumed to be proportional to the radial displacement of the voxel from the origin of the ellipsoid. Such a proportionality is a property of any power-law expansion. That is, the ellipsoidal shell is imagined to be expanding homologously so that its shape stays constant as it expands. The line-of-sight velocity of any voxel in such a shell is simply the radial expansion velocity of that voxel, projected onto the z-axis, if the shell as a whole has zero systemic velocity. We define v_{sys} as the systemic line-of-sight velocity of the origin of the ellipsoid. The z-axis points toward the observer, as shown in Figure 3.7, but astronomical convention is that positive velocities are directed *away* from the observer; hence the line-of-sight velocities must be negated to conform to convention.

To create a (b, v) plot, all voxels can be found in which a plane at $x = 0$ intersects the tilted ellipsoid, with the z-coordinate of each such voxel (the component of its radius vector projected onto the z-axis) being proportional to the LOS expansion velocity of that voxel, relative to v_{sys}. For a power-law expansion $R_b(t) = R_{initial}t^n$, for example, the proportionality relation between radial position of a voxel related to the bubble and its radial expansion velocity is $R_b(t) = t/n \times dR_b/dt = t/n \times v_e(t)$ for any expansion age t.

Similarly, to create an (ℓ, v) plot, a plane at y=0 intersects the tilted ellipsoid. To permit the (b, v) and (ℓ, v) "sections" through the ellipsoid to be taken at ℓ and b positions which do not coincide with the origin, however, fixed offsets in x and y respectively are permitted. Thus in the (b, v) plot in Fig. 3.6, ℓ=93.87°, and in the (ℓ, v) plot b=1.12°, whereas the origin of the ellipsoid is taken as (ℓ_0, b_0)=(93.961°, 1.123°).

In a similar manner, in constructing an (ℓ, b) plot a plane at z=0 can intersect the tilted ellipsoid. To allow the line-of-sight velocity chosen for the (ℓ, b) plot to differ from v_{sys} of the ellipsoid, a fixed offset in z is permitted, corresponding to sliding this plane, which is orthogonal to the line of sight, toward or away from the observer along the z-axis. Thus in Fig. 3.6, the (ℓ, b) "section" is at $v = -78.5$ km s^{-1}, whereas v_{sys} for this modelling process is set to -82 km s^{-1}, corresponding to an offset in z of 7 pc away from the observer using the relation $R_b = tv/n$ above. The parameters chosen for the model ellipsoid

whose "sections" are drawn in Fig. 3.6 are a_1=36 pc, a_2=29 pc, ϕ=35°, ψ=70°, and v_{sys}=−82 km s^{-1}. The distance is assumed to be 5.2 kpc, the origin is taken as (ℓ_0, b_0)=(93.961°, 1.123°), the exponent n in $R_b(t) = R_{initial}t^n$ is assumed to be 3/5, and the age t of the expansion is $\sim$ 1.2 Myr. While likely not unique, this set of parameters reproduces the H I *emission* appearance of the shell reasonably well in (ℓ, b), (ℓ, v), and (b, v), as shown in Fig. 3.6.

We are very fortunate in the case of the SWB surrounding 3C434.1, to find a strong extragalactic continuum source, 4C51.45, on the same line of sight. The line-of-sight velocities at which H I *absorption* of this source is produced by the shell of the SWB can now be used to check the parameters for the expanding ellipsoid found above using only H I in emission.

3.4.2 The Expanding SWB Observed in HI Absorption

The expanding ellipsoidal shell model introduced in Section 3.4.1 above is useful for interpreting H I absorption spectra as well as for producing (ℓ, b), (ℓ, v), and (b, v) "sections" of an H I shell seen in emission. For an absorption spectrum, given the position $(\ell_{source}, b_{source})$ of a background continuum source relative to the origin (ℓ_0, b_0) of the ellipsoidal shell, the points P1, P2 in Fig. 3.7 can be found at which the line of sight to the source intersects the ellipsoidal shell. Then the corresponding line-of-sight velocities follow from the z-coordinates of P1, P2 under the assumption that the expansion velocity of any voxel in the shell is proportional to its distance from the origin, as stated earlier. Using x=−$(\ell_{source} - \ell_0)$ and y=$(b_{source} - b_0)$ we find:

$$z_{1,2} = b_{31}x' + b_{32}y' + b_{33}z' \tag{3.11}$$

where

$$x' = \frac{1}{2a}\left(-b \pm \sqrt{b^2 - 4ac}\right) \tag{3.12}$$

$$y' = \left(\frac{b_{11}b_{23}}{b_{13}b_{22}} - \frac{b_{21}}{b_{22}}\right)x' + \left(\frac{y}{b_{22}} - \frac{b_{23}x}{b_{13}b_{22}}\right) \tag{3.13}$$

$$z' = \frac{x - b_{11}x'}{b_{13}} \tag{3.14}$$

and

$$a = \frac{b_{11}^2 a_2^2}{b_{13}^2 a_1^2} + 1 + \left(\frac{b_{11}b_{23}}{b_{22}b_{13}} - \frac{b_{21}}{b_{22}}\right)^2 \tag{3.15}$$

$$b = 2\left(\frac{b_{11}b_{23}}{b_{13}b_{22}} - \frac{b_{21}}{b_{22}}\right)\left(\frac{y}{b_{22}} - \frac{b_{23}x}{b_{13}b_{22}}\right) - \frac{2a_2^2 b_{11}x}{a_1^2 b_{13}^2} \tag{3.16}$$

$$c = \left(\frac{y}{b_{22}} - \frac{b_{23}x}{b_{13}b_{22}}\right)^2 - a_2^2 + \frac{a_2^2 x^2}{a_1^2 b_{13}^2} \tag{3.17}$$

with all quantities in the same units (e.g. pixels). Then the line-of-sight velocity of the voxel at P1 or P2 equals the radial expansion velocity of that voxel, projected onto the z-axis, negated to conform to convention, and added to v_{sys} of the ellipsoid:

$$v_{1,2} = v_{sys} - \frac{nz_{1,2}}{t} \tag{3.18}$$

in which we draw on the relation $R_b = tv/n$ as before.

Since 4C41.45 is located at $(\ell_{source}, b_{source})$=(94.11°, 1.22°) whereas the origin of the ellipsoid is set to be (ℓ_0, b_0)=(93.961°, 1.123°), we enter $x = 8.9'$ (25 pixels) and $y = 5.8'$ (16 pixels) in the foregoing. Using the parameters for the SWB deduced in Section 3.4.1 from the (ℓ, b), (ℓ, v), and (b, v) H I *emission* patterns, the expressions above predict that H I absorption occurring in the ellipsoidal shell should appear at line-of-sight velocities of −93.8 km s^{-1} and −70.1 km s^{-1}.

Fig. 3.3 shows the observed H I absorption profile towards 4C51.45, and in it we see a weak absorption peak near −96 km s^{-1} and another peak near −70 km s^{-1}. Thus the absorption features seen in the 4C51.45 H I *absorption* profile do substantiate the values found for the SWB parameters in the previous H I *emission* analysis. An important physical result from this kinematic analysis is the expansion velocity along the degenerate minor axes of the ellipsoid: na_2/t ~14 km s^{-1}.

3.4.3 Physical Characteristics and Dynamical Considerations

The differential column density of the shell wall measured at the position of 4C51.45, and adjusted for path length is:

$$\Delta N_{HI} = 1.823 \times 10^{18} \frac{T_{shell}}{1 - e^{-\tau}} \tau \Delta v \times sin\theta cos\phi \tag{3.19}$$

where T_{shell} is the brightness temperature (above background) of the shell (from Sec. 3.3.2, 17.3 K), and θ (50°) and ϕ (9.6°) are the angular locations (in spherical polar coordinates) of the 4C51.45 absorption feature on the surface of the shell, assumed a sphere for this estimate. Integrating across the velocity width of the τ-line centred on -96 km s^{-1} (see Fig. 3.3), we find $\Delta N_{HI} \simeq 1.2 \times 10^{20}$ cm^{-2}. This is taken as representative of the typical column density through the shell normal to its surface. Assuming a uniform thickness of 2′ and the elliptical shape for the shell modelled in the previous section, the mean density of swept-up neutral hydrogen within the shell is $n_{HI} \sim 13$ cm^{-3}. We thus infer that the environment into which the bubble expanded had an original ambient density of $n_0 \sim 5$ cm^{-3}, a typical value for the interstellar medium within a spiral arm undisturbed by massive stars. The mass of material swept up in the shell is 14500 $M_\odot$, (accounting for 9% Helium abundance by number in the surroundings), and the kinetic energy of the shell $E_k = 2.8 \times 10^{49}$ ergs. Table 3.1 lists these and other physical characteristics of the shell. The observed size and expansion rate of our H I bubble suggests it has certainly evolved beyond the first stage of bubble evolution (free expansion), and is likely well into the second, longest-lasting phase of evolution (the energy-driven phase) where the formation of a thin cold outer shell is expected due to minor radiative losses at the shell periphery.

The following equation governs the evolution of a typical energy-conserving interstellar bubble (eqn. 51, Weaver et al. 1977) with no losses:

$$R_b(t) = 27 n_0^{-\frac{1}{5}} L_{36}^{\frac{1}{5}} t_6^{\frac{3}{5}} (\mathrm{pc}) \tag{3.20}$$

where n_0 is the ambient interstellar density, L_{36} is the power of the stellar wind (L_w) responsible for the shell's formation (in units of 10^{36} ergs s^{-1}), and t_6 is the time (10^6 yr). Accounting for radiative loss produces an analytically intractable

Parameter	Value
Geometric Centre (ℓ_0, b_0)	93.961°, 1.123°.
Systemic velocity v_{sys}	-79 km s^{-1}
Distance	5.2±1.1 kpc
Size (semimajor, semiminor axes)	36±7 pc, 29±6 pc
Mean Thickness of Shell	3.1±0.6 pc
Expansion Velocity v_e	14 ± 3 km s^{-1}
H I density within shell n	12.9 ± 2 cm^{-3}
Local ISM H I density n_0	4.6 ± 1 cm^{-3}
H I mass within shell M_{shell}	14500 ± 2500 $M_\odot$
Kinetic energy of shell E_k	$2.8 \pm 0.5 \times 10^{49}$ ergs

Table 3.1: Observed and calculated physical and dynamical characteristics of the ellipsoidal stellar wind bubble surrounding 3C434.1.

equation. Weaver et al. (1977) numerically simulate the evolution of a bubble accounting for radiative loss, and find that $R_b(t)$ evolves as a power law with exponent 0.58, intermediate between Eqn. 3.20 and the law $R_b(t) \propto \sqrt{t}$ of Steigman et al. (1975). Koo & McKee (1992) find a similar solution for a partially radiative bubble, for which the shell radius will expand with a power law of index 0.57. One can see that partial radiative losses affect the time evolution of a bubble in only a small way. Therefore, in estimating parameters for our SWB, we retain the use of Weaver et al.'s analytic evolutionary equation (Eqn. 3.20) for the analysis. The dynamical age of the bubble is calculable by combining $R_b(t)$ with its first derivative: $t \approx 0.6 R_b/v_e$. With R_b=34 pc and v_e=14 km s^{-1} we find $t \sim 1.4 \times 10^6$ yr.

We assume the SWB was created by the progenitor and other O and B stars of the same cluster, and therefore the age of the SWB must be at least equal to the main-sequence lifetime of the progenitor star (assuming the age of the SNR itself is negligible). Since there is no massive star with such a short lifetime (1.4 Myr), an apparent conflict exists between the dynamical age of the bubble and the age of the SNR progenitor. Conflicts between kinematic and evolutionary ages of stellar wind bubbles have been observed by numerous authors (e.g. Cazzolato & Pineault 2003, Cappa et al. 2002) and the puzzle is highlighted in the review of Garmany (1994), who states the discrepancy is often by a factor

of 2. This is similar to the uncertainty that lies within the non-radiative stellar wind bubble solutions of Weaver et al. (1977). Explanations such as noncoeval star formation have been proposed (Saken et al. 1992), but cannot be proven here. We must believe that the true age of our system is likely much greater than 1.4 Myr, possibly up to 2.8 Myr. A plausible age nearer to this upper limit is supported by the discovery of an O4V type star within our bubble (see Sec. 3.5). The main-sequence lifetime given by Chiosi et al. (1978):

$$t_* = 4.4 \times 10^6 (S_{49})^{-\frac{1}{4}} (\mathrm{yr}) \tag{3.21}$$

is 2.6 Myr, where S_{49}=8.5 is the rate at which an O4V star emits ionizing photons (S), in units of 10^{49} s^{-1} (Panagia 1973). This lifetime is for an intermediate mass O4V star, or about 70 $M_\odot$ in Schaerer & de Koter (1997), who show evolutionary models for O4V stars from 60 $M_\odot$ (3.4 Myr) to 85 $M_\odot$ (1.7 Myr).

Simultaneously in solving for the SWB age t, we solve for the wind luminosity of the enclosed star(s). At the minimum age of the system (1.4 Myr), L_w ~5.1×10^{36} erg s^{-1}, and at the maximum (2.6 Myr), L_w ~8.4×10^{35} erg s^{-1}. Assuming a constant wind luminosity over the bubble's minimum lifetime, the energy imparted to the SWB's expansion is ϵ=E$_k$/E$_w$=0.12 times the total energy output (E$_w$=2.3×10^{50} erg). This efficiency is 0.07 if the bubble is considered as old as the 2.6 Myr main sequence lifetime of the O star we find within it.

3.4.4 Energy Considerations

The wind luminosity of a star powering the SWB is related to the terminal wind velocity v_w and mass-loss rate ($\dot{M}_6 = \dot{M}/10^{-6}\ M_\odot$ yr^{-1}) as $\dot{M}_6 v_{2000}^2 \approx 1.26 \times L_{36}$ (where we define v_{2000}=v_w/2000 km s^{-1}). From the above wind luminosity one calculates $\dot{M}_6 v_{2000}^2$ ≃6.4. Following McKee et al. (1984), the *characteristic* wind luminosity for a bubble formed in a medium with density n_0 is:

$$L_{st} = 1.26 \times 10^{36} \left(S_{49}^2/n_0\right)^{1/3} (\mathrm{ergs\ s^{-1}}) \tag{3.22}$$

Main sequence stars from O4-O8 typically produce S_{49}=$L_{36}^{2/3}$ (±20%) photons per second (Abbott 1982; Panagia 1973), and if the star(s) that formed our SWB

are similar, then $S_{49} = 3$. McKee et al. (1984) also define the dimensionless wind luminosity L_w^*=L_w / L_{st} as a gauge of the relative strength of the outflow. The minimum age of the bubble (1.4 Myr) gives L_w^*=3.26, while at the bubble's plausible age of 2.6 Myr, we find L_w^*=0.5 indicating a weak outflow, and that the wind-blown cold H I shell is likely filled with the hot wind of the resident stars. Thus cool shell material is evaporating and mixing with the internal hot wind, reducing the pressure caused by the wind and slowing the shell's expansion. It is probable that the H I shell's expansion has slowed due in part to such cooling, and its exterior is beginning to fragment, consistent with its current appearance.

Using the equations of McKee et al. (1984) we have calculated a simple time history model of a SWB blown by a single star, into a medium with n_0=5 cm^{-3}. A single O5.5V star is used, as the wind luminosity of such a star (L_{36}=3.5) is the closest match to the wind luminosity of the bubble found in Sec. 3.4.3 at its minimum age (L_{36}=5.1). In our model, the O5.5V star's *entire* mechanical energy output contributes to the formation of the bubble, whereas in reality the energy conversion efficiency is 20% or less (Koo & McKee 1992). The characteristic wind luminosity of the system at time t=0 is L_w^*=2.73, closely matching the value calculated for our bubble at its minimum age (L_w^*=3.26). The radius, velocity and age are found at which the bubble stalls, and are where pressure between the bubble's interior is balanced by the confinement pressure of the photoionized hydrogen surrounding the bubble. The bubble also becomes radiative at this point. Table 3.2 shows that the model bubble stalls when it reaches t=2.6 Myr, at a radius of 50 ($\pm$10) pc, within the uncertainty of our elliptical model's mean radius (34$\pm$7 pc). The stall velocity of 11.4 km s^{-1} is very nearly that calculated for the ellipsoidal model (14 km s^{-1} in Sec. 3.4.2). Considering the fragmented appearance we observe our SWB to have, the above simple model suggests that it is certainly highly evolved, and has certainly reached the last stages of Phase II. The rate of expansion due to momentum conservation has slowed to nearly the sound speed of the unperturbed medium, and the SWB's dissipation in the ISM has begun. For a "standard" bubble (n_0=1 cm^{-3}, L_{36}=1.3; Weaver et al. 1977) the dissipation time is approximately given by the main-sequence lifetime of the star, in this case 2.6$\times$10^6 yr. We are thus likely viewing the last period of this bubble's identity within the ISM, a fact confirmed by its

patchy appearance.

Parameter	Model	Observed
$L_w(10^{36}$ergs s$^{-1})$	3.5	5.1
L_w^*	2.73 (at t=0)	3.26 (at t=1.4 Myr)
$S_{49}(10^{49}$ photons s$^{-1})$	2.3	3.0
Stall Radius R_b (pc)	50±10	34±7
v_e at stall (km s^{-1})	11.4 ±2.3	14
t_{stall} (10^6 yr)	2.6±0.5	1.4-2.6

Table 3.2: Comparison of observed SWB parameters to those calculated from a simple time-evolution model of a SWB formed by the wind of a single O5.5V star, chosen to match the observed wind luminosity L_w at the minimum age of the bubble (t=1.4 Myr). The model is from McKee et al. (1984). The stall velocity and age for the bubble are near the lower and upper limits of those same parameters as measured, respectively. The stall radius is 30% larger than the observed radius, but is within uncertainties. The SWB surrounding 3C434.1 is apparently in its early stages of dissipation.

3.5 Stellar Residents within the SWB

We have carried out a search towards the direction of the SWB for O and B-type stars that could be associated with the SWB, and we here present the results of this search.

An observational bias of overweighting luminous objects will afflict a magnitude-limited sample of stars, especially out to great distances. This Malmquist bias will affect our observations, which therefore will reveal only the most massive and brightest stars at the distance of the SNR/SWB (5.2 kpc). This bias is pushed further towards luminous stars by the large total extinction A_V suffered by radiation (see below). On the other hand, the patchiness of interstellar extinction (the effects of which have been found on scales down to 30 square arcminutes by Boyle et al. 1992) makes it likely that many stars within our 730 square arcminute fields will be observed through transparent "windows" in the dust column (or conversely through dust screens). These effects, coupled with uncertainties in absolute magnitude M_V calibration (at least ±0.3 mag, or 15%

distance uncertainty) mean that a wide range of stars could be considered as possible candidates for association with the SWB. We quantify the selection criteria as follows.

First, we estimate the mean extinction to the SWB by measuring the hydrogen column density in the foreground. We express this column in visual magnitudes using the gas to dust ratio of Predehl et al. (1995), N_H/A_V=1.79±0.03×10^{21} cm^{-2} mag^{-1}. From H I in emission, the column density from Sec. 3.3.3 amounts to 6 magnitudes of extinction. This is likely a lower limit as H I within the entire column may not all be optically thin, a fact illustrated by the higher extinction found using the absorption profile towards 4C51.45, which shows an H I column amounting to at least 7 magnitudes of foreground extinction. This optically thick H I may not be uniformly distributed over the observed field and distance column, so a mean extinction of 6.5 magnitudes to the SNR/SWB is adopted, equivalent to a reddening of $E(B-V)$ ~2.1 magnitudes. We conservatively estimate the variation in $E(B-V)$ across field 1 by calculating the standard deviation $\sigma_{E(B-V)}$ of reddenings for all stars in distance bins 250 pc wide, out to 2.5 kpc. A total reddening scatter of $\sigma_{E(B-V)}$≈0.42 mag is calculated in this manner. Since our photometric error is small (see Sec. 3.2.2), this scatter is likely due to the irregular distribution of local dust across the field.

Thus stars for which $E(B-V)$ falls within 2.1±0.4 mag, and distance d within 5.2±1.0 kpc are considered candidates. For the given extinction (A_V=6.5±1.2 mag) and distance, the expected minimum stellar type that could be detected in our magnitude-limited sample (m_V=16.6 mag) is B1V (M_V=−3.2 mag). At the edge of the uncertainties, we may find stars down to B2.5V (M_V=−2.0 mag).

Of the 100 or so classified O and B stars seen towards the interior of the SWB, only 12 have reddenings $E(B-V)$ ≈1.7 mag or greater. If we assume all are main sequence stars, then eleven remain for which d ≤5.2±1.1 kpc. Table 3.3 lists the characteristics of these stars, and shows their photometric distances (assuming a common luminosity class of V). Three B0V stars have distances and reddenings that are very consistent with the SWB: Stars 1, 4, and 10 are the most likely residents. The O4-type Star 7 also has a very consistent distance and reddening. Much less certain and barely within the distance uncertainties is Star 2 and other stars fall short of being solid candidates. We can comfortably

Star	$B-V$ (±13%)	$U-B$ (±20%)	m_V (±0.07)	MK Type	M_V (±0.3)	d (kpc) (±30%)	$E(B-V)$ (±0.23)
1	1.45	0.06	14.95	B0	−4	5.1	1.74
2	1.75	0.11	13.55	O5	−5.7	3.7	2.08
3	1.72	0.44	13.92	B2	−2.47	1.2	1.95
4	1.46	0.02	15.05	B0	−4	5.2	1.77
5	1.62	0.40	14.10	B2	−2.47	1.0	1.84
6	1.66	0.21	14.04	B0	−3.9	2.4	1.95
7	1.86	−0.01	14.33	O4	−6.0	4.9	2.22
8	1.61	0.22	14.33	B1	−3.7	2.7	1.89
9	1.56	0.31	13.78	B2	−2.47	1.4	1.80
10	1.36	0.00	14.57	B0	−4	4.8	1.66
11	1.40	0.14	14.70	B1	−3.2	3.5	1.66

Table 3.3: Eleven stars towards 3C434.1 with observed reddenings that are consistent with that observed toward the SNR/SWB ($E(B-V)$=2.1 mag), i.e. 1.7 mag$\leq E(B-V) \leq$2.5 mag. The uncertainty in the assigned spectral type is on average plus or minus one sub-type (e.g. an O5 is O4-O6 within uncertainty). Distances are calculated using reddening law R_V=$A_V/E(B-V)$=3.1. All distances have an uncertainty of ±30%.

conclude that only Stars 1, 4, 7 and 10 are candidates for association with the SWB surrounding 3C434.1. Figure 3.8 shows the positions of these stars (circled) within the SWB, and with respect to the radio continuum appearance of 3C434.1. The wind-dominant O4V star is found very nearly in the centre of the bubble. There are no stars in Field 2 that match the selection criteria.

We now consider whether the observed wind luminosity and energy requirements of the bubble are met by the winds of the observed candidate stars. For our analysis, we use terminal wind velocities and mass loss rates from the models of Schaerer & de Koter (1997). The adopted parameters are listed in Table 3.4, and it is seen that the integrated wind luminosity of the observed stars is $\dot{M}_6 v_{2000}^2$=3.7, accounting for ~50% of the wind luminosity sustaining the bubble at age 1.4 Myr ($\dot{M}_6 v_{2000}^2$=6.4). This is predominantly from the O4V star.

That there are no other stars observed within this SWB with outputs significant enough to affect the bubble's evolution is likely, considering that B0V stars are the latest type observed here, and these are seen in Tab. 3.4 to have an almost negligible contribution to the wind luminosity $\dot{M}_6 v_{2000}^2$. The missing wind

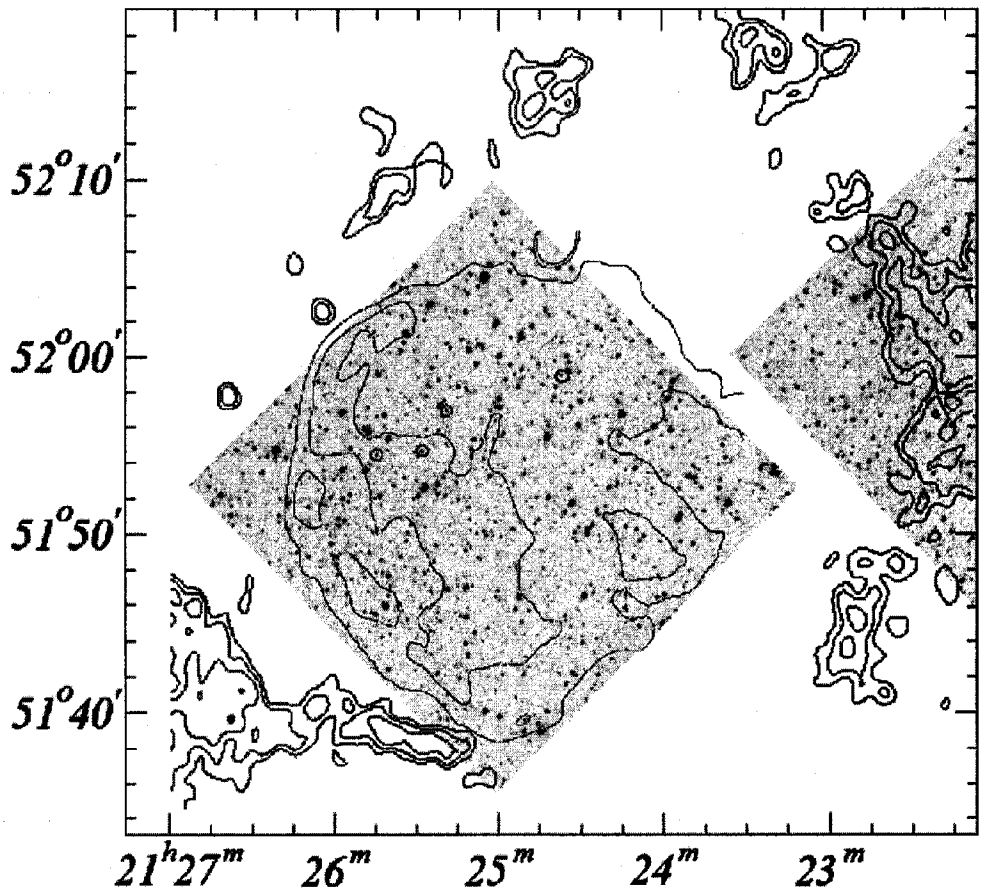

Figure 3.8: A composite optical, radio continuum and H I line image, showing V-band optical images of the sky within the contoured H I line image of the stellar wind bubble. Each optical field of view is $0.5° \times 0.5°$ (that of the Devon Astronomical Observatory telescope). Only part of field 2 (upper right) overlaps the bubble, while field 1 is fully within it. The four stars identified as residents of the SWB (see Sec. 5) are circled. The three B0V stars are seen at left, while the O4V star is very nearly centred within the H I bubble. The continuum contours of 3C434.1 are also drawn, showing the SNR's relation to the SWB and the stars responsible for its formation. Coordinates on axes are $(\alpha, \delta)(J2000)$.

α,δ (J2000)	v_∞ (km s^{-1})	$\log(L/L_\odot)$	M ($M_\odot$)	T_{eff} (10^4 K)	$\dot{M}/10^{-6}$ ($M_\odot$ yr^{-1})	$L_w/10^{36}$ (ergs s^{-1})
$21^h25^m46.2^s$ 51°54′52.5″	2890	4.66	20	3.55	0.088	0.23
$21^h25^m18.7^s$ 51°57′29.2″	2890	4.66	20	3.55	0.088	0.23
$21^h24^m33.7^s$ 51°59′19.4′	3100	5.85	70	5.00	1.30	3.94
$21^h25^m28.8^s$ 51°54′59.3″	2890	4.66	20	3.55	0.088	0.23

Table 3.4: Stars 1, 4, 7 & 10 from Table 3.3 whose photometric distances and reddenings are consistent with the SWB around 3C434.1. Sources of the physical values v_∞, luminosity, mass and effective temperature are from Schaerer & de Koter (1997). The relation $L_w/10^{36}= 1.26\times\dot{M}_6 v_{2000}^2$ is used in the text.

luminosity gives us an estimate of the latest stellar type for the progenitor of SNR 3C434.1. Another O4V star would bring the total internal wind luminosity up to $\dot{M}_6 v_{2000}^2$=6.8, and such a star has a main-sequence lifetime consistent with the upper-limit estimate of the bubble's age (2.6 Myr). The progenitor may even have been of an earlier spectral type than this, but should not have been much cooler, as such a star would have outlived the currently observed O4V star within the bubble. This suggests it is probable that SNR 3C434.1 marks the first supernova event to occur within this bubble, and the explosion was of type Ib or Ic.

Figure 3.8 shows that there is 30% (by area) of the SWB's interior not covered in the optical observations. It is very unlikely that other powerful stars related to the SWB lurk in these peripheral unobserved regions, as their winds would have certainly distorted the elliptical outline of the bubble (see Fig. 3.6).

3.6 Conclusion

We have presented evidence that the H I environment near SNR 3C434.1 has been shaped by a cluster of at least five stars, four of which are still affecting their surroundings, and the fifth of which produced the SNR itself. A thin walled H I shell surrounds the stars and the SNR (at a distance of 5.2±1.1 kpc),

and we confirm what its tattered appearance and low expansion velocity (14 km s^{-1}) suggest: it is an old stellar wind bubble which has hosted only 1 supernova event, and is now beginning to dissipate in the ISM. Much of the shell is comprised of cool (80 K) H I gas, and it is concluded that the far end cap (seen as a dark area amidst a bright emission field) is absorbing emission from a warm uniform background of H I emission. We develop a geometric model of this bubble in three dimensions, and fit it to the bubble's appearance in velocity space.

3.7 Acknowledgements

The authors would like to thank Tom Landecker (DRAO) for his thoughtful comments on our manuscript. The Dominion Radio Astrophysical Observatory is operated as a national facility by the National Research Council of Canada. The Canadian Galactic Plane Survey is a Canadian project with international partners, and is supported by a grant from the Natural Sciences and Engineering Research Council of Canada (NSERC). This work has been supported by NSERC operating grants to T. Landecker, D. Routledge, D. Hube, and S. Morsink. T. Foster has been supported by an NSERC Graduate Scholarship.

Bibliography

[1] Abbott, D. C. 1982, ApJ, 259, 282

[2] Bessel, M. 1990, PASP, 102, 1181

[3] Boyle, R. P., Dasgupta, A. K., Smriglio, F., Straizys, V., and Nandy, K. 1992, A&A, 95, 51

[4] Cappa, C., Pineault, S., Arnal, E. M., & Cichowolski, S. 2002, A&A, 395, 955

[5] Case, G. L., & Bhattacharya, D. 1998, ApJ, 504, 761

[6] Cazzolato, F., & Pineault, S. 2003, AJ, 125, 2050

[7] Chiosi, C., Nasi, E., & Sreenivasan, S. R. 1978, A&A, 63, 103

[8] Clark, D. H., & Caswell, J. L. 1976, MNRAS, 174, 267

[9] Cox, A. N., editor. 2000, Allen's Astrophysical Quantities, New York, Springer-Verlag

[10] Foster, T. & Routledge, D. 2001, A&A, 367, 635 (paper I)

[11] Foster, T., Hube, D., Couch, J., Martin, B., Routledge, D., & Vaneldik, F. 1999, ASP Conference Series, Vol. 189, 111

[12] Foster, T., & Routledge, D. 2003, ApJ, 598, in press

[13] Garmany, C. D. 1994, PASP, 106, 25

[14] Gathier, R., Pottasch, S. R., & Pel, J. W. 1986, A&A, 157, 171

[15] Georgelin, Y. M., & Georgelin, Y. P. 1976, A&A, 49, 57

[16] Gibson, S.J., Taylor, A.R., Higgs, L.A., & Dewdney, P.E. 2000, ApJ, 540, 851

[17] Green, D. A. 1984, MNRAS, 209, 449

[18] Higgs, L. A., & Tapping, K. F. 2000, AJ, 120, 2471

[19] Høg, E., Fabricius, C., Makarov, V. V., Urban, S., Corbin, T., Wycoff, G., Bastian, U., Schwekendiek, P., & Wicenec, A. 2000, A&A, 355, 27

[20] Koo, B-C., & McKee, C. F. 1992, ApJ, 388, 93

[21] Kothes, R., Uyaniker, B., & Pineault, S. 2001, ApJ, 560, 236

[22] Landecker, T. L., Dewdney, P. E., Burgess, T. A., Gray, A. D., Higgs, L. A., Hoffmann, A. P., Hovey, G. J., Karpa, D. R., Lacey, J. D., Prowse, N., Purton, C. R., Roger, R. S., Willis, A. G., Wyslouzil, W., Routledge, D., & Vaneldik, J. F. 2000, A&A, 145, 509

[23] Mantovani, F., Nanni, M., Salter, C., & Tomasi, P. 1982, A&A, 105, 176

[24] McKee, C. F., Van Buren, D., & Lazareff, B. 1984, ApJL, 278, 115

[25] Oja, T. 1996, BaltA. 5, 103

[26] Panagia, N. 1973, AJ, 78, 92

[27] Predehl, P., & Schmitt, J. H. M. M. 1995, A&A, 293, 889

[28] Reich, W., Reich, P., & Fürst, E. 1997, A&A, 126, 413

[29] Roberts, W. 1972, ApJ, 173, 259

[30] Russeil, D. 2003, A&A, 397, 133

[31] Saken, J. M., Shull, J. M., Garmany, C. D., Nichols-Bohlin, J., & Fesen, R. A. 1992, ApJ, 397, 537

[32] Schaerer, D. & de Koter, A. 1997, A&A, 322, 598

[33] Steigman, G., Strittmatter, P. A., & Williams, R. E. 1975, ApJ, 198, 575

[34] Taylor, A. R., Gibson, S. J., Peracaula, M., Martin, P. G., Landecker, T. L., Brunt, C. M., Dewdney, P. E., Dougherty, S. M., Gray, A. D., Higgs, L. A., Kerton, C. R., Knee, L. B. G., Kothes, R., Purton, C. R., Uyaniker, B., Wallace, B. J., Willis, A. G., & Durand, D. 2003, AJ, 125, 3145

[35] Uyaniker, B., Kothes, R., & Brunt, C. M. 2002, ApJ, 565, 1022

[36] Weaver, R., McCray, R., Castor, J., Shapiro, P., & Moore, R. 1977, ApJ, 218, 377

Chapter 4

Reddening and Distances to Four Objects near ℓ=93°

Foreword

The method presented in this thesis was developed over the span of about 18 months, and during this creative period the author was constantly writing and revising the paper that is now published in the Astrophysical Journal (Chapter 2). Based on comparing a measurement of foreground column depth to a total column depth within the framework of a column versus distance model, the method originally used dust column densities (i.e. extinctions, or reddening) to achieve its goals. As well, it was developed to resolve the question of the distance to four Galactic plane objects near $\ell = 93°$. New results of both extinction and distance for these objects came out of this original research. Therefore, it is completely appropriate that selected results of this formative work be included here.

The chapter presents new optical observations of H II regions Sh138 and Sh139 (near $\ell = 110°$), and H II regions NRAO 655, WB89-73, and G93.6+1.3 (near $\ell = 93°$). These optical observations are used to calculate new measurements of extinction (due to dust), which are compared to extinctions found from integrated H I and ^{12}CO column densities and the dust-to-gas ratio A_V/N_H (see Table 4.1). As well, for the first time I present X-ray observations of SNR 3C434.1, and the results of a model fitted to the observed X-ray spectrum of this remnant, which calculates an absorbing column depth that compares favorably to that found by the above integration.

An interesting conclusion is that the $\ell = 93°$ objects NRAO 655, WB89-73, and 3C434.1 are at similar distances near ~ 5 kpc, the same as that of the Perseus Spiral Arm in this direction (e.g. Russeil 2003). Although the study of NRAO 655 and 3C434.1 by Goss et al. (1984) lacked any distance information, this conclusion supports those author's predictions that these objects may share a true spatial proximity. This chapter therefore contributes substantially by confirming this 20 year old mystery. I comment briefly on the association of these objects with the Perseus Arm spiral shock (Roberts 1972) in the final section.

This chapter also demonstrates that the column density $N_H = N_{HI} + 2N_{H_2}$ (where N_{H_2} is proportional to the area under a ^{12}CO T_b emission spectrum) can accurately trace the optically-absorbing material (dust) along lines of sight in

this Galactic plane region. This relationship between gas and dust constitutes a fundamental assumption in many studies of extinction (e.g. to individual objects), and one that is not obviously justified (Astrophysical Journal referee comment on the author's original paper). The author here takes the opportunity to respond to the referee, demonstrating an original solution to a difficult question.

Abstract

Methods that use a multi-wavelength approach to finding the optical extinction to four Galactic plane objects are presented. I demonstrate the techniques on two Sharpless objects (Sh138 and Sh139) near $\ell = 110°$ with known photometric distances that place them in the Perseus spiral arm. These multi-wavelength techniques are then applied to find original values of hydrogen column density and optical absorption to four objects near $\ell = 93°$: three H II regions (NRAO 655, WB89-73, and the newly discovered G93.6+1.3) and one SNR (3C434.1). It is demonstrated that the dust column to an object can be traced by the total hydrogen gas column. As well, new distances to these objects are presented, calculated from the method of Foster & Routledge (2003). The method yields distances to the four objects that are markedly closer than those apparent from kinematic distances that use a flat Galactic rotation curve. This is explained in terms of a spiral shock potential that each object is shown to be subject to. A new picture of this region of the Galactic plane emerges.

4.1 Introduction

In this work, I present applications of two optical extinction methods, and compare their results with those based on atomic and molecular hydrogen column density. Such studies show how well H I+^{12}CO (total hydrogen nuclei column) traces the absorbing material in the interstellar medium (ISM), as found through other methods of optical extinction. The fundamental question concerns whether the spatial distribution of H I and H_2 is the same as that of dust, and hence whether attenuation of optical light by dust (A_V) can be used to trace the col-

umn density of H I plus H_2 between observer and object.

Known values for the column density of H I seen in emission are also used to calculate accurate distances with the method of Chapter 2 (see Foster & Routledge 2003). CGPS 21 cm continuum, H I line and ^{12}CO(J=1-0) line data will be used throughout this chapter (Taylor et al. 2003).

The radio continuum appearance of four objects near $\ell = 93°$ is shown in Fig. 4.1. Optical emission ($H\alpha$) has been newly discovered by the author from all four objects (Fig. 4.2). NRAO 655 and 3C434.1 have similar radial velocities (Foster & Routledge 2001) and are both extremely faint optically. The small H II region WB89-73 appears within the tail of NRAO 655, and is coincident with ^{12}CO emission near $v = -60$ km s^{-1}, and IR source IRAS 21202+5157. I have also discovered a new nebula, G93.6+1.3, which appears bright optically (λ656.3 nm), and very faint in radio continuum. CGPS polarization data shows that it appears as an conspicuously unpolarized source amidst a polarized field. Its distance suggests it is probably a foreground H II region (see Sec. 4.3.3), and it appears to depolarize 21 cm emission originating behind it.

I demonstrate the extinction methods on two objects lying directly in the Galactic plane (b=0°) with known non-kinematic distances: Sh139 (r=3.3 kpc) and Sh138 (r=4.8 kpc). I then apply the techniques to the above four objects, and derive new values of extinction and distance to each. Previous to this study, distances to these objects were either unknown (3C434.1 and G93.6+1.3) or kinematic only (NRAO 655 and WB89-73). Extinctions to any of these objects have not previously been published.

4.1.1 A Multi-Wavelength Approach to Determining Optical Absorption

Classically, one measures the optical extinction to a gaseous object (e.g. planetary nebula, or H II region) by finding the intensity ratio of two observable lines (one of which may be a radio line). The lines are attenuated differently due to the λ^{-1} wavelength dependence of scattering. Recombination lines such as $H\alpha$, $H\beta$, and $H158\alpha$ are favoured in this approach. Surveys such as the CGPS have made available high-resolution radio continuum and spectral line

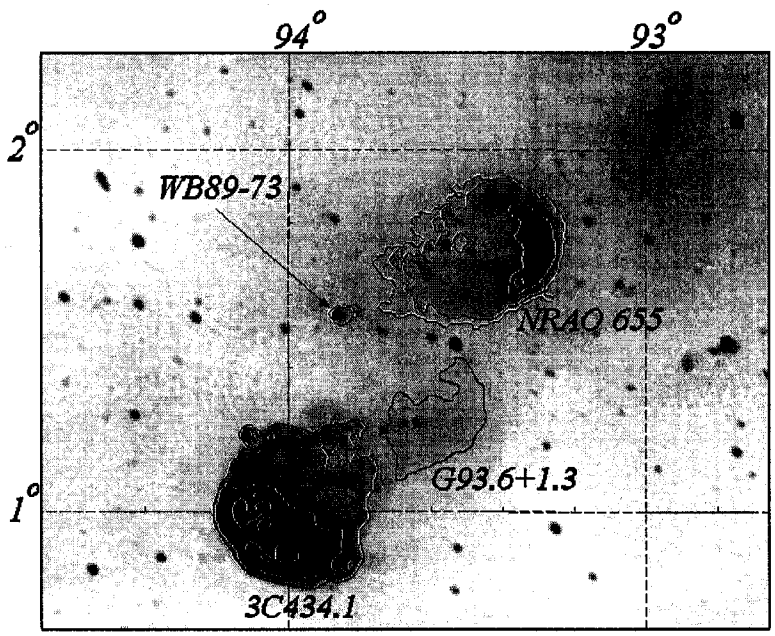

Figure 4.1: The λ=21 cm radio continuum appearance of the $\ell = 93°$ Galactic plane region, as imaged by the Canadian Galactic Plane Survey. The four objects principal to this study are shown.

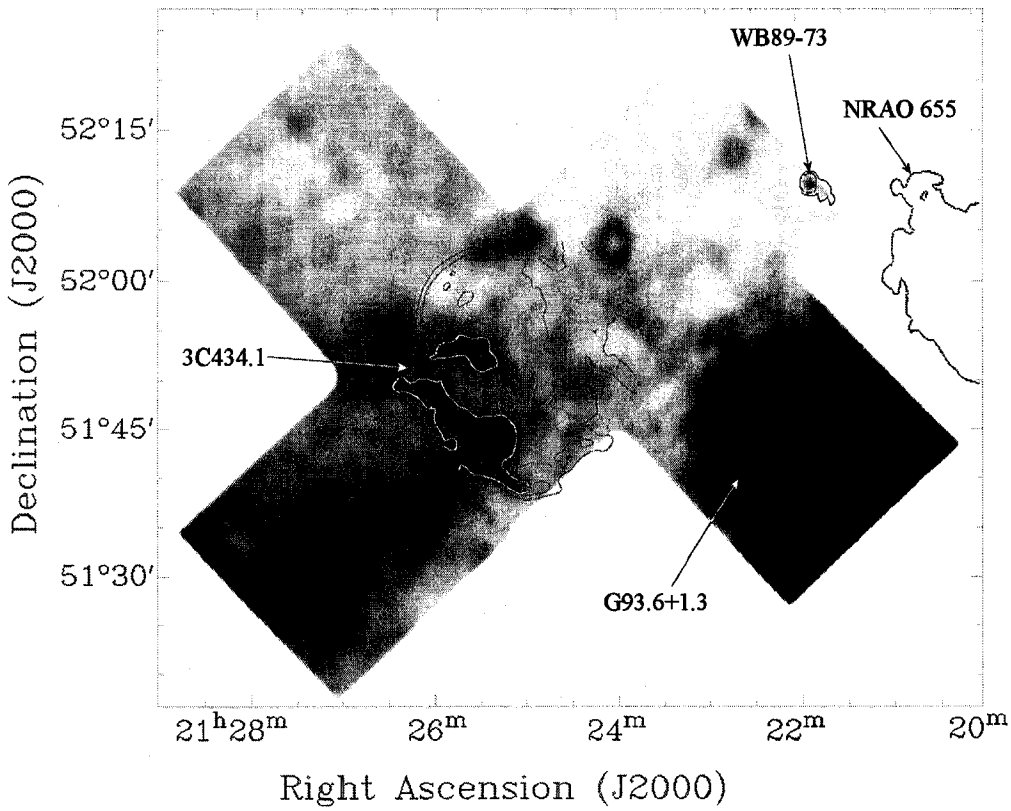

Figure 4.2: Optical $H\alpha$ emission line mosaic centred on $\ell = 94°$, $b = 1°$, with 21 cm radio-continuum contours overlaid. Stars have been removed by point-spread function (PSF) fitting routines (IRAF), and the image convolved to the resolution of the CGPS 21 cm continuum image ($\simeq 1'$). The $H\alpha$ appearance of NRAO 655 is presented in Foster & Routledge (2001). Images for this mosaic were obtained by the author at the University of Alberta Devon Astronomical Observatory (DevonAO). Dark is brighter $H\alpha$ emission.

(H I and ^{12}CO(J=1-0)) images for the first time. An H II region's emission measure can be determined from radio continuum brightness, and the ratio of this to the emission measure found from the attenuated $H\alpha$ line emission determines the extinction along the line-of-sight. Radio line images in H I and ^{12}CO emission make it possible to determine accurate hydrogen column densities, from which a value of A_V or $E(B-V)$ is found, via the well-determined relation between optical absorption and interstellar hydrogen column density (see Tab. 4.1). With H I absorption spectra derived from CGPS data, such column densities to objects can now be found with unprecedented accuracy. As well, models of a supernova remnant's X-ray spectrum can independently lead to N_H (see Sec. 4.4), and therefore A_V.

4.1.2 Determining Absorption to Objects with Known Radial Velocities

I employ CGPS H I and ^{12}CO emission spectra (^{12}CO data for the region ℓ = 93° courtesy T. Dame, Dame et al. 2000) to measure accurate column densities to Galactic objects, and determine A_V via the very recent gas-to-dust ratio N_H/A_V=1.57± 0.10×10^{21} cm^{-2} mag^{-1} (Vuong et al. 2003: see Table 4.1). The common value of this parameter determined over the years encourages one to believe that determining extinction this way leads to very reasonable values. This method of measuring extinction also has the advantage of allowing one to inspect the absorbing column for dense local clouds not accounted for in models of large-scale Galactic distribution of material.

The following relation finds the line-of-sight column density of atomic and molecular Galactic hydrogen (referred to in this chapter as "total") from H I and ^{12}CO line emission:

$$N_H(\mathrm{cm}^{-2}) = N_{HI}+2N_{H_2} = 1.823\times10^{18}\int^{v_{obj}} T_{b(HI)}dv+2\left(2.8\times10^{20}\int T_{b(CO)}dv\right) \quad (4.1)$$

where the expression for N_{HI} is from Rohlfs & Wilson (1996), and for N_{H_2} from Elmegreen (1998). With observed H I and ^{12}CO emission profiles towards an

Reference (year)	1 (1975)	2 (1975)	3 (1978)	4 (1979)	5 (1995)	6 (2003)
N_H/A_V	[2.2]	[1.9]	[1.9]	1.89	1.79 ± 0.03	1.57 ± 0.1
$N_H/E(B-V)$	6.8 ± 1.6	5.9 ± 1.6	5.8	[5.9]	[5.6]	[4.9]

Table 4.1: Published ratios of total Galactic hydrogen to visual extinction N_H/A_V, or to reddening $N_H/E(B-V)$, in units of (10^{21} cm^{-2} mag^{-1}). Sources and references are 1) Gorenstein 1975, 2) Ryter et al. 1975, 3) *(Copernicus)* Bohlin et al. 1978, 4) Savage & Mathis 1979, 5) *(ROSAT)* Predehl & Schmitt 1995, and 6) Vuong et al. 2003. Values in brackets are calculated using the published ratios and dust law parameter R_V=3.1.

object, one integrates the emission using the object velocity as the lower limit to obtain A_V(object).

It should be noted that the expression above for N_{HI} assumes the λ21 cm H I emission is optically thin ($\tau \ll 1$). If this assumption fails, the above equation underestimates N_{HI} by the factor $\tau/[1-exp(-\tau)]$, since cooler optically thick gas is not readily seen in emission and is therefore not included in the integration. There are two effects of cold H I on the derived N_{HI} values. 1) A double undercounting in the presence of H I Self-Absorption (HISA) is possible, i.e. a positive contribution to column density, contributing negatively to the H I line intensity. 2) A saturation effect (for those lines of sight which are not self-absorbed). Many small-angular-size concentrations of cold material in the Perseus Arm have optical depths of 1 or greater (Gibson et al. 2000), which leads to an underestimation of the H I column depth (by Eqn. 4.1) by 60%. However, H I emission over a large angular area (e.g. the size of an H II region) generally underestimates the total column by a much smaller fraction.

Whereas the expression for N_{HI} in Eqn. 4.1 is valid only for optically thin radiation, a more general expression applicable regardless of the presence of cold H I is:

$$N_{HI}(\mathrm{cm}^{-2}) = 1.823 \times 10^{18} T_s\,(\mathrm{K}) \int^{v_{obj}} \tau(v) dv \qquad (4.2)$$

where the optical depth $\tau \equiv \tau(v)$[1] and the spin temperature T_s (generally the

[1]For $\tau \ll 1$, $T_b = T_s[1-exp(-\tau)] \approx T_s\tau$, and N_{HI} in Eqn. 4.1 results from Eqn. 4.2.

kinetic temperature of neutral hydrogen gas) are found by measuring H I in absorption (Rohlfs & Wilson 1996). Observing absorption against a bright extragalactic source found near one's target object, one can estimate the optical depth of large scale features (like the Perseus Spiral Arm). This method also yields very accurate foreground column densities to one's target source, but to be seen in absorption, the source's continuum brightness temperature must be higher than the mean brightness temperature of the surrounding H I.

Column densities derived from H I seen in absorption more accurately describe the total column, but are usually measured along a column with a very small angular width relative to that of an extended object. Thus, such column densities may not accurately reflect the mean extinction over an extended object, for example extended H II regions. Further, very few extended sources of interest are bright enough to be seen in absorption. Of the objects in this study, WB89-73 and Sh138 are both small-scale (one beamwidth) and bright enough to be absorbed, and I have used Eqn. 4.2 to find the extinction A_V(object) to these two objects. Where H I emission alone is used to measure A_V(object), the mean brightness temperature T_b was derived from within a box centred on the source and large enough to include some of its surroundings. Fig. 4.3 presents H I and ^{12}CO spectral profiles towards each of the four objects in the $\ell = 93°$ area, each derived from a $0.5° \times 0.5°$ box centred on each of the objects. The profile towards NRAO 655 (from the highest-latitude box) contains a very bright CO emission feature near $v = -6$ km s^{-1}, indicative of a local cloud of molecular gas in this direction. A weaker signal at a similar velocity is seen in spectra towards 3C434.1 and WB89-73, and is absent from the spectrum of G93.6+1.3. Further, WB89-73 is known to be associated with a ^{12}CO feature near $v = -60$ km s^{-1}. Both NRAO 655 and WB89-73 are also associated with bright dust emission (seen in Fig. 4.4).

I shall return to these objects in Section 4.3 after demonstrating the method on two H II regions of known distance.

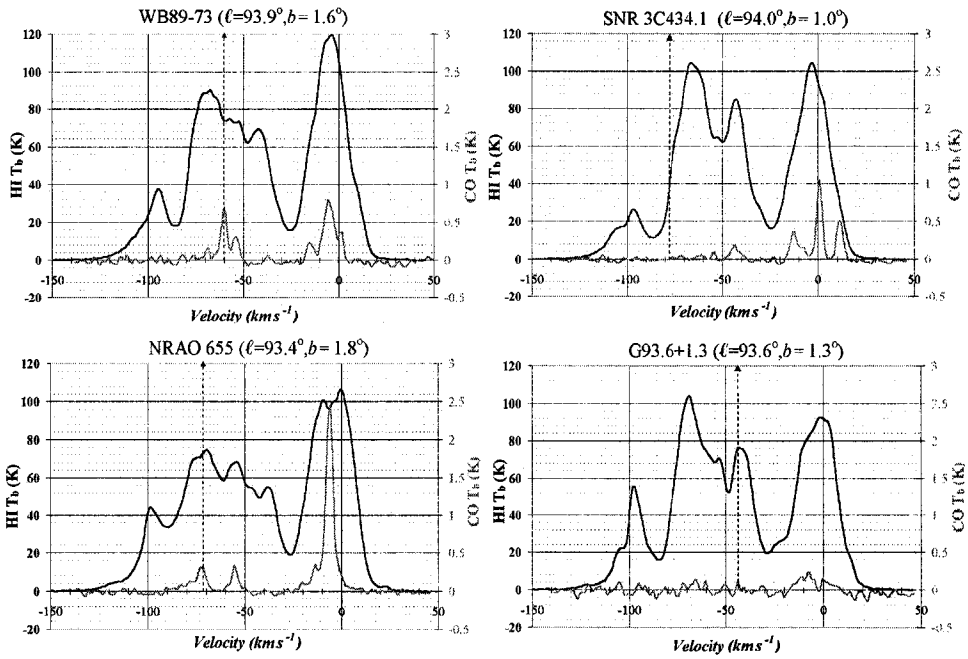

Figure 4.3: H I and ^{12}CO spectral profiles towards the four objects in this study. All charts are similarly scaled, with CO spectra appearing as the lower of the two curves in each graph. Systemic velocities for H I associated with each object are shown (dashed lines).

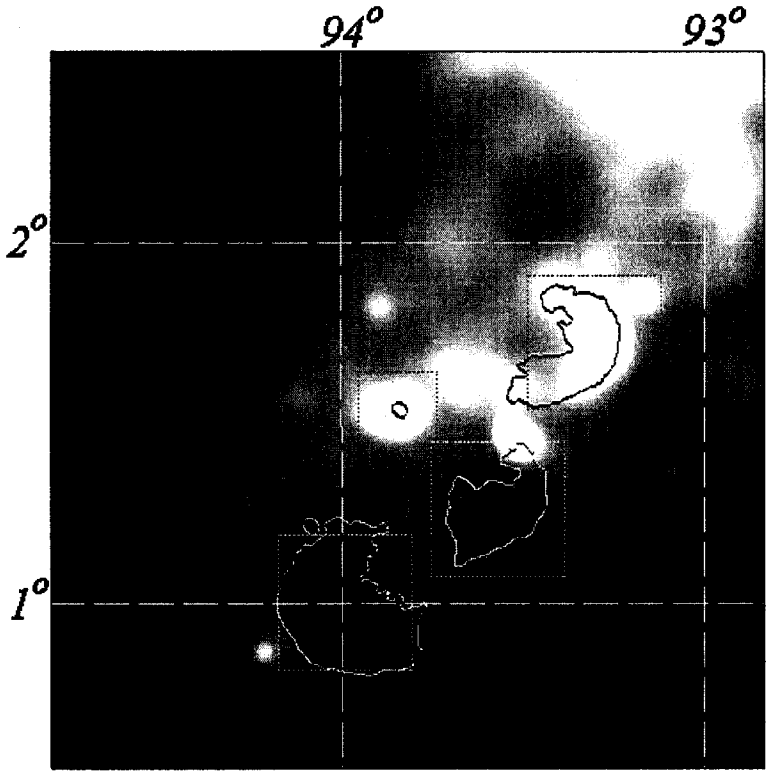

Figure 4.4: IRAS 100 μm image of dust emission towards $\ell = 93°$, $b = 1°$, with CGPS 21 cm radio-continuum contours overlaid. Note that WB89-73 and NRAO 655 are both sources of IR. The boxes shown are regions from which mean brightness temperatures of H I (in emission) and ^{12}CO were extracted to form the spectra in Fig. 4.3.

4.2 Extinction Methods Applied To Objects near $\ell = 110°$

In the direction of $\ell = 110°$, several H II regions exist which were catalogued by Sharpless, and since then observations of stars have added spectrophotometric distances for each. Sh138 ($\ell = 105.6°$, $b = 0.3°$) is a compact H II region 5.0±1 kpc distant (Deharveng et al. 1999). Sh139 (ℓ =105.8°, $b = 0.0°$) is an extended, diffuse H II region, and is found to be 3.3±1.1 kpc from the Sun in Fich, Blitz & Stark (1989). These nebulae are present in CGPS 21 cm radio continuum, H I and ^{12}CO radio line data, and the author has observed them in the optical H I recombination lines $H\alpha$ and $H\beta$. I demonstrate three independent methods here to find the extinction A_V towards these objects, and show the corresponding distances match those known for the objects within their uncertainties.

Balmer line observations of Sh138 and Sh139 were made with the high performance CCD system at the University of Alberta's Devon Astronomical Observatory (DevonAO, Foster et al. 1999), a system the author has been responsible for, spearheading the design and testing of the instrumentation, and developing the control software (see Foster 2000). Images in $H\alpha$ (656.3 nm) and $H\beta$ (486.9 nm) were made over a wide airmass range. Our line filters are identical in bandwidth (FWHM=7.5 nm) and the CCD quantum efficiencies roughly equal in both bands, so a direct ratio of the extra-atmospheric fluxes (derived from nightly extinction coefficients) gives the reddened intensity ratio, $I_{H\alpha}/I_{H\beta}$. The N II lines (λ =654.8 nm and λ =658.3 nm) are within the passband of our $H\alpha$ filter. N II fluxes were estimated and removed using the filter's transmission curve, and the average ratio for $I_{NII=658.3}/I_{H\alpha}$=0.36 observed in H II regions in the galaxy M83 (Brand et al. 1981). An *intrinsic* Balmer-line intensity ratio of 2.74 is calculated by Osterbrock (1974) for T_e=10^4 K. I derive the parameters for Sh138 and Sh139 tabulated in Tab. 4.2. Logarithmic extinction c is found from the equation:

$$\frac{I_{H\alpha}}{I_{H\beta}} = \left(\frac{I_{H\alpha}}{I_{H\beta}}\right)_0 10^{-c[f(H\alpha)-f(H\beta)]} \tag{4.3}$$

where the $H\alpha$ extinction relative to $H\beta$ is given by the standard interstellar

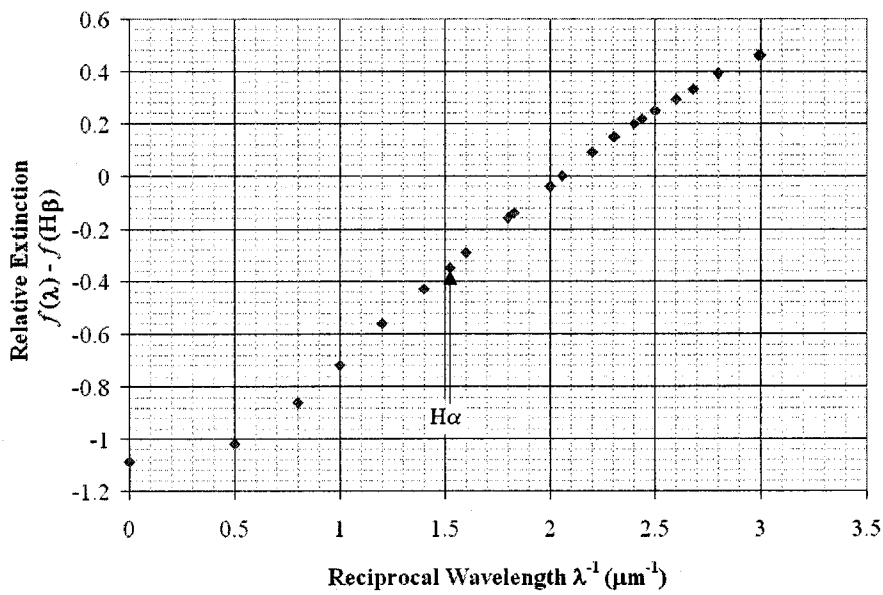

Figure 4.5: The relationship between wavelength and differential extinction, normalized relative to the $H\beta$ line (2.057 μm^{-1}). The $H\alpha$ line ($f(H\alpha)-f(H\beta)$=−0.35) is arrowed. From Whitford 1958.

extinction curve (Figure 4.5, Whitford 1958) as being −0.35. The conversion $c = 1.47E(B-V)$ (Feibelman 1982) and a ratio of total-to-selective extinction R_V=3.1 is used to express the result in visual magnitudes of extinction A_V.

If interstellar dust effects were not present, one should find the emission measures of an H II region, as measured in optical and radio wavelengths, to be identical. An optical line and the 21 cm radio continuum can thus be used to measure the extinction, since the interstellar medium (ISM) is essentially lossless at 1.4 GHz. Both Sharpless regions are visible in 21 cm CGPS images, from which we derive mean brightness temperatures of each. Within an aperture of the same angular extent, the nebular flux in $H\alpha$ was measured from the DevonAO image. Emission measures were corrected for the beam-width difference between the DRAO Synthesis Telescope (FWHM$\simeq$ 60″) and the seeing at the DevonAO site (FWHM$\simeq$ 6″). The *apparent* emission measure from the $H\alpha$ data and equation 1 from Reynolds (1988) is:

$$EM_{H\alpha}(\mathrm{cm^6\ pc^{-1}}) = 2.75 \left(\frac{T_e}{10^4\ \mathrm{K}}\right)^{0.9} I_\alpha \tag{4.4}$$

where I_α is the intensity of $H\alpha$ emission in Rayleighs (1 Rayleigh=$10^6/4\pi$ photons $\mathrm{cm^{-2}\ s^{-1}\ sr^{-1}}$).

If no absorption of optical emission by the intervening ISM were present, this value should be identical with the emission measure obtained with 21 cm data:

$$EM_{21\ cm} = 12.14 \left(\frac{T_b}{\mathrm{K}}\right) \left(\frac{T_e}{\mathrm{K}}\right)^{0.35} \left(\frac{\nu}{\mathrm{GHz}}\right)^{2.1} \mathrm{cm^6\ pc^{-1}} \tag{4.5}$$

where here ν is the frequency 1.42 GHz. The visual extinction A_V suggested by the ratio of Eqn.s 4.4 and 4.5 is found as:

$$A_V(\mathrm{mag}) = 1.28 \times 2.5 log \left(\frac{EM_{21\ cm}}{EM_{H\alpha}}\right) \tag{4.6}$$

where the factor of 1.28 converts the resulting $H\alpha$ extinction into visual magnitudes A_V (from the reddening curve of Whitford 1958).

Both Sharpless objects are known to be associated with CO emission from molecular material. This is confirmed with images of ^{12}CO emission made for the CGPS. The spectrum of Sh139 (Fig. 4.6) shows peak emission near $v = -46$ km s^{-1} and $v = -54$ km s^{-1}. On the ^{12}CO images near $v = -54$ km s^{-1} a wall of emission neatly wrapping around the radio continuum emission from the south "head" of Sh139 is seen. A systemic radial velocity of $v_{obj} = -50 \pm 4$ km s^{-1} is adopted for the nebula. H I and CO line emission in a 12′× 12′ box containing Sh139 was integrated to $v = -50$ km s^{-1}, and N_H calculated using Eqn. 4.1. Using the gas-to-dust ratio N_H/A_V=1.57± 0.1× 10^{21} cm^{-2} mag^{-1}, the integral of N_H=5.02±0.48×10^{21} cm^{-2} represents a visual extinction of A_V=3.2± 0.4 magnitudes.

The 21 cm continuum emission of Sh138 (T_b=96 K) is brighter than the mean H I line emission of its surroundings, so an H I absorption profile can be used to count N_{HI}. Two minima in the H I absorption profile (Fig. 4.6) are seen at $v = -49.3$ km s^{-1} and $v = -53.4$ km s^{-1}, dense material that brackets an emission peak from ^{12}CO gas, located between these velocities at $v = -52.4$ km s^{-1}.

This is similar to the velocity of the ionized gas ($v = -50\pm 2$ km s^{-1}) reported by Deharveng et al. (1999) and ($v = -52.1$ km s^{-1}) by Peeters et al. (2002). Integrating only the ^{12}CO to velocity $v_{obj} = -52.4$ km s^{-1}, and the entire absorbed H I column to $v = -60$ km s^{-1}, the total hydrogen-gas column density N_H=1.14±0.14×10^{22} cm^{-2} is found, or A_V=7.27± 0.87 magnitudes.

Tab. 4.2 shows the results of the above three methods for calculating A_V (and $E(B-V)$) to Sh138 and Sh139. The calculations of extinction A_V (via direct emission measures, and the dust-surrogate of H I+^{12}CO column) are very similar, suggesting that H I+^{12}CO reasonably traces the dust. Even more intriguing is that total extinction values exceed those of the selective values ($E(B-V)$) by a factor that is more than the canonical factor of R_V=3.1 (valid for the smooth ISM). The mean dust law parameter in the line of sight towards H II region Sh138 is found to be $R_V = A_V / E(B-V) \sim 4$, indicative of this region's association with a great amount of internal dust (Neckel & Chini 1981). Indeed, MSX and IRAS images of this H II region show strong emission at 8 μm and 60 μm, indicative of thermally radiating dust. Sh139 appears to be associated with very little dust emission, consistent with its lower measured reddening (0.7 magnitudes less than Sh138). Its extinction therefore likely originates from the foreground ISM dust since its measured dust parameter R_V=3.4 is close to the canonical ISM value.

From the method in Chapter 2, the distances to both Sh138 and Sh139 are found to be similar at $r \sim 3.1 \pm 0.5$ kpc. The fitted value of the heliocentric distance to the Perseus Arm's centre is R_m=3.2 kpc, which agrees well with other models of the outer Galaxy (e.g. Georgelin & Georgelin 1976, Russeil 2003). These two H II regions are obviously Spiral arm residents. From a flat circular model of Galactic rotation (with R_0=8 kpc and θ_0=220 km s^{-1}) the common distance predicted by these objects' similar velocity is 5.1 kpc. Thus, if the above rotation model holds true in this direction, a non-circular velocity contribution of +24 km s^{-1} is indicated.

While velocities and distances are similar for both objects, their photometric distances are quite dissimilar. The distance to Sh139 (3.3±1.1 kpc) is consistent with our measurement (and with that to the Perseus Arm) while that of Sh138 (5.0± 1.0 kpc) is better matched to its kinematic estimate. So which is correct?

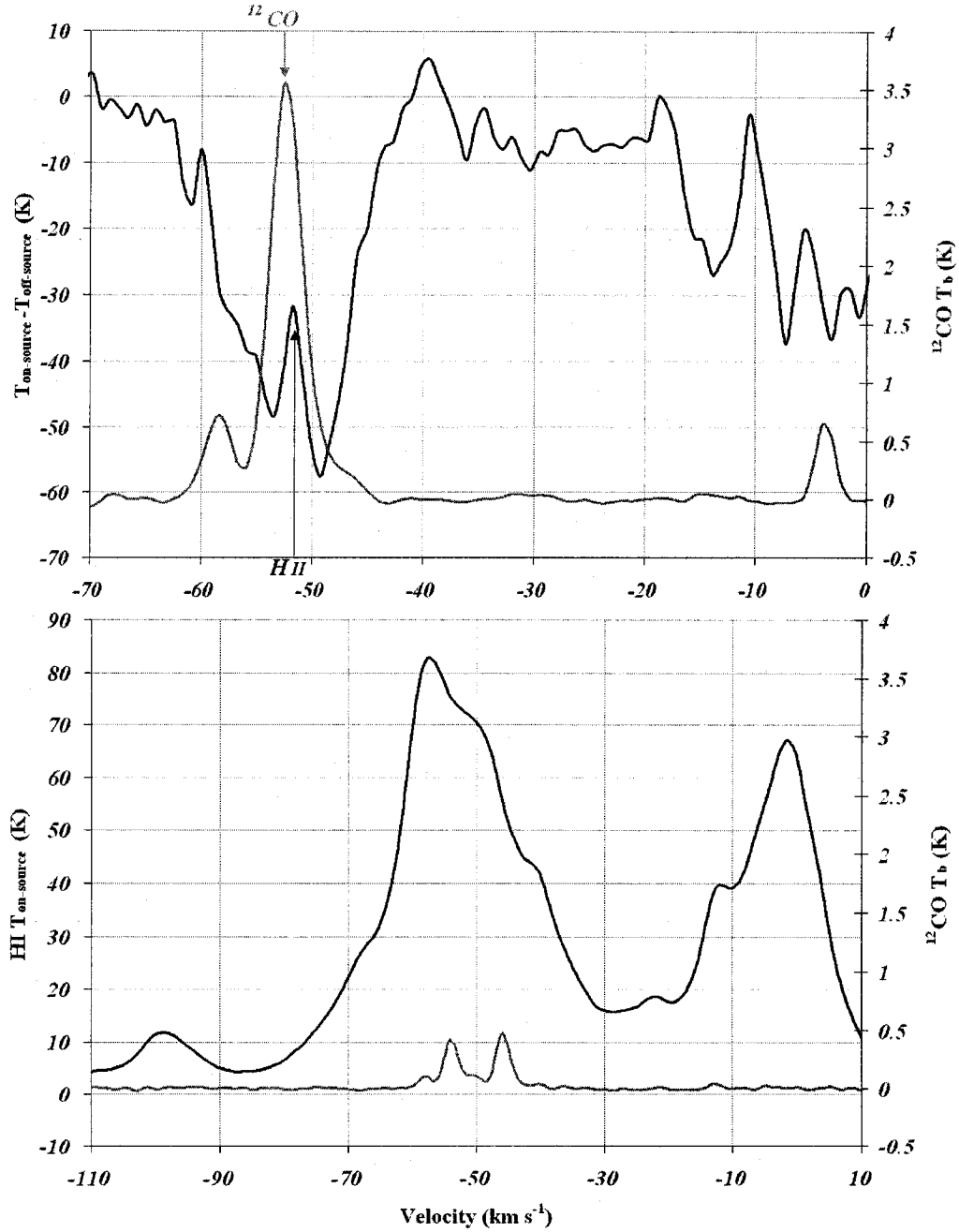

Figure 4.6: H I and ^{12}CO spectra towards Sh138 (top) and Sh139 (bottom). The ^{12}CO feature associated with Sh138 ($v_{obj} = -52.4$ km s^{-1}) is arrowed, as is the velocity of the ionized hydrogen associated with this object. For Sh139, an H I brightness temperature ($T_{on-source}$) emission spectrum is shown, while for Sh138 an H I absorption spectrum ($T_{on-source} - T_{off-source}$) is shown.

Quantity	Sh138	Sh139
$I_{H\alpha}/I_{H\beta}$	19.74± 4.28	8.66±1.70
c	2.45± 0.27	1.43± 0.24
$E(B-V)$ (mag)	1.67± 0.18	0.97± 0.17
$EM_{H\alpha}$ (cm^6 pc^{-1})	479.0± 143.2	83.8± 20.0
$EM_{21\ cm}$ (cm^6 pc^{-1})	54600± 2340	891± 255
A_V (mag)	6.58± 0.42	3.29± 0.52
A_V from N_H (mag)	7.27± 0.87	3.20± 0.37
Mean R_V	4.1± 0.5	3.4± 0.8

Table 4.2: Three determinations of extinction A_V (or $E(B-V)$) for Sh138 and Sh139 derived from Balmer line ratio ($H\alpha/H\beta$), emission measure (21 cm/$H\alpha$) ratio (calculated assuming T_e =10^4 K), and foreground column density (N_H). Values of reddening law parameter R_V estimated from the extinction/reddening pairs are shown as well.

The reddening parameter R_V can be used to explain the problem. For Sh138 the reddening parameter R_V=4.1 is larger than the value of 3.1 which is expected for dust smoothly distributed through the ISM. A photometric distance using A_V=3.1$E(B-V)$ would have underestimated the total extinction to the stars in Sh138, and overestimated the distance-modulus $m_V - M_V - R_V E(B-V)$=$-5+5log_{10}(r)$. Deharveng et al. suggest that only 0.9 magnitudes of reddening originates with the foreground, a value that is confirmed when integrating H I+^{12}CO to the line of sight velocity where the ^{12}CO associated with the nebula just starts to appear ($v = -47.6$ km s^{-1}, where A_V=3.0). This suggests that the value of R_V within the dust shell of Sh138 is at least 4.4.

4.3 New Non-Kinematic Distances to the Three H II Regions

Having demonstrated the consistency of the extinction methods on objects near $\ell = 110°$, we shall now find extinctions and distances to the three thermal objects in the $\ell = 93°$, $b = 1°$ region which were introduced in Sections 4.1 and 4.2. The methods for measuring A_V and $E(B-V)$ presented in the previous section are

applied, and a brief comment on each object is given.

4.3.1 The Extinction and Distance to WB89-73

A distant object with only a kinematic distance available, radio source G93.9+1.6, or WB89-73 ($\ell = 93.86°$, $b = 1.55°$) is classed as an ultracompact H II region. Molecular material was detected in ^{12}CO by Wouterloot & Brand (1989), who found two velocities of $v = -5.4$ and -59.6 km s^{-1}. I confirm this using ^{12}CO data (courtesy T. Dame, Center for Astrophysics, Dame et al. 2001), finding $v = -5.8$ and -60.5 km s^{-1} (see Fig. 4.3). The CO with velocity $v = -5.8$ km s^{-1} is local, thus the systemic velocity adopted for the object is $v_{obj} = -60$ km s^{-1}. Using a flat Galactic rotation model (R_0=8 kpc, θ_0=220 km s^{-1}), a kinematic distance of 7.0 kpc is found for the object.

Optical emission from WB89-73 was discovered by the author in 2001 January in a deep $H\alpha$ survey of fields surrounding the nearby SNR 3C434.1. It is observed as a 1′ source in the CGPS 21 cm and 74 cm radio continuum maps, lying near the end of H II region NRAO 655's extended tail (Foster & Routledge 2001). The source appears connected to NRAO 655 by a diffuse background surrounding both nebulae (see Fig. 4.1). I find a radio flux density of $S_{21\ cm}$=337± 8 mJy, and an $H\alpha$ surface brightness of 174.3± 44.2 Rayleighs for WB89-73.

The emission measure determined from $H\alpha$ at the same image resolution as at 21 cm (Eqn. 4.4, assuming T_e=10000 K) is $EM_{H\alpha}$=18.5± 4.7 cm^{-6} pc, while from 21 cm continuum (Eqn. 4.5) we find $EM_{21\ cm}$=29900± 1500 cm^{-6} pc. The extinction is thus found (using Eqn. 4.6) to be A_V=10.31± 0.36.

In the $H\beta$ line, the nebular emission is extremely faint, attesting to a high reddening. A CCD composite image of twelve 600 second integrations was made to detect the extremely faint $H\beta$ line emission. Using this with the DevonAO $H\alpha$ image, I derive a reddened intensity ratio of $I_{H\alpha}/I_{H\beta}$=57.2± 17.6 for WB89-73. The resulting logarithmic extinction of c=3.77± 0.38 is equivalent to a reddening of $E(B-V)$=2.56± 0.26 mag.

I derive N_{HI}=1.33×10^{22} cm^{-2} from the H I absorption spectrum towards the object (Eqn. 4.2). The ^{12}CO emission profile (see Fig. 4.3) is integrated to obtain N_{H_2}=2.24×10^{21} cm^{-2}, and I find a total column density of N_H=1.77×10^{22} cm^{-2},

	$I_{H\alpha}/I_{H\beta}$	$EM_{21\ cm}/EM_{H\alpha}$	N_H
A_V(mag)		10.31±0.36	11.30±1.56
$E(B-V)$(mag)	2.56±0.26		

Table 4.3: Results of three independent methods used to find visual magnitudes of extinction (and reddening) to WB89-73. The value of the reddening parameter R_V=4.0 found is a mean value for the whole column between the observer and the ionized gas that comprises this ultracompact H II region.

or total extinction A_V=11.30±1.56 mag to WB89-73. This method of determining extinction implicitly assumes that the H I and ^{12}CO emission integrated to the object's systemic velocity is truly from material foreground to the object. A velocity profile of the on-source brightness-temperature ($T_{on-source}$) and the mean background $T_{off-source}$ for WB89-73 shows $T_{on-source} < T_{off-source}$ for all velocities more positive than $v_{obj} = -60$ km s^{-1}, indicating that material in this range is indeed foreground. A similar plot for the nearby extragalactic source 4C51.45 shows absorption features at more negative velocities, not seen in the profile for WB89-73. This demonstrates that emission seen at $v < -60$ km s^{-1} is from material behind this H II region.

Table 4.3 summarizes all extinction measurements to WB89-73. An error-weighted mean total extinction A_V=10.5 mag towards WB89-73 is found. With the independently measure $E(B-V)$, a reddening law parameter of R_V ~4.1 is determinable. As with Sh138, WB89-73 must be associated with a significant amount of internal dust. Indeed, the MSX 8 μm image (see Figure 4.7) shows bright concentrated dust emission from WB89-73.

WB89-73 is also a bright source of emission in all four IRAS wavelength bands. One can make use of these data to estimate an upper-limit distance to WB89-73, using a comparison of radio and IR fluxes (as detailed in Chapter 2). I derive two measures for the nebula: the ionizing luminosity via the observed radio flux density, and the total IR luminosity from flux densities in each of the four IRAS bands. Both values depend on the square of the source distance, hence the ratio of these observables is distance-independent. The underlying assumption here is that all of the Lyman-α photons from the embedded stellar flux are reprocessed into IR emission. This assumption is more sound for ul-

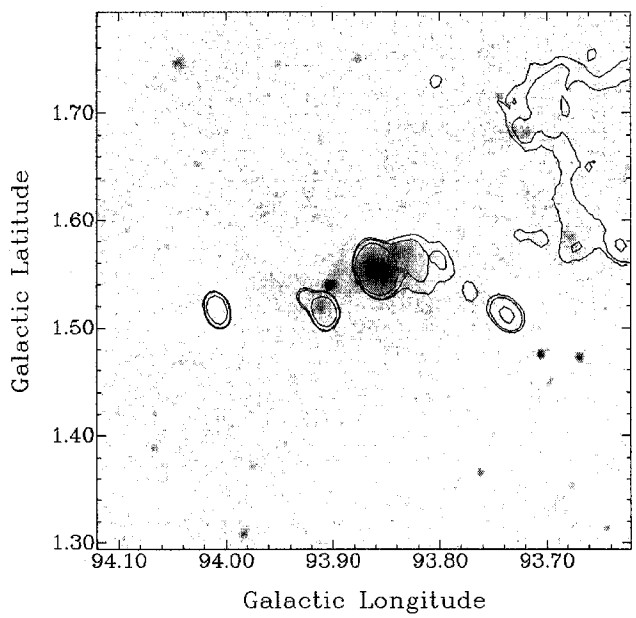

Figure 4.7: Dust emission from WB89-73 as seen by the MSX satellite in the *A*-band (λ=8 μm). The contoured appearance of this ultracompact H II region is from the 21 cm radio continuum image (CGPS data).

tracompact H II regions than for more diffuse nebulae (Charles Kerton, private communication).

Assuming T_e=10^4 K, I find that a star of spectral type O9.5 would produce the observed IR luminosity of L=3.627±0.151× 10^4 $L_\odot$, and obtain an upper-limit distance estimate of 4.7 kpc. A factor of 2 error in T_e affects the distance by only 17%.

The distance measured using the method of Foster & Routledge is 4.3± 0.6 kpc (limit error), while the centre of the Perseus Arm is found 4.6 kpc distant in this direction. The upper limit estimate is in fine agreement with this distance. The kinematic distance of 7.0 kpc is discordant with both the above and the radio/IR limit. A line-of-sight velocity excess of +28± 8 km s^{-1} from that expected from flat circular rotation (R_0=8 kpc, θ_0=220 km s^{-1}) is found for WB89-73. The uncertainty of 8 km s^{-1} is the mean velocity dispersion of gas in the Perseus arm (6-10 km s^{-1}; Roberts 1972).

4.3.2 A New Extinction and Distance to NRAO 655

NRAO 655 (ℓ = 93.4°, b = 1.8°) is a large, extended H II region that probably formed within the boundary of a cloud of H_2, the cloud being located in a tenuous medium with a density gradient approximating a power law. The north-east extension or radio-continuum tail suggests that a "champagne flow" formed as the Strömgren sphere broke through the edge of the cloud and flowed into the surrounding lower-density ISM. The nature of radio and optical line emission from this nebula are detailed by Foster & Routledge (2001), who found a kinematic distance of r=8.8 kpc (with R_0=8.5 kpc; 8.3 kpc results with R_0=8 kpc).

I observed recombination line emission from NRAO 655 in the $H158\alpha$ line (1651.541 MHz) using the 26 m paraboloid at the Dominion Radio Astrophysical Observatory. The detected line is centred near v = −70.6 km s^{-1}, and has width Δv=32.3 km s^{-1}. The velocity of the line is essentially identical to that of an H I cavity identified in CGPS data by the authors at v_{obj} = −71.5 km s^{-1}. The total column density integrated to this velocity (N_H=1.945×10^{22} cm^{-2} ± 10%) corresponds to an extinction of A_V=12.39± 1.47 mag.

This H II region was also detected and imaged optically in the $H\alpha$ line with

the 0.5 m DevonAO telescope. The surface-brightness is quite faint at 15.24±3.6 Rayleighs, and the integrated flux density of the $H\alpha$ emission is S_{656nm}=0.66±0.16 Jy. I find an apparent emission measure of $EM_{H\alpha}$=0.51± 0.12 cm^6 pc^{-1} at the resolution of the radio image, while the mean 21 cm continuum brightness temperature T_b=5.11 K (± 5%) suggests an absolute emission measure of $EM_{21\ cm}$=3258 cm^6 pc^{-1}. The optical extinction to NRAO 655 given by Eqn. 4.5 is A_V=12.17± 0.34 mag.

The error-weighted mean value of extinction to NRAO 655 is A_V=12.2 mag. The distance to NRAO 655 is estimated as r=4.8± 0.8 kpc, significantly different from the kinematic distance of 8.8 kpc. A line of sight velocity excess of +36± 8 km s^{-1} is indicated.

4.3.3 The Extinction and Distance to G93.6+1.3

Here, I report the discovery of a new nebula, G93.6+1.3 ($\ell = 93.6°, b = 1.3°$). This uncatalogued object is visible in the 21 cm (Fig. 4.1) and 74 cm radio continuum maps from the CGPS, as well as continuum maps from the 11 cm Galactic Plane survey of Reich et al. (1984). It is very weak at radio wavelengths, having a 21 cm integrated flux density of $S_{21\ cm}$=0.35 Jy, though its angular diameter is $\simeq$15′. With data from the above three frequencies one finds an optically-thin thermal spectral index of α=0.16±0.12 (where flux density at frequency ν is S(Jy)$\propto \nu^{-\alpha}$). In $H\alpha$ emission line images from the DevonAO, its surface brightness dominates those of the objects in the region ℓ=93°, b=1°, and the emission exhibits an oval shape elongated North-South (15′×11′) (see Fig. 4.2). The integrated surface brightness at 656.3 nm is 12.2±3.6 Rayleighs, or a flux density (in $H\alpha$) of S_{656nm}=0.47 Jy. No optical emission "bridge" is seen connecting it to the SNR.

A very distinct cavity in neutral hydrogen exists at the coordinates of the optical nebula (Fig. 4.8). The systemic velocity of this H I hollow is $v_{obj} = -46.0$ km s^{-1}, and it appears as a 5 km s^{-1}-wide minimum in the H I emission spectrum (Fig. 4.3). A kinematic distance of 5.7 kpc to G93.6+1.3 is indicated by the velocity of this feature. There is no significant ^{12}CO emission towards this H II region at any velocity. Integrating H I only to −46 km s^{-1} accumulates A_V=3.91±0.46 magnitudes of extinction. From the photometry of the optical emission, the

apparent emission measure is $EM_{H\alpha}$=33.4±9.8 cm^6 pc^{-1}. Integration of 21 cm CGPS radio continuum data over the same area gives the absolute emission measure $EM_{21\ cm}$=439±22 cm^6 pc^{-1}. Thus, the emission-measure decrement to G93.6+1.3 is found to be A_V=3.60±0.33 magnitudes.

A mean value of A_V=3.73 mag is thus reported as the extinction to this new H II region. As well, the method of Chapter 2 calculates a distance of 3.3±0.6 kpc, corresponding to a circular velocity that is +25 km s^{-1} discrepant from its observed velocity.

4.4 The Extinction to SNR 3C434.1

Currently, the only high-energy observations of SNR 3C434.1 exist in the public archive of the ROSAT mission. ROSAT PSPC-B data for G94.0+1.0 were obtained, and analyzed using the PROS software package under IRAF. Smoothed hard band 0.5 keV< kT_e < 2.4 keV images of the remnant were made and compared to CGPS 21 cm and 74 cm images. A total absorbing column density was estimated from a fitted model of the X-ray spectrum of 3C434.1. The value compares very well with that estimated from integration of H I+^{12}CO. I briefly describe the remnant's appearance in X-rays and the spectrum below.

As seen in Figure 4.9, the SNR's radio continuum and hard X-ray morphology correlate very well, with the hard X-ray emission mostly confined to the eastern bright radio shell. East-west surface brightness profiles of emission show strongly peaked hard X-rays in the centre of the eastern radio shell, and the hard X-ray emission falls to background counts at the location of the radio shell's limb in the East. Lower surface brightness X-ray emission in the West correlates with lower brightness radio emission in this region, and the X-rays taper to background counts at a similar rate as radio emission. The remnant appears not to be interacting with anything in this hemisphere, and is probably still freely expanding in the westerly direction inside the very low density interior of its SWB home. The elliptical SWB discussed in Chapter 3 completely encloses the hard X-ray emission as seen in Fig. 4.9.

A very distinct anticorrelation exists between the $H\alpha$ emission identified with 3C434.1 (see Fig. 4.2) and hard X-ray emission. The anticorrelation sug-

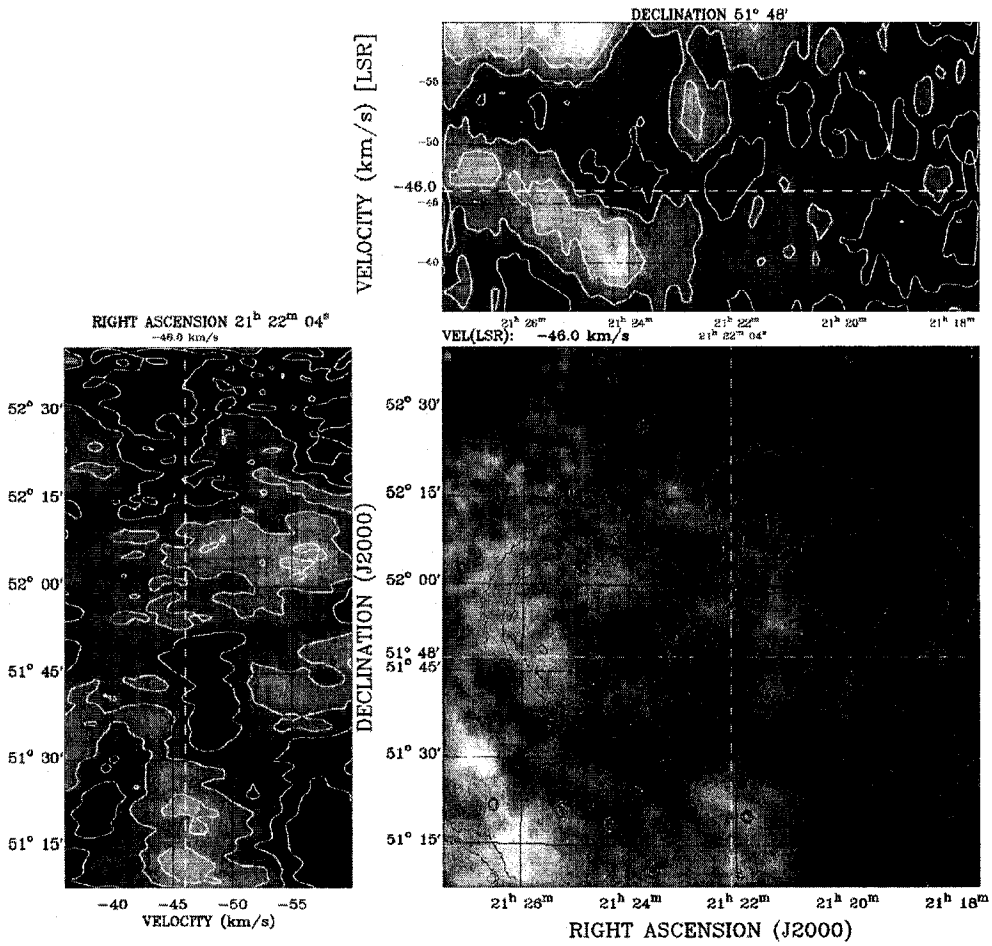

Figure 4.8: Three slices through the H I data cube towards G93.6+1.3. Right panel: an H I shell corresponding to G93.6+1.3 is seen at coordinates $\alpha(2000) = 21^h22^m, \delta(2000) = 51°48'$ with a systemic velocity $v_{obj} = -46$ km s^{-1}. The top panel is a velocity-α slice at the above declination, in which a matching cavity is visible. Left panel: a velocity-δ slice at fixed α shows the same H I cavity.

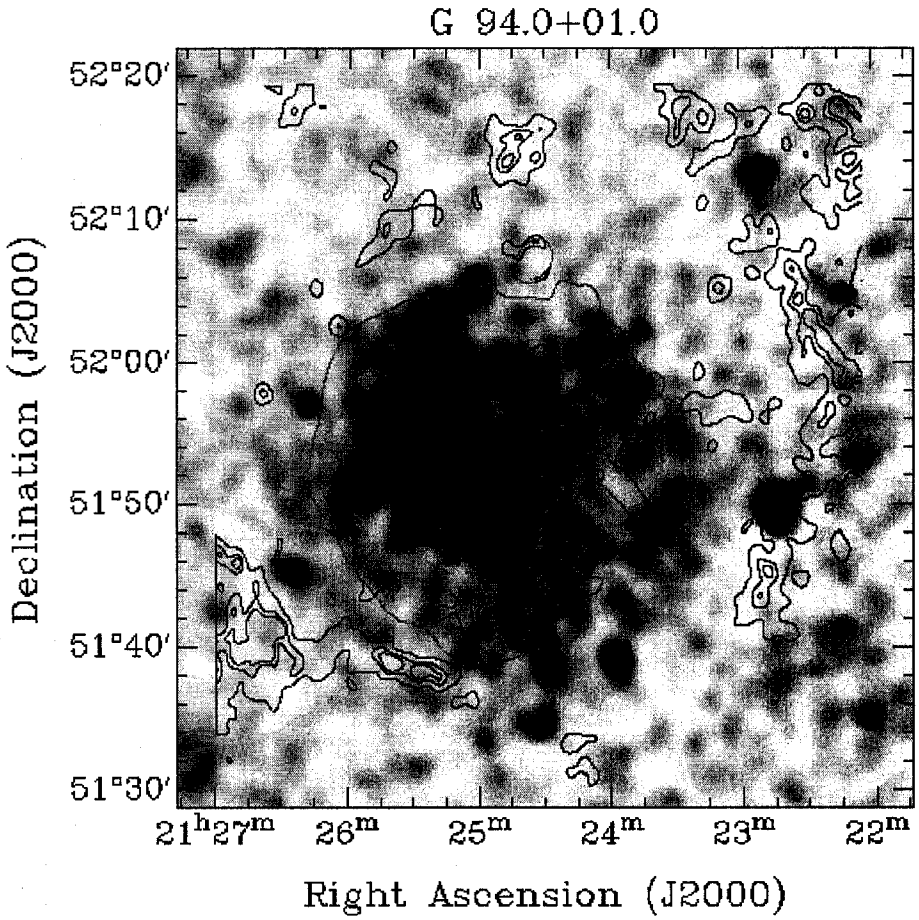

Figure 4.9: The high-energy X-ray appearance (0.5 keV< kT_e < 2.4 keV) of 3C434.1, as observed by the ROSAT satellite. Black is more intense emission in this figure. There is excellent correlation of this emission with the bright eastern half radio shell (21 cm continuum, contoured). The H I shell that surrounds 3C434.1 (c.f. Chapter 2) is shown to completely enclose the X-ray emission.

gests that the $H\alpha$ and X-ray emission originate from different locations and components of the remnant. In a "cloudy" medium (one with sharp density contrasts) this is understandable, as $H\alpha$ should originate with dense clouds that are cooling after having been heated by a secondary shock wave, while X-ray emission marks the location of hot intercloud medium gas ($T_e > 10^6$ K) and tenuous swept-up matter recently heated by the shock.

There is a lack of overall structure in soft X-rays (0.1 keV - 0.5 keV), save for a conspicuous absence of soft X-ray emission within the eastern radio-bright shell. Scattered patches of such emission are seen inside and outside the radio continuum boundary of 3C434.1, but no clear correlation is observed. Very little flux in this band is observed for this remnant, suggesting a large absorbing column and distance.

Finally, there is no observed correlation between any radio and X-ray point sources in this field.

A high-energy-band spectrum (0.5 keV-2.4 keV) was extracted from a circle (radius 10.7′) overlaid on the centre of the X-ray remnant, and a background was determined from an annulus (inner radius 17.8′, width 5′). Six point sources within these regions were excluded. The observed spectrum (see Fig. 4.10) peaks near 1.3 keV. Various models of plasma emission absorbed by smooth and localized components of hydrogen (Galactic and intrinsic absorption) were fitted to this spectrum, with the most formally acceptable fit (reduced χ^2=14/19=0.74) being obtained with an absorbed single temperature plasma model (Raymond & Smith 1977), with line emission from heavy elements similar in abundance to solar values. Table 4.4 provides results of the spectral fit for 3C434.1, and lists some derived astrophysical properties of this SNR. Figure 4.10 shows both the observed and fitted spectra.

Confidence level contours of Galactic N_H and temperature were constructed for the fit and are shown in Figure 4.10. They indicate little variation in absorption column values with varying temperature, with a clear minimum in χ^2. One can thus be confident of the value for Galactic absorption obtained by fitting with this model. The model yields a Galactic column density of N_H=1.51± 0.06× 10^{22} cm^{-2}, very similar to that obtained by direct integration of H I+^{12}CO emission (see below). Using the gas to dust ratio N_H/A_V=1.57±0.1×10^{21} cm^{-2}

Observed Parameters:	
Count rate (s^{-1})	0.18±0.01
Distance (kpc)	5.2±1.1
Radius of emitting region (pc)	16±3
Flux F_x (10^{-12}ergs s^{-1} cm^{-2})	1.5
Fitted Parameters:	
kT_e (keV)	0.48
Galactic N_H(10^{22} cm^{-2})	1.50
Derived Properties	
Normalization $log(\int n_e^2 dV/4\pi r^2$ cm^{-5})	12.3
Volume emission measure (10^{57} cm^{-3})	6.76
RMS electron density n_e (cm^{-3})	0.3
X-ray emitting mass M_x ($M_\odot$)	55
Thermal Energy E_{th} (10^{50} ergs)	1.2
Unabsorbed flux F_{x0} (10^{-12} ergs s^{-1} cm^{-2})	47
X-ray Luminosity $L_x = 4\pi r^2 F_{x0}$ ($L_\odot$)	41.3

Table 4.4: Observed, fitted and derived results of the single temperature plasma model with absorption fitted to the PSPC X-ray spectrum (in the range 0.5 keV to 2.4 keV) of 3C434.1. The quality of this fit is χ^2=14/19 (reduced χ^2 with 19 degrees of freedom). The PSPC count rate is background-subtracted. The log of the normalization is the volume emission measure over the area of a sphere of radius r, the distance to the source (r=1.6×10^{22} cm). The fitted value for kT_e indicates a plasma temperature of T_e =5.4×10^6 K. A volume filling factor of f =0.15, estimated in the text, is used. Errors are estimated from the range of acceptable model fits obtained with varying metal abundance Z (percentage of Solar value).

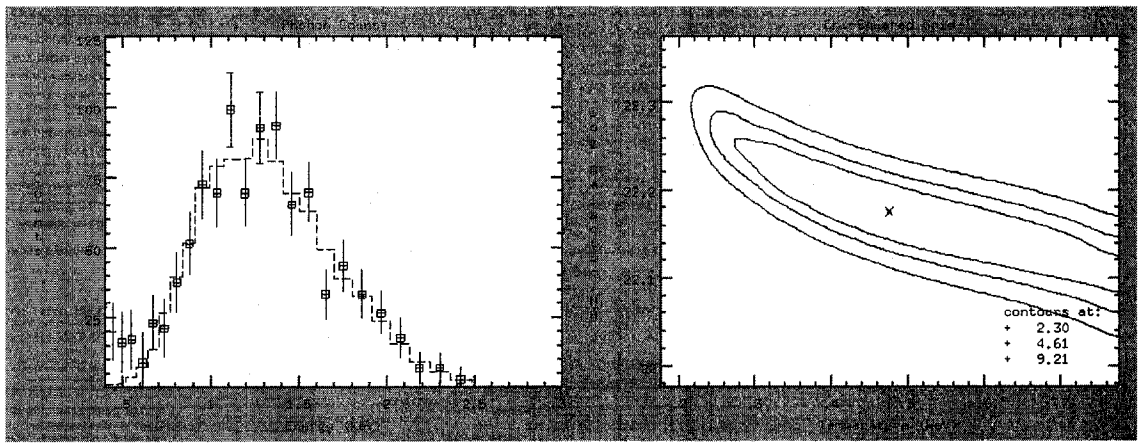

Figure 4.10: (left panel) The observed and model spectra of the X-ray emitting plasma associated with SNR 3C434.1. (right panel) Two dimensional χ^2 contour plot (Galactic N_H versus temperature), demonstrating the narrow constraint on the fitted absorption parameter for widely varying values of temperature. Confidence (contour) levels are 68%, 90%, and 99%.

mag^{-1}, an optical extinction of A_V=9.6± 0.8 magnitudes is found for the sight-line to the X-ray gas in the SNR.

The excellent fit of the Raymond-Smith model indicates the X-ray emission is predominantly thermal in origin (at least in this easterly region of the SNR), and on average the plasma that comprises the SNR seen in this area is probably in thermal equilibrium. The X-ray emitting material from this SNR is likely evolving in an adiabatic way, the shock having been slowed by its encounter with intrabubble matter, probably that involved with the inside edge of the stellar wind bubble.

Integration of H I and ^{12}CO data towards $\ell = 94°, b = 1°$ yields a column density of N_H=1.56±10%×10^{22} cm^{-2}, similar to that obtained by fitting the absorbed Raymond-Smith thermal emission model above. Thus, an optical extinction of A_V=9.9± 1.2 magnitudes is found for the sight-line to the SNR. Combining the X-ray results with the H I+CO results, a mean extinction of A_V=9.7± 1.0 magnitudes for 3C434.1 is estimated.

A distance of 5.2±1.1 kpc is also found from Chapter 3. One can thus estimate that along this LOS a mean extinction rate A_V/r ~1.9 mag kpc^{-1} is applica-

ble, not far from the value of ~1.6 mag kpc^{-1} suggested by Binney & Merrifield (1998). As well, a typical physical size is thus estimated for this SNR (radius≃24 pc). I derive other new physical parameters for 3C434.1 from X-ray and other data in a future publication (see Table 4.4, from Foster & Routledge, in preparation).

4.5 Discussion and Conclusions

I offer a "big picture" summary of the ℓ =93° area, and comment on possibilities raised by the new distances and extinctions established for the four objects therein.

It is instructive to refer to the Two-Arm Spiral Shock (TASS) model (Roberts 1972) for the Perseus spiral arm, with R_0=8 kpc. In the direction of 94°, the TASS pattern is located roughly 3.5 kpc from the Sun (a spatial uncertainty of order ± 400 pc or greater is assigned by Roberts), and the shock stretches for 0.5 kpc along the LOS. Roberts suggests that most luminous optical objects that reside in the Arm (e.g. H II regions) should be situated at or behind the shock, after having been triggered into existence by its effect.

Figure 4.11 shows the placement of the objects in this study with respect to a model spiral arm, and to the TASS. It is readily noticable in this grand picture that most objects indeed lie within or behind the shock, the result predicted by Roberts. If the ℓ = 93° objects originally formed from material compressed by the shock, then the age of the stellar wind bubble surrounding 3C434.1 (2.6×10^6 yr, see Chapter 3) provides an upper limit estimate for their ages.

G93.6+1.3 is the youngest H II region of the lot. Our distance of 3.3± 0.6 kpc for G93.6+1.3 easily places it within the influence of the Perseus Arm shock. Further, the observed radial velocity of the H I cavity associated with G93.6+1.3 (v_{obj} = −46 km s^{-1}) places it atop the shock ridge predicted by Roberts' model of H I distribution towards ℓ =93°. The observed velocity excess of 25 km s^{-1} for G93.6+1.3 is well explained by this model. Exciting stars within G93.6+1.3 may have recently been triggered into existence by passage through the shock. Clearly, the evidence indicates that G93.6+1.3 is a relatively young H II region, foreground to the other objects.

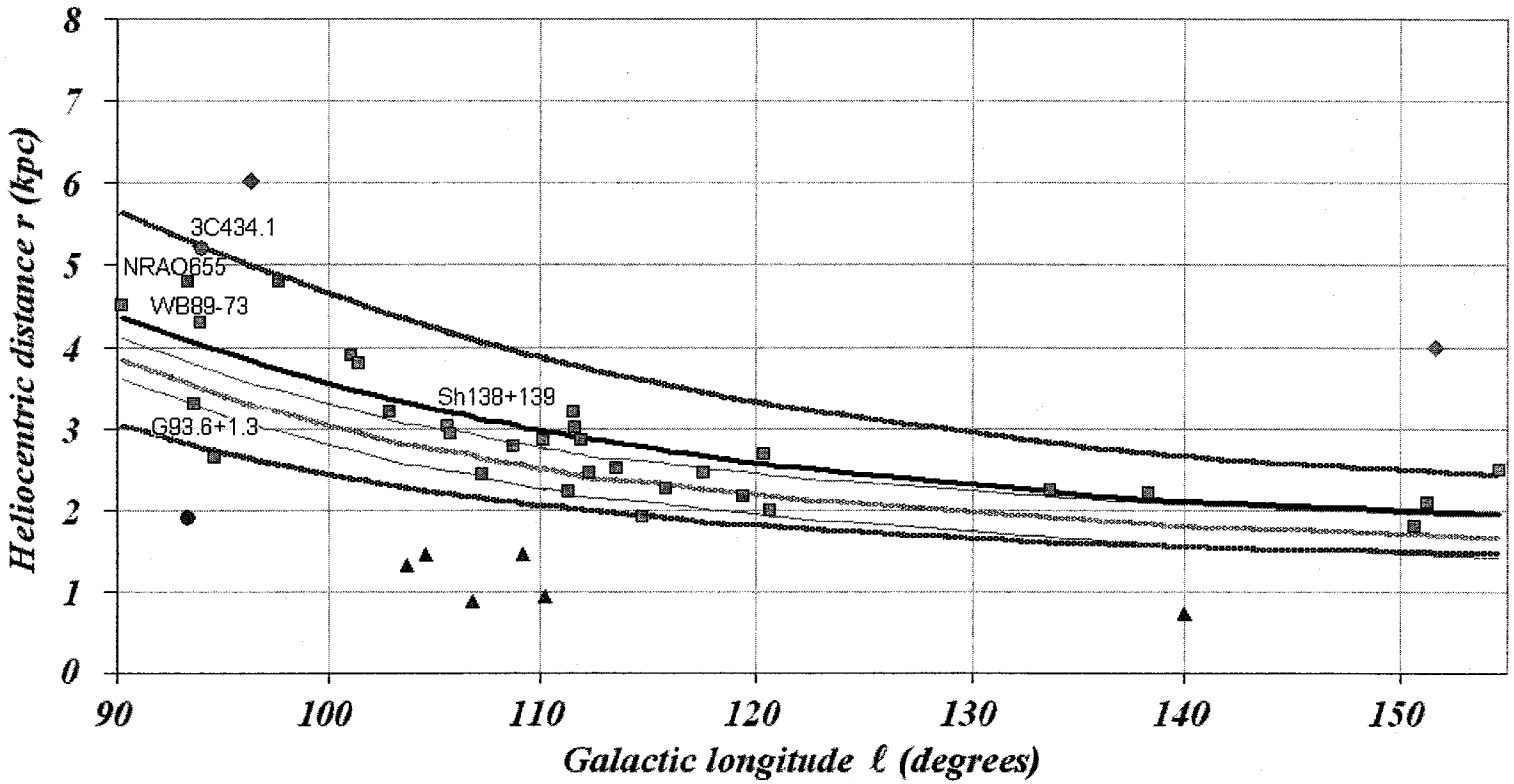

Figure 4.11: A spatial map of the second quadrant, constructed by the author's method. The Perseus Spiral Arm is easily traced by the distribution of 29 optical H II regions (light squares) and 1 SNR (circle). Six Local Arm H II regions are marked as triangles and 1 local SNR as a circle. Two possible Outer Arm H II regions are shown as diamonds. The objects in this study are labelled. A logarithmic model of a spiral arm (bold solid line) has been fitted to these nebulae, and a pitch angle near i=10° is found. The line of sight extent (2σ half-width) of the model arm is delimited by the thick dark hatched curves. The model is constructed from the centre and width of the arm (R(ϕ_0)=9.4 kpc, w_{arm}=0.5 kpc) as calculated towards ℓ_0=105.8° by the author's method. Note the large apparent width of the arm near to the low longitude end: this is due to the line of sight viewing the arm longitudinally. The Spiral Shock model of Roberts (1972, Fig. 2 in that paper) has been overlaid for comparison (thick opaque grey curve) with the 0.5 kpc extent assigned by Roberts delimited by thin grey curves.

The two H II regions NRAO 655 and WB89-73 are found to be at similar distances from the Sun (see Tab. 4.5), and well behind the shock. As calculated, the radial velocity excesses of the objects are similar, a reasonable finding since each was probably similarly affected by the spiral shock. $H\alpha$ images display interesting features of WB89-73: an optical "tail" of emission pointing away from NRAO 655, and faint radio continuum extension pointing towards NRAO 655. The optical image of WB89-73 is reminiscent of a comet seen with a highly foreshortened tail. It is possible that NRAO 655's "champagne" outflow is shaping this nebula, and this flow is partly along the LOS. I suggest the possibility of interaction between these two H II regions.

I also suggest that 3C434.1 and NRAO 655 are quite probably related as well. The extinction toward the SNR is quite similar to that toward NRAO 655 (see Tab. 4.5). The calculated non-circular velocities are essentially identical, indicating that both objects have been similarly displaced from flat circular rotation (if such a rotation model is accepted). The 21 cm continuum image shows emission from material "erupting" from each, seemingly escaping into a common area between them. Ionized gas from NRAO 655 is likely undergoing a "champagne flow" into this lower density midregion (Foster & Routledge 2001). Although our distance for 3C434.1 of 5.2±1.1 kpc establishes the possibility that this SNR is evolving into the same area as NRAO 655 (distance 4.8±0.8 kpc), the SNR is "enclosed" within a stellar wind bubble formed by its progenitor and a companion (O4 type stars). It is possible that the stars of this SWB and the exciting stars within H II region NRAO 655 are related as part of an extended OB association, and formed at similar times. The two O4-type stars (see Foster et al. 2003) that formed in the eastern side of this cluster subsequently excavated a cavity in neutral hydrogen, while stars that formed in the western side are continuing to be responsible for the ionization of NRAO 655.

Tab. 4.5 summarizes the extinctions, distances and velocity excesses found in this work for each of the four objects studied. Objects in the ℓ =93° region are likely interacting with the Perseus Arm spiral shock, exhibiting velocity shifts of order 20-30 km s^{-1} from flat circular rotation. I speculate NRAO 655 and 3C434.1 are related by the same cluster of stars, with 3C434.1 evolving into a medium of reduced density (swept out by its progenitor and another star), and

Measure	A_V (EM_λ [X-ray])	A_V (N_H)	Kinematic (kpc)	F&R (kpc)	v_{nc} (km s^{-1})
WB89-73	10.1±0.4	10.5±1.2	7.0	4.3 ±0.6	+28
3C434.1	[9.6±0.8]	9.9±1.2	9.2	5.2±1.1	+40
NRAO 655	12.3±0.3	12.4±1.5	8.3	4.8±0.8	+36
G93.6+1.3	3.8±0.3	4.3±0.5	5.7	3.3±0.6	+25

Table 4.5: Extinctions (in magnitudes), distances and non-circular velocities v_{nc} reported in this chapter for nebulae in the Galactic plane region near ℓ=93°, b=1°. Column 2 lists extinctions derived via emission measure ratios $EM_{21\ cm}/EM_{H\alpha}$ (Eqn. 4.6) or from a model of the absorbed X-ray spectrum. These values represent direct calculations of the foreground dust column. Column 3 shows extinctions derived from N_H=H I+^{12}CO (Eqn. 4.1 and 4.2) and the gas-to-dust ratio of Vuong et al. (2003). The latter are very comparable to the former values, suggesting that the dust column is well represented by the hydrogen column. All errors are standard errors (except in distance, which are limit errors).

NRAO 655 into a power-law density environment outside its parent molecular cloud. The ages of these objects are similar at ~3 Myr. I also conclude that the newly discovered H II region G93.6+1.3 is the most recently formed, and relatively nearby with respect to the other objects.

Table 4.5 also shows the comparable values of extinctions, derived from the different methods in this Chapter. The very important conclusion one draws from this is that in this direction, the LOS distribution of dust is well traced by total hydrogen column density N_H, and the gas-to-dust ratio of Vuong et al. (2003). The methods used in this chapter, and the availability of high quality H I and ^{12}CO line data (from surveys like the CGPS) can contribute to fruitful new studies of the distribution of optically-absorbing material in the Galactic plane.

Bibliography

[1] Binney, J., & Merrifield, M. 1998, Galactic Astronomy, (New Jersey: Princeton University Press)

[2] Bohlin, R., Savage, B., & Drake, J. 1978, ApJ, 224, 132

[3] Brand, P. W. J. L., Coulson, I. M., & Zealy, W. J. 1981, MNRAS, 195, 353

[4] Dame, T. M., Hartmann, D., & Thaddeus, P. 2001, ApJ, 547, 792

[5] Deharveng, L., Zavagno, A., Nadeau, D., Caplan, J., & Petit, M. 1999, A&A, 344, 943

[6] Elmegreen, D. M. 1998, Galaxies and Galactic Structure, (New Jersey: Prentice-Hall, Inc.)

[7] Feibelman, W. A. 1982, AJ, 87, 555

[8] Fich, M., Blitz, L., & Stark, A. A. 1989, ApJ, 342, 272

[9] Foster, T. Routledge, D., & Kothes R. 2003, A&A, accepted

[10] Foster, T. & Routledge, D. 2001, A&A, 367, 635

[11] Foster, T. 2000, M.Sc. thesis, University of Alberta

[12] Foster, T., Hube, D., Couch, J., Martin, B., Routledge, D., & Vaneldik, J. F. 1999, in ASP Conf. Ser. 189, Precision CCD Photometry, ed. E. R. Phillips, D. L. Crawford, & R. A. Tucker (San Francisco: ASP), 111

[13] Georgelin, Y. M., & Georgelin, Y. P. 1976, A&A, 49, 57

[14] Gibson, S. J., Taylor, A. R., Higgs, L. A., & Dewdney, P. E. 2000, ApJ, 540, 851

[15] Gorenstein, P. 1975, ApJ, 198, 95

[16] Goss, W. M., Mantovani, F., Salter, C. J., Tomasi, P., & Velusamy, T. 1984, A&A, 138, 469

[17] Kerton, Charles. 2003, private communication

[18] Neckel, T., & Chini, R. 1981, A&AS, 45, 451

[19] Osterbrock, D. 1974, Astrophysics of Gaseous Nebulae, (San Francisco: W.H. Freeman and Company)

[20] Peeters, E., Martín-Hernández, N. L., Damour, F., Cox, P., Roelfsema, P. R., Baluteau, J.-P., Tielens, A. G. G. M., Churchwell, E., Kessler, M. F., Mathis, J. S., Morisset, C., & Schaerer, D. 2002, A&A, 381, 571

[21] Predehl, P., & Schmitt, J.H.M.M. 1995, A&A, 293, 889

[22] Raymond, J. C., & Smith, B.W. 1977, ApJS, 35, 419

[23] Reich, W., Fuerst, E., Haslam, C. G. T., Steffen, P., & Reif, K. 1984, A&AS, 58, 197

[24] Reynolds, R. J. 1988, ApJ, 333, 341

[25] Roberts, W. 1972, ApJ, 173, 259

[26] Rohlfs, K., & Wilson, T.L. 1996, Tools of Radio Astronomy, (2d ed.; Berlin: Springer-Verlag)

[27] Russeil, D. 2003, A&A, 397, 133

[28] Ryter, C., Cesarky, C. J., & Audouze, J. 1975, ApJ, 198, 103

[29] Savage, B. D., & Mathis, J. S. 1979, ARA&A, 17, 73

[30] Taylor, A. R., Dewdney, P. E., Landecker, T. L., Martin, P. G., Brunt, C. M., Dougherty, S. M., Durand, D., Gibson, S. J., Gray, A. D., Higgs, L. A., Kerton, C. R., Knee, L. B. G., Kothes, R., Peracaula, M., Purton, C. R., Uyanıker, B., Wallace, B. J., & Willis, A. G. 2002, AJ, 125, 3145

[31] Whitford, A. E. 1958, AJ, 63, 201

[32] Wouterloot, J. G. A. & Brand, J. 1989, A&AS, 80, 149

[33] Vuong, M. H., Montmerle, T., Grosso, N., Feigelson, E. D., Verstraete, L., & Ozawa, H. 2003, A&A, 408, 581

Chapter 5

The Dynamics and Rotation of the Outer Galactic Disk

Foreword

Upon looking at Figure 2.1 (see Chapter 2), it is natural to be suspiscious of the flat circular Galactic rotation model. Alone, this canonical rotation curve fails to account for the large radial velocities of relatively nearby H II regions throughout the second quadrant of the Galaxy ($90° \leq \ell \leq 180°$). The velocities of these nebulae are blueshifted beyond that expected from a ± 8 km s^{-1} velocity dispersion, creating an apparent disparity between the radio and the optical spiral arm as traced by these objects.

A non-axisymmetric disturbance (such as a Galactic shock wave) can account for some of this discrepancy. However, in that model the velocity field is expected to rejoin circular Galactic rotation beyond the spiral density wave. In this case, the interarm regions and the far outer Galactic disk should be unaffected by the shock, which is expected to give rise to Spiral Arm objects only. Figure 2.1 shows no sign of this behaviour: rather, one might conclude that the chasm is ever-widening. What is affecting H II regions in the distant outer Galaxy?

The contents of this thesis chapter show a new way of determining the *velocity field* for a given direction in the second quadrant. This is a natural product of the fitting technique in Chapter 2: the derivation of a smooth relationship between heliocentric distances and line of sight velocities for a given direction, rather than a single distance for a given radial velocity. Some of this chapter appears published in the pages of the ASP Conference Series "Milky Way Surveys: The Structure and Evolution of Our Galaxy" (eds. Clemens & Brainerd 2003).

It should be noted that the derivation of velocity fields only relies on one basic assumption: that there exists on a large scale a smooth relationship between v and r along directions in the outer Galaxy. However, translating velocity fields into rotation curves imposes one more implicit (and precarious) assumption: that an object's line of sight velocity arises entirely from circular motions about the Galactic centre. In pronouncing the new rotation model calculated in this section, I tread carefully, and offer much discussion on the assumptions, and inherent accuracy of the method. This work represents a snapshot in time of a very large and very important ongoing project to determine the dynamics that

govern in this part of the Galaxy.

Abstract

Models of the smooth large-scale radial distribution of the column depth of H I in the thin disk are used to found a new technique of mapping the velocity field of the Outer Galaxy in the second quadrant. The results show common features across this quadrant: a) locally ($r \leq 2$ kpc), Galactic H I obeys a near-flat rotation law (with R_0=7.9 kpc, θ_0=214 km s^{-1}, and Oort constants A=13.2 and B=−13.9 km s^{-1} kpc^{-1}), b) beyond r=2 kpc, velocities of H I in the plane ($|b| \leq 5°$) show pronounced deviation from velocity fields predicted by flat circular rotation, and c) towards some relatively high latitudes ($|b| > 5°$), the Galactic H I exhibits "normal" behaviour, with observed velocities congruent with those predicted by a gently declining circular rotation curve. It is concluded from these observations that the Perseus Arm spiral shock is visible in our velocity fields, but is only partially responsible. Combined with the nearby shock, an underlying gently-declining rotation curve beyond $r \geq 2$ kpc and streaming motions along the Perseus Spiral Arm would explain the observations. We also discuss an apparent "rolling" motion present in the Perseus Spiral Arm.

5.1 Introduction

Neutral hydrogen (H I) seen in emission is omnipresent in the Galactic plane, and is well known as a component that traces the smooth structure of the Galaxy's disk. Line of sight (LOS) H I velocities are commonly used in determinations of the outer Galaxy rotation curve (by comparison with independently known distances, usually to H II regions), or as distance indicators (with foreknowledge of the Galactic rotation curve). A seldom-discussed yet fundamental assumption in the above applications is that the observed velocity derives entirely from an object's circular rotational velocity about the Galactic centre. This is not necessarily true, as non-circular motions in H I spectra can affect the projected placement of H I features (e.g. streaming motions and shocks formed by spiral

density waves).

The dangers in the assumption of pure circular motion are demonstrated in published photometric distances to 30 H II regions (catalogued by Fich, Blitz & Stark 1989) which are glaringly inconsistent with those calculated kinematically with the flat rotation curve predicted by their ^{12}CO velocities. Obviously, a different approach to determining the properties and dynamics of the outer H I disk is needed, preferably one with a less-impacting assumption.

One such new method has been developed, based on a model of the cumulative H I column density with Galactocentric radius (Foster & Routledge 2003, hereafter F&R). Midplane H I data from the Canadian Galactic Plane Survey (CGPS; Taylor et al. 2003) is used with the model to determine the outer Galaxy's dynamical behaviour in the second quadrant region $90° \leq \ell \leq 140°$. We present an exploration of both the method and the preliminary results.

5.2 The Technique of Finding Velocity Fields

The method of Galactic H I study proposed by F&R is shown in Figure 5.1. An input H I emission spectrum $T_b(v)$ is obtained towards direction (ℓ, b). To use the method as a distance tool requires a third input (the object's LOS velocity). The integrated column density to the Galactic edge $N_{HI}(r = \infty)$ in the direction of interest is obtained from the observed H I spectrum. A model of cumulative column density with distance:

$$N_{HI}(r, \ell, b) = \int_0^r n(r', \ell, b) dr' \tag{5.1}$$

is made to terminate at this value, where $n(r, \ell, b)$ is the model of the number density of hydrogen nuclei encountered versus LOS distance (see Equation 2.11). This model has both axisymmetric features (exponentially-decaying density with R and height z), and non-axisymmetric components (the disk's warp, and spiral arms). The model $N_{HI}(r, \ell, b)$ (Eqn. 5.1) is transformed using a trial velocity field $v(r)$. The function $v(r)$ maps the column depth model $N_{HI}(r, \ell, b)$ into velocity space ($N_{HI}(v(r), \ell, b)$), allowing a direct comparison. Parameters of both functions are varied until the overall form of $N_{HI}(v)$ observed in the H I

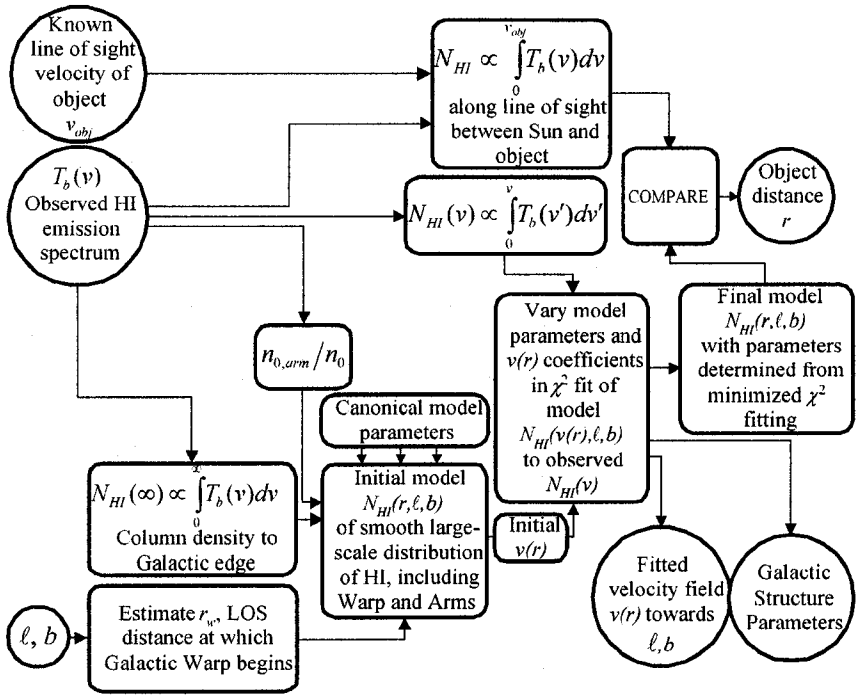

Figure 5.1: Flowchart of the method of Galactic H I study proposed by Foster & Routledge (2003). Circles represent inputs and outputs of the method, with steps represented in boxes. This chapter deals with the fitted velocity field $v(r)$ towards the direction of interest ℓ, b.

data is well fitted in a χ^2-minimization process. This fitting yields the LOS velocity field $v(r)$, and Galactic structure parameters that best match the observed H I (bottom-right circles in Figure 5.1).

The accuracy of the method's distance output has been demonstrated towards 30 H II regions with known photometric distances and radial velocities (see Chapter 2). Applying this technique does not assume that LOS velocities arise solely from circular rotation, but rather that on a large scale, the observed LOS velocity (for H I in emission) is increasingly negative with distance. Circular motions would exhibit this behavior, but they are only one possible contributor to an object's observed velocity. On a large scale, for H I in emission and for which circular motions are a substantial fraction of the observed LOS velocity, the assumption that distance is monotonic with velocity is fundamentally true.

Before we proceed, we add two complementary refinements to the density

distribution $n(r, \ell, b)$. First, it is appropriate to introduce a natural dispersion to the path length per unit velocity interval, such that H I present at a *range* of distances is found at a single radial velocity v. We employ a normalized Gaussian of width σ_r and convolve it with $n(r, \ell, b)$:

$$n'(r, \ell, b) = \frac{1}{\sqrt{2\pi}\sigma_r} \int_0^\infty n(r', \ell, b) exp\left(-(r - r')^2/2\sigma_r^2\right) dr' \tag{5.2}$$

and estimate the dispersion using:

$$\sigma_r = |\partial r/\partial v_{flat}|_{r=0kpc}\, \sigma_v \tag{5.3}$$

where σ_v is estimated from the half-width of the H I profile at positive velocities (forbidden in circular rotation), typically $3 \leq \sigma_v \leq 9$ km s^{-1}. The path length per unit velocity interval near the Sun, predicted by a canonical flat rotation curve (Eqn. 5.8 with R_0=8 kpc, $\theta_0 = 220$ km s^{-1}) is $|\partial r/\partial v_{flat}|_{r=0kpc}$=$2R_0/\theta_0 sin2\ell \sim 0.1$ kpc/km s^{-1} near ℓ =110°.

Secondly, we add to $n(r, \ell, b)$ a component that models the *local* density distribution, $n_{local}(r, \ell, b)$. It is known that the Sun resides within a less-dense region (the "local bubble") that itself is within a minor spiral feature (the Local Arm, or "spur"). A Gaussian velocity profile for local H I is observed in almost all H I spectra for $0 > v > -15$ km s^{-1}, and peaks at negative velocity, crudely suggesting that a concentration of H I lay near or just in front of the Sun ($R_l \geq R_0$, where R_l is the galactocentric distance to the H I density peak $n_{local\ arm}$ associated with the local arm). A Gaussian for n_{local} thus seems appropriate:

$$n_{local}(r, \ell, b) = n_{local\ arm} exp\left(-(R - R_l)^2/w_{local}^2\right) \tag{5.4}$$

where w_{local} is the width of this feature. However, it is important to note that the Gaussian distribution is rather indistinguishable from a *uniform* density distribution for the local H I (see Fig. 5.2), due to the natural dispersion of the velocity-distance relation. Thus, it is not possible to rule in favour of either distribution for the local arm, although it seems unphysical that an abrupt drop in density should occur near r=0.8 kpc as in the uniform model. With the above uncertainty in mind, we retain the Gaussian model component (Eqn. 5.4) for H I

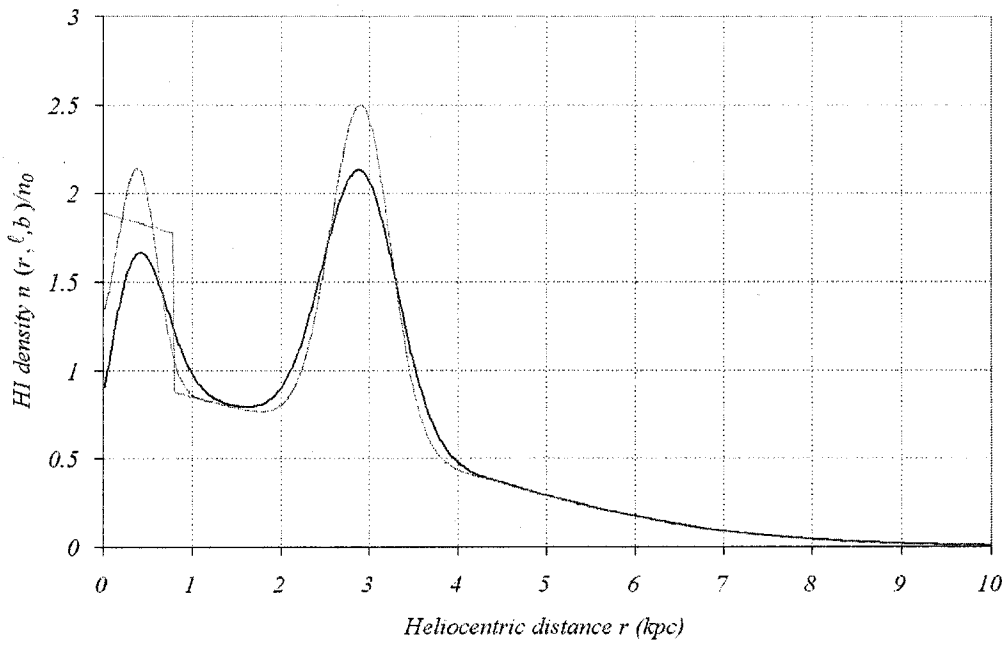

Figure 5.2: The model density profile $n(r, \ell, b)$ towards $\ell = 112°, b = 1°$, before (thin lines) and after (thick black line) the convolution in Eqn. 5.2. Due to this convolution, a uniform density distribution for the local H I ($r \leq 0.8$ kpc) produces a spectrum that is indistinct from that of a Gaussian density profile (of the same total area). In this direction, the local dispersion is $\sigma_r \sim 0.3$ kpc.

near to the Sun.

A typical model density profile with these refinements is shown in Figure 5.2. The convolution mildly extends the width of the spiral arm profiles, but other changes are insignificant.

For an initial look at the field, we choose a cubic function of the form $v(r) = ar^3 + br^2 + cr + d$ to represent a simple smooth velocity field. This function contains four free parameters. Presupposing circular motions would mean the parameter d should be constrained to 0 km s^{-1}. However, since we broaden the local density of H I by σ_r, d may be expected to be positive. We constrain d to be less than or equal to the velocity at which H I is first measurable (typically $<\sim$10 km s^{-1}), but give H I at positive velocities zero-weight in the fit. In the models of $n(r)$, five additional parameters are varied in the minimization (h_R,

h_0, h', R_m, and w_{arm}). Depending on the direction (ℓ, b), those channels with velocity $0 \geq v \geq v_1$ km s^{-1} in the H I spectrum are given unity weighting (v_1 is the *lower* velocity limit where $dN_{HI}(r, \ell, b)/dr$ becomes negligibly small). The lower velocity limit v_1 varies from direction to direction (see Table 5.1). With channels at $v \geq 0$ km s^{-1} given zero weight, we typically have $\nu \geq 120$ degrees of freedom available.

The cubic representation of $v(r)$ is actually the smooth function that best fits the *predicted* velocity-distance mapping. This is the observed relationship between v and r, values for which are extracted from a comparison of common column densities calculated by the model and observed in the data:

$$N_H(r, \ell, b) = N_H(v, \ell, b) \tag{5.5}$$

where $N_{HI}(v, \ell, b)$ is from the observed H I column density-velocity diagram. The initial assumption of a monotonic relationship between v and r forces this observed relationship to be continuous. Figure 5.3 shows two predicted fields with cubic representations from the fitting process.

5.3 Goodness-of-fit and Error Estimations

In Chapter 2, one judged the distance uncertainty based on the uncertainty in an object's radial velocity. This was given by the typical width of the ^{12}CO signal ($\sigma_v \sim 2.4$ km s^{-1}, see Chapter 2) associated with each H II region. However, ^{12}CO is much cooler than H I seen in emission, and thus 2.4 km s^{-1} is likely low with respect to the velocity dispersion associated with warm H I. Such H I has an upper limit velocity uncertainty of $\sigma_v \leq 8.8$ km s^{-1} (Kulkarni & Heiles 1988), derived for the warm neutral medium component of the ISM. To estimate the velocity uncertainty for statistical purposes, we use the *local* value of the velocity dispersion from the half-width of the H I profile at forbidden (positive) velocities.

The probability that the observed (minimized) value of chi-squared will ex-

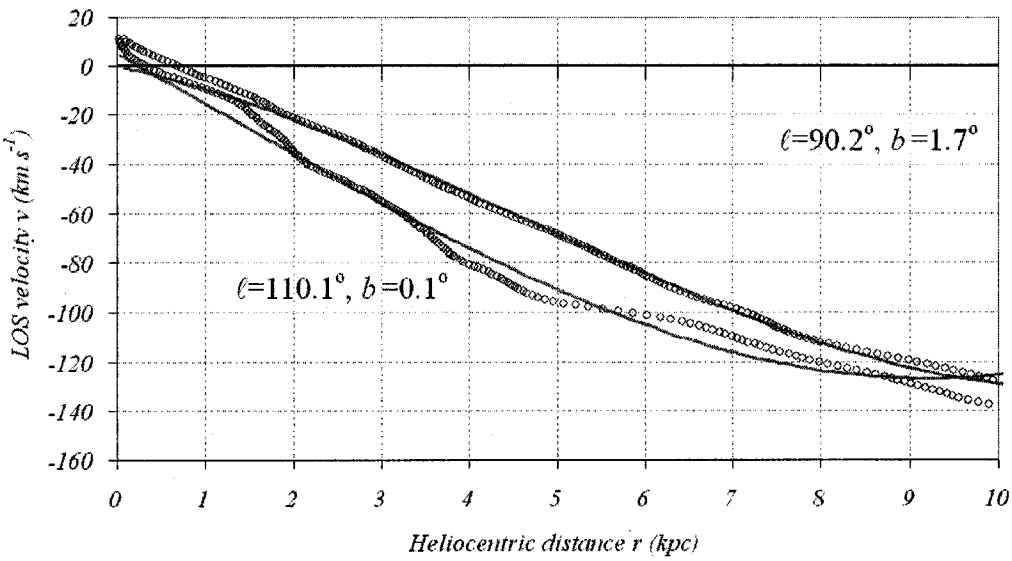

Figure 5.3: Predicted velocity fields (open symbols) and fitted velocity fields (smooth curves) from two directions in the Galactic plane. The smooth $v(r)$ curves are cubic fits to the directly predicted fields.

ceed a particular value χ^2 by chance alone is evaluated by:

$$Q(\frac{1}{2}\nu, \frac{1}{2}\chi^2) = \frac{\Gamma(\frac{1}{2}\nu, \frac{1}{2}\chi^2)}{\Gamma(\frac{1}{2}\nu)} \tag{5.6}$$

where ν is the number of degrees of freedom, which is the number of velocity channels used in the fit (N) minus the number of model parameters allowed to vary. Q is a quantitative measure for the goodness-of-fit of the model (see Press, Teukolsky, Vetterling & Flannery 1996 for discussion), and assumes the velocity errors σ_v are normally distributed, and that the model is correct. It is the probability that the apparent discrepancy between model and observation are chance fluctuations. Perhaps easier to understand, $1 - Q$ is the probability that we would obtain a lower χ^2 value (a *better fit*) with this "correct" model. If $1 - Q \ll 1$, we can pronounce our fit as reasonable.

Table 5.1 shows the directions (ℓ, b) used in the following sections for demonstration and examination of outer Galaxy dynamics. All fits were performed

with a cubic function for $v(r)$ (Sec. 5.2). One can see that the calculated probability Q is unreasonable in many cases, suggesting that either the fit is unusually good/bad or the velocity uncertainties (associated with the fit) from $\sigma_v,\ v \geq 0$ are over/under-estimated. Where the half-width of H I at forbidden velocities gives unreasonable estimates for σ_v, Q may be too near to 1 for a less-than-perfect fit, or too near to 0 for an otherwise excellent fit. The value of Q as a quantitative benchmark should therefore be considered marginal when using $\sigma_v,\ v \geq 0$.

Although the exact magnitude of the normally distributed errors in velocity remain unknown along these lines of sight (making Q not completely trustworthy), we can estimate the root mean square value of σ_v by minimizing χ^2 in the usual way and computing:

$$\sigma_{rms}^2 = \sum_{i=1}^{N} \left(v_i - v(r)\right)^2 / \nu \tag{5.7}$$

Again assuming the model is correct, σ_{rms} gives the mean difference in velocity between the fitted model $N_{HI}(v(r), \ell, b)$ and observed $N_{HI}(v, \ell, b)$. Perhaps the best quantitative judgement of the goodness-of-fit is gleaned from σ_{rms} calculated with Eqn. 5.7. If this value is less than or near the typical velocity dispersion ascribed to H I (e.g. Mebold 1972), then it can be concluded that the fit is reasonable. One can see in Table 5.1 that this is true of all directions, and that velocity errors due to an imperfect fit are a small fraction of σ_v, the natural velocity dispersion of interstellar H I gas.

The bulk of the uncertainty introduced to each velocity field descends from uncertainties in the distances calculated from the model $N_{HI}(r, \ell, b)$. Errors in the distance found to each velocity along a given line of sight will cause the derived velocity fields to exhibit some variance. To estimate distance errors, a $\pm$20% variance is introduced to the following model parameters: h_R, h_0, h', R_m, w_{arm}, and r_w. Figure 5.4 shows the velocity fields in the current study flanked by curves that demonstrate the range these uncertainties introduce.

The $\pm$20% allowance is perhaps overly generous, since it is found that the fitted model $N_{HI}(r, \ell, b)$ parameter values do not differ from each other by more

Direction ℓ, b (°)	Limit v_1 ($0 \leq v \leq v_1$)	σ_v, $v \geq 0$ (km s^{-1})	χ^2/ν	Q	σ_{rms} (km s^{-1})
90.23, 1.72	−136.7	9.3	11/156	1.00	2.4
93.3, 6.9	−140.7	6.0	9/85	1.00	1.4
103.72, 2.18	−136.7	5.1	69/156	1.00	3.4
105.77, −0.15	−153.2	4.3	53/176	1.00	2.4
107.0, 5.4	−135.0	5.1	23/154	1.00	2.0
110.11, 0.05	−135.0	3.5	287/154	0.00	4.7
111.89, 0.88	−135.0	3.5	56/154	1.00	2.1
113.52, −0.57	−121.0	4.3	14/137	1.00	1.4
115.79, −1.65	−121.0	5.1	25/137	1.00	2.2
138.3, 1.56	−101.2	5.0	90/113	0.94	4.7

Table 5.1: A broad selection of ten lines-of-sight, mostly from the CGPS I region (the exception is $\ell = 93.3°$, $b = 6.9°$), chosen to demonstrate velocity fields from a large range of ℓ & b. Estimates of the velocity dispersion and goodness-of-fit are shown. Where the half-width of the H I profile for $v \geq 0$ is used, the values of χ^2/ν and Q (Eqn. 5.6) are misleading. σ_{rms} is from Eqn. 5.7, and provides a better quantitative basis for judging the goodness-of-fit.

than $\sim \pm 10$ to 15%, across the 50° longitude range (see Table 5.2). Further, values for these parameters agree extremely well with recent determinations by Wouterloot et al. (1990), who conclude for H I in the warped midplane a radial scale length h_R =2.5 kpc, a scale height near the Sun of h_0 =200 pc, and a rate of increase of h_0 as h'=36 pc kpc^{-1}. These values are very similar to the mean values found by the author towards ten Galactic Plane locations (see Table 5.2), and are further supported by similar values from other authors (e.g. Diplas & Savage 1991, and Knapp et al. 1978). Finally, with the exception of $\ell = 93.3°$, each direction in Table 5.2 is towards an H II region with a known spectrophotometric distance (see Tab. 2.2). All optical distances are predicted by the velocity fields to within 10%, an indication that the fields are probably at least this accurate.

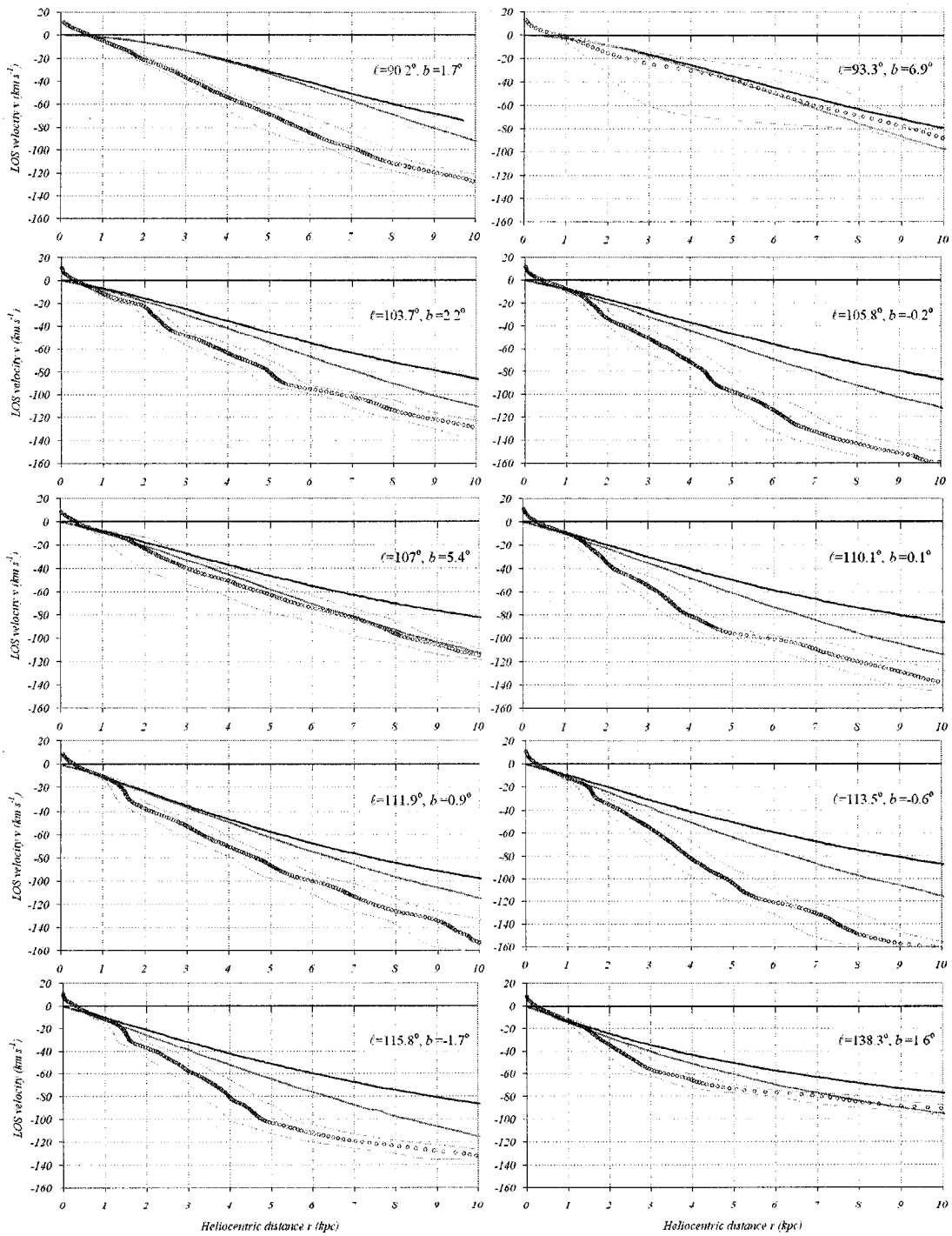

Figure 5.4: The $v(r)$ fields towards the directions in Table 5.1. Overlaid with our observed fields (open circles) are those calculated from a flat rotation curve for the outer Galaxy (Eqn. 5.8, thick black curve) with R_0=7.9 kpc and θ_0 = 200 km s^{-1} (Merrifield 1992), and a Schmidt model (thick grey curve, Schmidt 1965) with R_0=10 kpc and θ_0 = 250 km s^{-1}. The possible range of $v(r)$ due to distance uncertainties is delimited by the thin grey curves, which descend from a hypothetical ±20% uncertainty in $N_{HI}(r, \ell, b)$ model parameters.

ℓ, b (°)	h_R (kpc)	h_0 (kpc)	h' (pc kpc^{-1})	R_m (kpc)	w_{arm} (kpc)	$n_{local\ arm}/n_0$	$n_{0,arm}/n_0$
90.23, 1.72	2.0	0.18	35	9.73	0.83		1.3
93.3, 6.9	2.85	0.2	36	-	-	0.3	-
103.72, 2.18	2.3	0.18	30	9.63	0.67		0.6
105.77, −0.15	2.2	0.21	35	9.39	0.50		1.6
107.0, 5.4	2.9	0.2	30	10.50	0.5	1.2	0.5
110.11, 0.05	2.9	0.22	30	9.30	0.25	1	2
111.89, 0.88	2.9	0.2	30	9.38	0.3	1.2	1.9
113.52, −0.57	1.9	0.19	35	9.35	0.53		1.8
115.79, −1.65	2.0	0.21	35	9.43	0.55		2.2
138.3, 1.56	2.5	0.2	35	9.84	0.66		1
Mean	2.5	0.2	33	-	-	-	-
σ	±0.4	±0.01	±3				

Table 5.2: $N_{HI}(r, \ell, b)$ model parameters allowed to vary in each fitting to the corresponding observed H I data. Only h_R, h_0, and h' should be approximately constant with differing directions ℓ, b. The value for the heliocentric distance at which the Galactic Warp begins was fitted towards ℓ=93.3°, b=6.9° (final value r_w=2.1 kpc), and this distance was assumed to be circular about the Galactic centre for the other directions. Fixed parameters were R_0= 7.9 kpc, and $Z_\odot$=0.015 kpc. The values of $n_{0,arm}/n_0$ and $n_{local\ arm}/n_0$ are directly measurable for each ℓ, b. In each of these directions, the spatial parameters for the Local Arm are found to be very stable, with R_l=8.05 kpc and w_{local}=0.2 kpc.

5.4 The Results

Figure 5.4 shows one-dimensional velocity fields $v(r)$ towards the Galactic Plane in the range $90° \leq \ell \leq 140°$, $-1.7° \leq b \leq +7°$, which are representative of our findings across the second quadrant. Each field is plotted alongside those from two canonical rotation models: the Schmidt model (with R_0=10 kpc & $\theta_0 = 250$ km s^{-1}, Schmidt 1965), and the "flat" model, for which the field equation is:

$$v_{flat}(r, \ell, b) = \theta_0 \left(\left(1 + \frac{(r/R_0 - cos\,(\ell))^2}{sin^2\,(\ell)} \right)^{-\frac{1}{2}} - sin\,(\ell) \right) \tag{5.8}$$

and for Figure 5.4 we choose the constants from Merrifield (1992) as R_0= 7.9 kpc and $\theta_0 = 200$ km s^{-1}. It is important to remember that these fields show the *entire* velocity of H I towards the Sun, that arises from both circular and non-circular motions. A brief discussion of the general field characteristics follows.

5.4.1 The Local Velocity Field

It is observed for all directions (except toward $\ell = 90°$) that for $r \leq$1.5 kpc, the velocity field closely follows that given by the flat rotation model. Nearby "local arm" H I seems to obey flat circular rotation. These findings are consistent with the belief among many that kinematic distances which use a flat rotation curve (in this quadrant of the outer Galaxy) are generally accurate when the object is very nearby.

Let us estimate the Sun's orbital velocity about the Galactic Centre θ_0 using the approximation that very nearby H I has a similar orbital velocity, thus $\theta(R) \simeq \theta_0$ (in otherwords a flat rotation model is valid locally, for $R \sim R_0$). If we subscribe to Merrifield (1992) that the distance of the Sun from the centre of the Galaxy is R_0=7.9 kpc (a constant our model of $N_{HI}(r, \ell, b)$ uses), the local velocity fields (see Figure 5.4) can be used with Eqn. 5.8 to find the Solar velocity. A least-squares routine to fit Eqn. 5.8 to the nine separate $v(r)$ in Fig. 5.4 is performed for H I in the velocity range $-15 \leq v \leq$0 km s^{-1}. The value for parameter θ_0 is found that minimizes χ^2 with 18 degrees of freedom, under the constraint of R_0=7.9 kpc. From the nine fields across 50° longitude

range, a mean value of θ_0 =214±10 km s^{-1} is found, consistent with the very modern determination of Sackett (1997) of θ_0 =200±20 km s^{-1} and Knapp et al. 1978 (whose analysis suggests a value somewhere between 200 and 220 km s^{-1}). If we use R_0=7.2 kpc (a direct distance determination to the Galactic centre employing proper motions of H_2O masers, Reid 1993), then θ_0 =197±9 km s^{-1}. Note that a small R_0=7.1 ±0.4 kpc and θ_0 =184±8 km s^{-1} was also obtained by Olling and Merrifield (1998).

Measuring the Oort Constants Near to the Sun

The above analysis assumes flat circular rotation locally. Let us relax our requirements and backstep to the more basic assumption that the local field traces circular motions only. For objects in circular rotation, one relates Galactocentric distance R to the LOS velocity v by:

$$v = R_0 \left(\theta(R)/R - \theta_0/R_0\right) sin(\ell)cos(b) \tag{5.9}$$

where $\theta(R)$ is an object's circular speed about the Galactic centre. For local H I ($R \sim R_0$) we have the following approximation:

$$v \simeq -2A(R - R_0)sin(\ell)cos(b) \tag{5.10}$$

where $A = -1/2R_0 \left(d/dR(\theta(R)/R)\right)_{R=R_0}$ is the azimuthal shear (Oort constant) evaluated in the Solar neighborhood. Equation 5.10 is valid locally and therefore depends very little on R_0, and with $R^2 = R_0^2 + r^2cos^2(b) - 2R_0rcos(\ell)cos(b)$ it can be written as:

$$dv/dr \simeq Asin(2\ell)cos^2(b) \tag{5.11}$$

We use the above with each of our local fields in Fig. 5.4 (out to r ~1.3 kpc from the Sun) to calculate the local values of the azimuthal shear A and vorticity B, found via:

$$A - B = \theta_0/R_0 \tag{5.12}$$

Assuming R_0=7.9 kpc and using our value of θ_0 we arrive at error-weighted mean values of $A = 13.2 \pm 0.7$ km s^{-1} kpc^{-1}, and $B = -13.9 \pm 1.0$ km s^{-1} kpc^{-1}.

Reference	A (km s^{-1} kpc^{-1})	$-B$ (km s^{-1} kpc^{-1})	θ_0 (km s^{-1})
1	14.5±1.3	12.0±2.8	220±20
2	12.6	13.2	220
3	15.9±0.3		
4	14.8±0.8	12.4±0.6	231±15
5	11.3±1.1	13.9±0.9	184±8
6	15.9±1.2	16.9±4.6	
7	12.95	12.93	
This work	13.2±0.7	13.9±1.0	214±10

Table 5.3: Recent values of Galactic constants A, B and θ_0 near the Sun derived by various authors, and including the current work. References are (1) Kerr & Lynden-Bell 1986, (2) Brand & Blitz 1993, (3) Pont, Mayor & Burki 1994, (4) Feast & Whitelock 1997, (5) Hanson 1987, (6) Olling & Dehnen 2003, and (7) Allen & Santillan 1991.

These values compare favorably with the relatively recent measurements listed in Table 5.3. Note that a flat rotation curve gives $A + B = 0$, and Eqn. 5.12 becomes $2AR_0 = \theta_0$. Having made no initial assumptions of flatness, we nevertheless recover (for the local field) a nearly flat rotation model with our values for A and B, a quantitative demonstration that kinematic distances calculated with this canonical rotation curve are good distance estimates, albeit for local objects only.

5.4.2 The Velocity Field Beyond the Solar Neighborhood

In all fields, a pronounced deviation from the fields predicted by a flat rotation law and the 1965 Schmidt model is observed beyond about $r \sim 1.5$ kpc. H I beyond the interarm region appears at higher negative velocities than it otherwise should if a flat law was uniquely present. Beyond this region of sharp deviation the field thereafter continues roughly parallel with respect to the flat and Schmidt curves. Of key interest here is the region where the field shifts away from obeying a flat rotation law. This is possibly evidence for the Perseus Spiral Arm shock, (as predicted by Roberts 1972), where ISM gas is decelerated as it enters a spiral potential (see Fig. 5.5).

Uncovering the Spiral Shock Within...

We offer evidence that this breakaway is a shock phenomenon similar in properties to Robert's TASS model, but begininng at a different heliocentric distance. To compare to the TASS model, we choose the midplane direction $\ell = 110°$ similar to Roberts' selection in his 1972 work. In this direction H II region Sh156 is found in the middle of the Perseus Spiral Arm, the H I peak for which is 2.95 kpc distant. The arm stretches 1.4 kpc ($\pm 3\sigma$, where $\sigma = w_{arm}/\sqrt{2}$) along the line of sight.

In this direction Roberts places the shock ridge ~2.4 kpc from the Sun and with a potential well (the "velocity trough" in Figure 5.5) capable of affecting LOS velocities by +30 km s^{-1}. The velocity trough (from the shock ridge to the top of the "velocity hill") is where dense ISM gas compressed by the shock exists in a ~0.5 kpc wide region. Most optically visible objects (e.g. OB Galactic clusters, H II regions) should lie within the region of the velocity hill, having migrated away from the shock ridge which triggered their initial formation several million years ago.

We model a single-arm[1] shocked flat velocity field using Eqn. 5.8 in the following way:

$$v_{shocked}(r, \ell, b) = \begin{cases} v_{flat}, \; r < r_s \\ v_{flat} - v_s exp\left(-(r - r_s)/w_s\right), \; r \geq r_s \end{cases} \tag{5.13}$$

where v_s is the velocity displacement caused by the shock initially (the "depth" of the potential well), r_s is the heliocentric distance at which the shock ridge is found, and w_s is the LOS width of the region of shock-compressed ISM gas. For v_{flat} we choose $R_0 = 7.9$ kpc and $\theta_0 = 214$ km s^{-1}, values appropriate to the local field (see previous section). The shocked-flat field model is shown in Fig. 5.5. Gas moving in a circular orbit encounters the shock and is decelerated as it enters the spiral arm potential, which *increases* its apparent LOS velocity towards the Sun. Note that the shock creates a non-monotonic velocity-distance relation, where two or more kinematic distances are possible for a single velocity

[1]The two-armed spiral shock (TASS) model of Roberts is so-named as a double-peaked gas density distribution arises along the LOS from his models. The secondary peak is negligibly small relative to the primary, and we do not include it here.

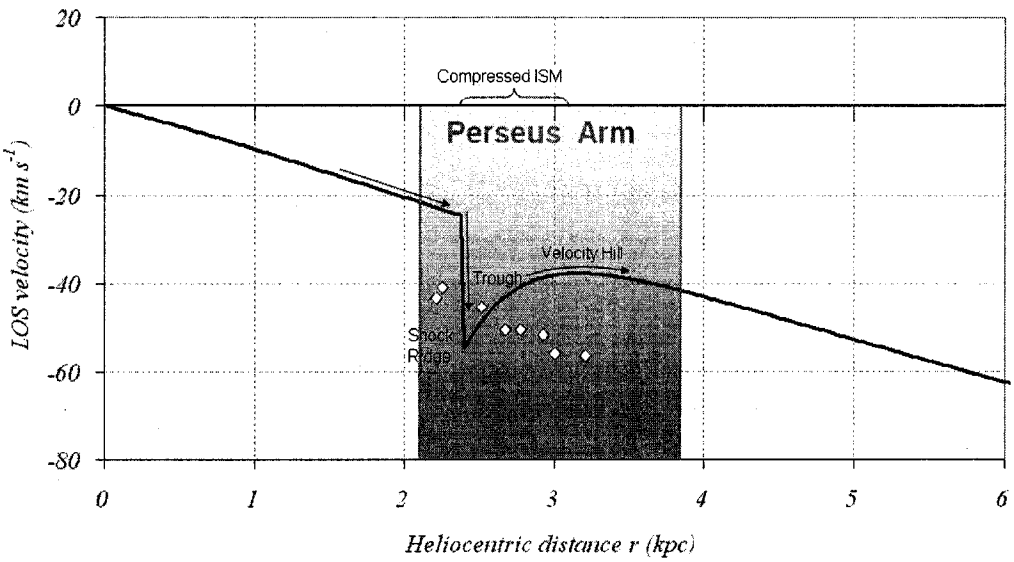

Figure 5.5: A model for a single-armed spiral shock towards $\ell = 110 - 115°$. The model is from Eqn. 5.13 with parameters that reproduce Roberts' $\ell = 110°$ TASS model. The direction of flow for gas in circular orbits is indicated. The H I Perseus arm as represented in the author's column-depth model toward $\ell = 110°$ is shown, and 8 H II regions towards this direction (from Table 2.2) are plotted (from left to right: Sh158, 159, 156, 152, 161, 163, 169 & 157). The optical arm and H I arm are one and the same.

(we discuss this ambiguity in a later section).

Is the shock to be found within our velocity fields? Indeed, the overall shape of the field from 0 km s^{-1} to just beyond the disturbance **is** consistent with a shocked flat model of rotation. To see this consistency, we unsharpen the relation between velocity and distance in the flat shocked model of Eqn. 5.13, by convolving it with a normalized Gaussian of width σ_r:

$$v'_{shocked}(r,\ell,b) = \frac{1}{\sqrt{2\pi}\sigma_r}\int_0^\infty v_{shocked}(r',\ell,b)exp\left(-(r-r')^2/2\sigma_r^2\right)dr' \qquad (5.14)$$

where σ_r is estimated as described for Eqn. 5.3. The appearance of our fields make it rather essential that the shock ridge occurs slightly closer to the Sun (r_s=1.8 kpc for $\ell = 110°$) than in Roberts' picture (2.4 kpc). This is also more con-

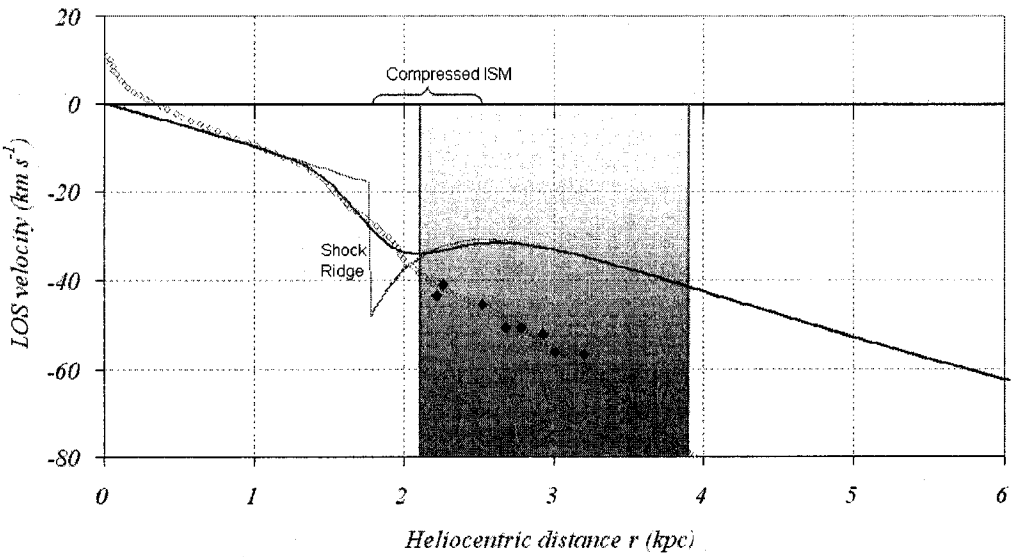

Figure 5.6: A single-armed spiral shock model convolved to introduce a fuzziness between distance and velocity (solid curve, Eqn. 5.14), and superposed with the predicted velocity field towards $\ell = 110°$, $b = 0.1°$ (open circles). The predicted field's shifting to higher negative velocities past 1.4 kpc is well explained by a spiral potential at 1.8 kpc, and a broadening (due to turbulent velocities) of σ_r =0.24 kpc.

sistent with the location of H II regions Sh158 and Sh159, which appear nearer than (and otherwise unrelated to) his 2.4 kpc distant shock ridge. Other parameters in $v_{shocked}$ remain unchanged from the original model (Fig. 5.5). Figure 5.6 plots $v'_{shocked}$ for longitude $\ell = 110°$. Excellent correlation is seen between the theoretical field and the predicted $v(r)$ in the region of deviation (1.4 kpc to 2 kpc). We conclude that a shock model *is consistent* with the shifting region observed in the predicted velocity fields of Fig. 5.4.

However, in the shock model, the post-shock field returns to obeying a undisturbed flat circular law, whereas our shifted field continues parallel to this unperturbed field. Our original assumption of a smooth monotonic velocity field does not allow for velocity reversals (to positive dv/dr), as would be the case if the H I returned to its pre-shock potential. However, there is observational evidence that the velocity structure in our fields does not abruptly reverse in the

manner of Fig. 5.5.

Consider for a moment the shocked flat velocity field in Fig. 5.7 towards Sh161 (ℓ=111.9°, b=0.9°). If a shock ridge exists at the distance indicated, there should also exist reasonably dense compressed H I within the velocity trough ($v \simeq -45$ km s^{-1}). As well, if such a field adequately described the true field beyond $r = 2$ kpc and if H I is ubiquitously distributed, there should be an apparent H I density enhancement where the path length per unit velocity interval $|dv/dr|$ is near to zero, the situation found at $v \simeq -30$ km s^{-1}. Indeed, the H I absorption spectrum towards the bright radio continuum H II region Sh158 (ℓ=111.54°, b=0.8°) *does* show a strong absorption peak at -45 km s^{-1}, indicative of cool dense H I at this velocity. However, a lack of H I density at $v \sim -30$ km s^{-1} is seen in both spectra, suggesting that dv/dr does not approach zero and a velocity hill really is absent here. Further, if the velocity field actually returned to flat circular rotation, then objects that are well behind the shock (for e.g. those near $\ell = 93°$, described in Chapter 4) would exhibit higher positive velocities and kinematic distances more agreeable with their photometric distances.

The H I spectra for the fields in Figure 5.4 are consistent with a highly localized potential along the LOS, and an absence of a post-potential velocity hill. There is a conspicuous similarity between our velocity fields and the smoothed theoretical model of Eqn. 5.13 at the point of breakaway, good evidence that a shock ridge is present there. H II regions (with accurate distances and ^{12}CO velocities) are correctly seen within the post-shock ridge zone, and the "velocity trough" is coincident with dense compressed H I (seen in absorption).

It is observed that towards the lower longitude end, the distance to the shock ridge is farther away (e.g. 2.3 kpc towards ℓ=100°) than towards the higher longitude end (e.g. 1.4 kpc towards ℓ=138°) of the CGPS. The location of the ridge is remarkably consistent with the inner edge of the H I and optical Perseus Arm (see Fig. 4.11). Velocity fields from Figure 5.4 in the latitude range $-1.7° \leq b \leq 5.4°$ are shown together in Fig. 5.8. The amount of deviation from flat circular rotation is observed to be latitude dependent. The field towards b=5.4° exhibits only mild blueshifting (maximally $\sim$20 km s^{-1} beyond 6 kpc), however, directly toward the midplane (b=0.1° & b=$-$0.6°) the LOS velocity fields are severely blueshifted ($\sim$40 km s^{-1} at 6 kpc). This behavior suggests

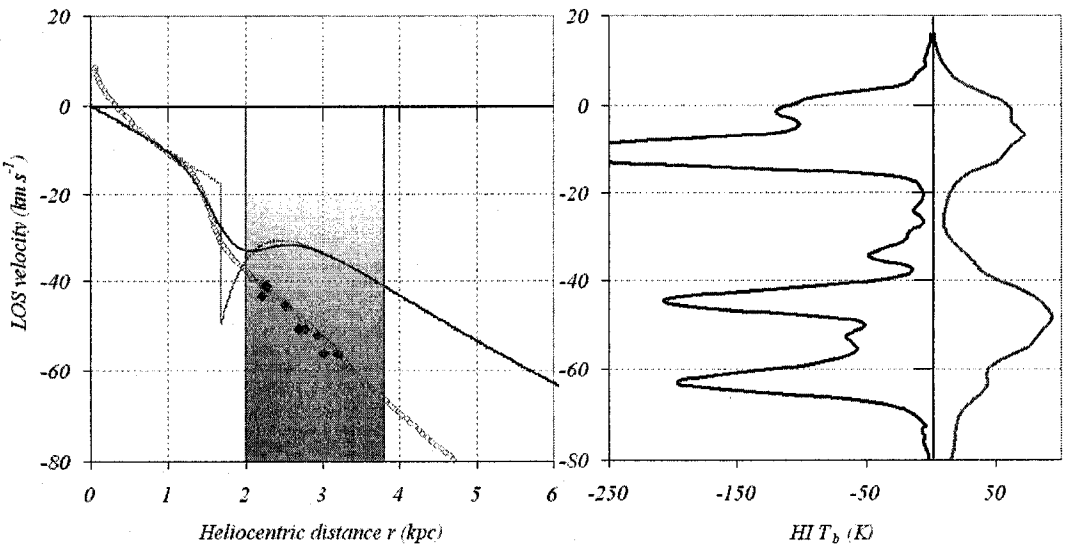

Figure 5.7: The velocity field together with H I emission and absorption spectra (right panel, from CGPS data) towards $\ell = 112°$, $b = 1°$. The shocked flat velocity field is the same as in Fig. 5.6, except that r_s=1.7 kpc. The Perseus Arm centre (2.9 kpc) and LOS extent (0.9 kpc) is again shown in the shaded region, along with the 8 H II regions. No H I is observed coincident with the velocity hill, suggesting that the shocked field does not return to an undisturbed flat field beyond $r \sim 2$ kpc.

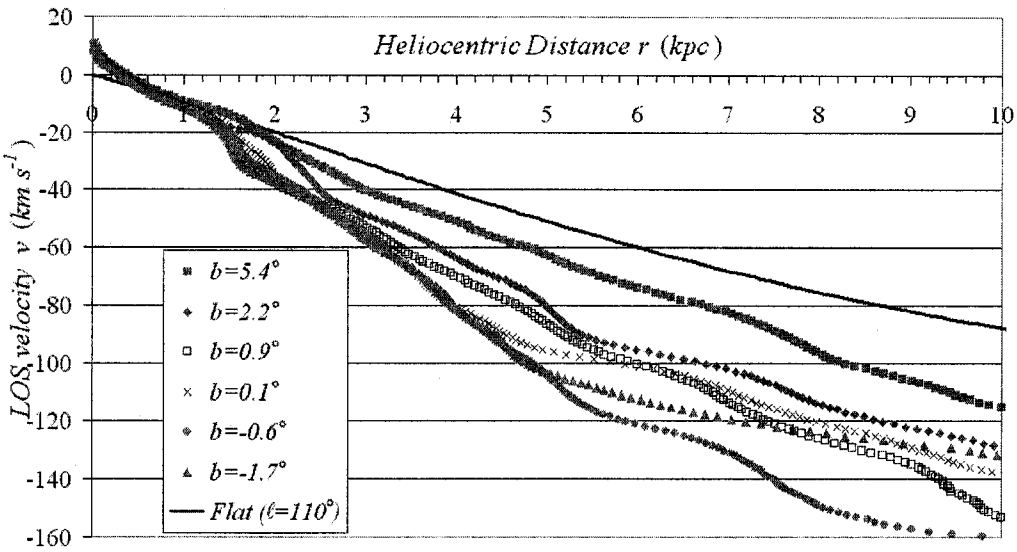

Figure 5.8: b-variation in $v(r)$ towards ℓ=105-115°. The solid black line is a flat circular rotation model (for ℓ=110°) with R_0=7.9 kpc, θ_0=200 km s^{-1}. Note the striking latitude dependence of the perturbation seen near r=2 kpc.

the causal phenomenon is concentrated in the plane, again consistent with a spiral arm.

It is thus concluded that a shock ridge precedes the optical & neutral hydrogen Perseus Arm in the outer H I disk. A flat velocity field with a single spiral shock (with constants R_0=7.9 kpc, θ_0=214 km s^{-1}, and v_s ~30 km s^{-1}) best describes our predicted fields out to r ~2 kpc or so. Beyond this area, the high negative velocities of relatively nearby H II regions and a lack of H I at the presumed location of the velocity hill are evidence that the true field does not actually return to the undisturbed flat model obeyed locally. More than just a "shocked" velocity field is observed here: a significant component of the velocity structure in the outer Galaxy may be non-circular in origin. The spiral shock appears to be *closer* than predicted by Roberts. This more forward location places most Perseus Arm H II regions in the post-shock region, consistent with their forming from this triggering phenomenon.

5.5 The Rotation Curve Beyond the Shock

If we believe that distant ($r > r_s$) H I gas (and H II regions) exhibit velocities that are purely descended from their circular motions, then they do not seem to completely recover from their encounter with the spiral potential. Far Outer Galaxy H I and H II regions do not return to the nearly flat rotation behaviour characteristic of the local gas. Instead, their LOS velocity seems to grow increasingly negative with distance in a fashion inconsistent with any sensical rotation curve. This is easily seen by assigning a power-law[2] to $\theta(R)$:

$$\theta(R) = \theta_0(R/R_0)^{-\alpha} \tag{5.15}$$

in Eqn. 5.9, and deriving values for α by fitting this rotation curve to $v(r)$, $r > r_s$ (for constants R_0 and θ_0 as in Sec. 5.4.1). One obtains (for $\ell = 110-115°$) $\alpha \simeq 0.85$, far from a flat model ($\alpha = 0$) and even a Keplerian model (α=0.5). We must conclude that our original assumption is in error, and the velocity of H I beyond $r = r_s$ has a significant non-circular component.

It is important to realize here that our velocity fields trace the *entire* LOS motion toward the Sun, both circular and non-circular (so-called streaming motions). Further, it is the non-random component of streaming motions that are traced (random motions are effectively averaged by the underlying method). These motions represent an extremely interesting dynamical property of H I, but were difficult to separate from circular motions until now. Fortunately we find that high-latitude velocity fields are relatively undisturbed, and allow us to calculate the "true" rotation curve, allowing separation of $v(r)$ into circular and non-circular components.

High-Latitude Fields

Lines of sight at a high galactic latitude ($b \geq 5.4°$) are significantly far from the plane and do not encounter most of the Perseus Arm material: thus, perturbations associated with this spiral arm are expected to be minimal. We make

[2]The power-law form for the rotation curve is found to adequately describe the observed rotational behaviour of most external galaxies, Knapp et al. 1978

the assumption that up here, velocities of H I more completely originate with the LOS component of the cloud's circular rotation. The velocity fields $v(r)$ towards these relatively high latitudes appear much more congruent with a reasonable rotation curve (Eqn. 5.15). In Fig. 5.4, the fields toward ℓ=93.3°, b=6.9°, and ℓ=107.0°, b=5.4° more closely obey the Schmidt model of Galactic rotation (R_0=10 kpc & $\theta_0 = 250$ km s^{-1}) than the flat model. A rotation curve that slowly declines through the outer Galaxy seems to better describe these fields.

One can see in Figure 5.9 that the field toward ℓ=93.3°, b=6.9° is well modeled by such a gently decreasing rotation curve of index $\alpha \simeq 0.13$. This field is high enough that the Perseus Arm is hardly encountered at all along the sight line (an outer spiral arm component for the density model $n(r, \ell, b)$ was not required for this direction, see Table 5.2). Fourteen degrees east, the field towards ℓ=107.0°, b=5.4° shows a slightly higher rate of decline ($\alpha \simeq 0.3$), a difference explained by its minor brush with the Arm (the effect of the shock ridge is somewhat visible in the velocity field near $r \sim 2$ kpc). We believe the velocity field near ℓ=93.3° is most free of streaming motions induced by the Arm, and use it to derive the circular speed curve in Figure 5.10. The quality of fit towards this direction is excellent (a velocity deviation $\sigma_{rms} = \pm 1.4$ km s^{-1} is found, see Table 5.1).

It is an important conclusion that *the rotation curve is not ideally flat in the outer Galaxy*, and is not rising as is the curve of Brand & Blitz (1993, hereafter BB93). Near R/R_0=2, the tangential speed has fallen to $\theta \sim 190$ km s^{-1}. This gives the dynamical mass of the Galaxy (to $2R_0$) as:

$$M = \frac{2R_0\theta(2R_0)^2}{G} = 1.33 \times 10^{11} M_\odot \tag{5.16}$$

assuming an axisymmetric disk. However, within our uncertainties we cannot rule out the curve of BB93, although the 20% estimate for uncertainty in r (shown at r=6 kpc in Figure 5.10) is probably on the high side of the true value.

Discussion of the Rotation Curve's Accuracy

It is also worthy of note that the author's method of calculating Galactic rotation is inherently more accurate than using outer galaxy H II regions (e.g. Brand &

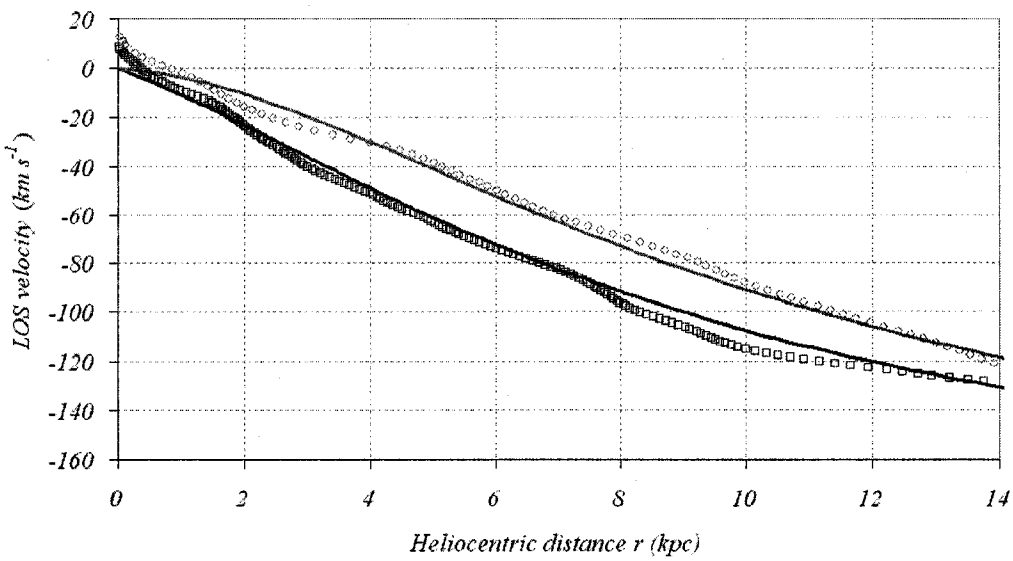

Figure 5.9: The velocity fields toward two high-latitude regions: $\ell = 93.3°$, $b = 6.9°$ (open circles) and $\ell = 107.0°$, $b = 5.4°$ (open squares). The power-law rotation model of Eqn. 5.15 has been fitted to each field, yielding a similar result: a non-flat rotation curve that shows tangential velocity θ decreases very gradually through the outer Galaxy.

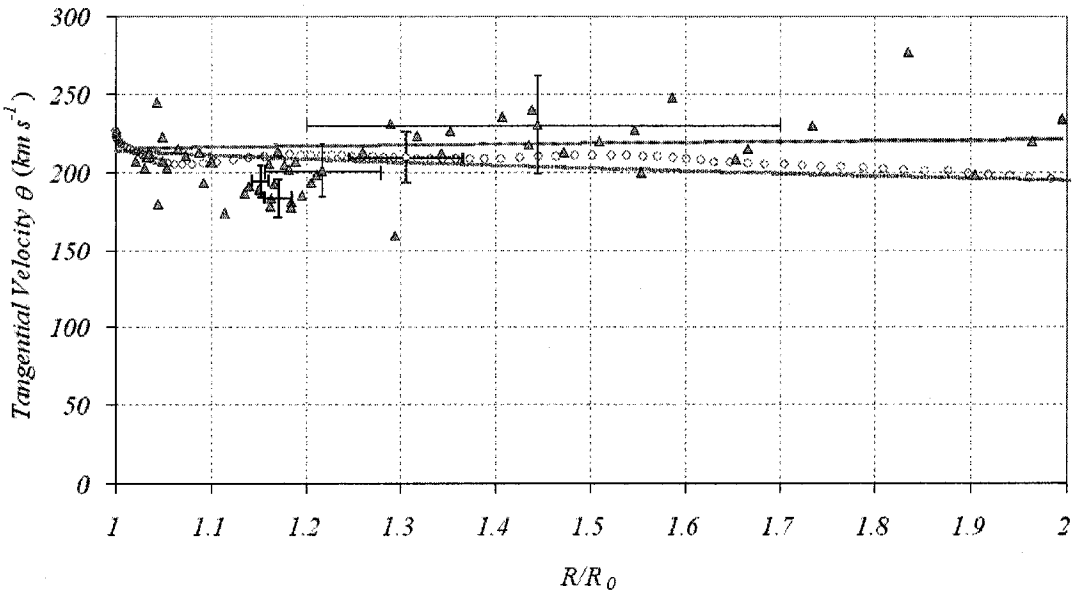

Figure 5.10: The rotation curve of the outer Milky Way Galaxy to $2R_0$, as derived from a high-latitude velocity field from this study ($v(r)$ towards ℓ=93.3°, b=6.9°, open circles). The Sun is at R/R_0=1 (where R_0 = 7.9 kpc) & θ_0 = 214 km s^{-1}. H II regions (triangles) and the rotation curve of Brand & Blitz (1993) are shown, scaled to match our Galactic constants (those authors used R_0=8.5 kpc & θ_0 = 220 km s^{-1}). The curve of BB93 rises slightly in the outer Galaxy (dark hatched line, $\alpha = -0.04$), while we find a gently declining curve of $\alpha = 0.13$ (grey hatched line, fitted to $v(r)$). To compare accuracy, for the H II regions Sh156 and Sh162 we show the coordinates and uncertainties from BB93 (for Sh156 R/R_0=1.44±0.3, $\theta = 230 \pm 31$ km s^{-1}, thin bars) along with those from the author's method (R/R_0=1.17±0.02, $\theta = 185 \pm 13$ km s^{-1}, thick bars). As well, the uncertainties in R & θ are shown for a point on our rotation curve (R/R_0=1.3±0.07, $\theta = 210 \pm 15$ km s^{-1}), derived from a hypothetical 20% uncertainty in heliocentric distance.

Blitz 1993, Fich, Blitz & Stark 1989). Besides displaying wild random motions, photometric distance errors to exciting stars can creep higher than 30% (affecting *both* θ and R). The rise in the curve of BB93 has been attributed to systematic distance errors that are a consequence of not accounting for the metallicity of these stars, which decreases through the Galaxy (Hron 1989). More recently, Binney & Dehnen (1997) argue that a rising rotation curve is a natural statistical result of noisy distances, and that a gently falling curve best describes the actual data. In any case, the current method avoids both problems, and calculates distances with smaller uncertainties (less than 20%, see Figure 5.10).

Two nagging quandaries remain, and should be briefly resolved for the reader. Firstly, although the underlying assumption of a smooth $v(r)$ somewhat cures our method of random (noisy) distance and velocity residuals, it is not entirely clear how this fundamental assumption of monotonicity affects the resulting velocity fields. As shown by absorption spectra (e.g. Kothes & Kerton 2002) in many directions, some H I that appears at high negative velocities is otherwise spatially in front of gas with more positive velocities (this H I is said to be "velocity-reversed"). Certainly, a shock-ridge should generate velocity reversals in H I spectra. However, the *area* ($\int T_b(v)dv$) under the emission profile of velocity-reversed H I would have to be a substantial fraction of the non-reversed emission to substantially affect $N_{HI}(v)$, and moderate deviations are ignored in the fitting procedure. Fortunately, *shocked* gas is often found to be velocity-reversed (e.g. shocked gas in shells around H II regions and in the spiral arm potential), and as shocked compressed gas is more likely to be optically thick, should not contribute strongly to emission profiles.

Secondly, a more pronounced source of systematic non-uniform motions is an apparent "rolling" motion exhibited by the Perseus Arm. Table 5.2 shows that towards the high latitude field ℓ=107°, b=5.4° the centre of the Perseus Arm is found to be 5 kpc distant from the Sun, whereas more mid-planar latitudes show it to be closer to 3 kpc. In Figure 5.11 a steep gradient in latitude is seen for the velocity centroid of the Perseus Arm. The arm appears to be rolling towards the Sun at high latitudes by about 10 km s^{-1} (thereby making it appear more distant at high-b). Given this effect, it is not surprising to find that distances to H II regions are also affected (see Figure 5.11). However, the effect is quite

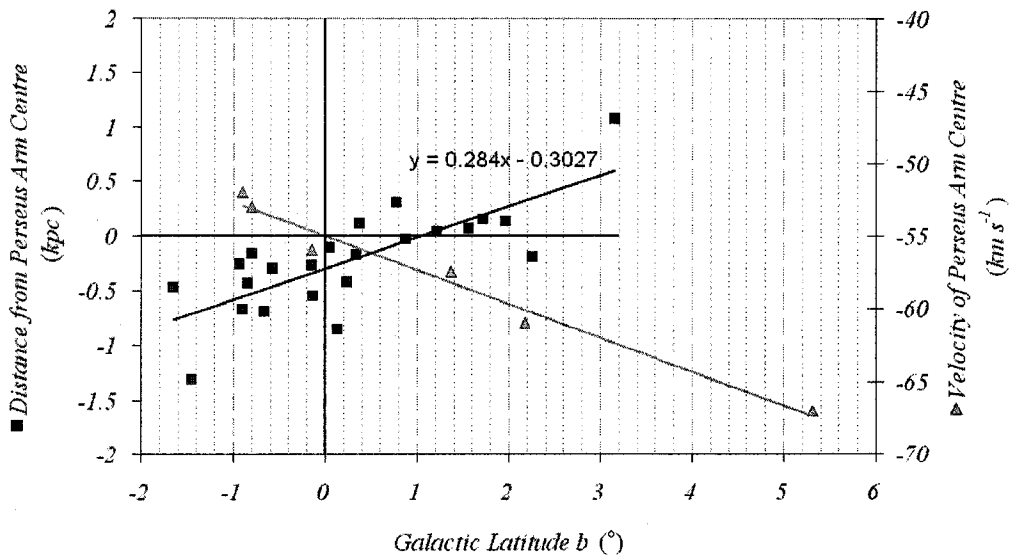

Figure 5.11: The distance of Perseus Arm H II regions from the Arm's centre (squares), and the velocity centroid of the Perseus Arm (for a constant longitude, triangles), both as a function of latitude b.

small (maximally ± 0.3 kpc per degree of latitude), and some of this may be an observational effect due to the upward warp of the midplane (where H II regions at negative latitudes would naturally tend to be closer to us).

Neither of the above issues significantly affects the rotation curve calculated from the velocity field towards $\ell = 93.3°$, $b = 6.9°$. This LOS avoids shock-related velocity reversed H I, and the non-uniform rolling motions associated with the Perseus Arm.

5.5.1 Non-circular Motions of Neutral Hydrogen in the Plane

The *velocity residuals* of the H I gas are defined as the observed velocity minus that expected from circular rotation. Since our individual fields are from spectra obtained over $\frac{1}{4}$ square-degrees of sky (a large angular patch of H I) toward individual directions (ℓ, b), we expect only the large-scale systematic component of non-circular motions to be present (the small-scale random components of each H I cloudlet in the $\frac{1}{4}$ square-degree patch of sky should average to zero).

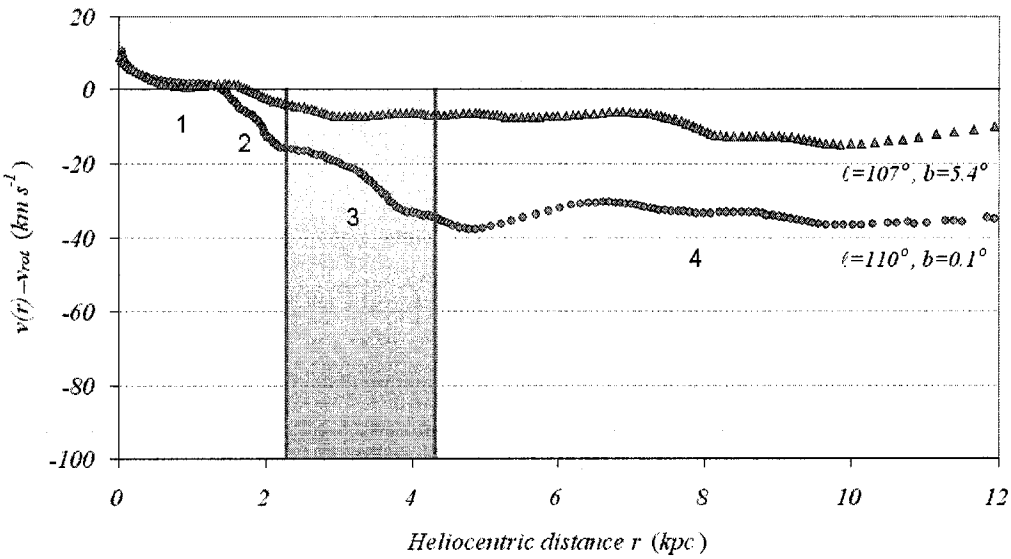

Figure 5.12: The systematic velocity residuals $(v(r) - v_{rot})$ as a function of distance r for two directions, one more directly into the plane than the other. Four distinct regions are labelled and described in the text.

We use our rotation curve to calculate these residuals, and plot the results for two directions in Figure 5.12.

Four regions of interest are labelled in our residuals figure. Region 1 is clearly where H I uniquely obeys circular rotation (shown in Sec. 5.4.1), and illustrates the flatness of $\theta(R)$ locally. Region 2 is distinctly defined as the location of the shock ridge where gas, moving with differential rotation, "catches up" with the spiral arm (which itself moves at a slower pattern speed) and is decelerated by the spiral potential. The third region in Figure 5.12 is coincident with the overlaid $\pm 2\sigma$ extent of the Perseus Spiral Arm (centred on $r = 3$ kpc, from Fig. 4.11), and shows a decline in the hydrogen's rotational speed (for H I in the plane). Finally, H I in the plane that has overtaken the Arm apparently recovers to near-flat differential rotation, but seems to retain a constant velocity "memory" from its experience with the Arm.

That there should be a velocity gradient *across* a spiral arm (Region 3) can be explained by H I streaming motions parallel to the Arm's axis, which according to Lin, Yuan & Shu (1969) are a dynamical result of the gravitational field of a

circular arm of concentrated matter. Consider Figure 5.13, which illustrates a qualitative model for our $v(r)$ fields that accounts for these systematic streams along the arm's edges. The flow of the H I due to streaming is *with* the general rotation pattern on the *outside* edge of the arm, and *against* the pattern on the *inside* edge.

The observed line-of-sight velocity field would appear as in the figure: H I is decelerated by the shock (A), shows a *continuing drop* in velocity inside the near-edge of the arm (B), somewhat levelling-off to (C) before a gradual return to near-flat circular rotation as the line-of-sight exits the arm. This model $v(r)$ is similar to the appearance of the predicted velocity fields, and suggests that Region 2 in Figure 5.12 is actually caused by the shock ridge plus streaming motions at the near-edge of the Perseus Arm. In this model, a shocked velocity field would not appear to return to normal circular rotation if it is immediately followed by an arm with non-circular streaming motions such as those drawn.

However, there is still the mystery of why H I in Region 4 is not observed to rejoin the near-flat differential rotation. According to a qualitative model by Burton & Bania (1974, Figure 17 in their paper) that is based on Roberts' shock model, stars that form from gravitational collapse of clouds triggered by the shock will kinematically *decouple* from the gaseous H I. The motions of these stars and their surrounding gas clouds retain the kinematic shift Δv they picked up from the shock ridge, and as long as they are not viscously dragged along by the gas, they continue in a circular rotation pattern, but with a velocity "residue" indicative of their shock-related formation. The stars and gas remain spatially correlated but in this model the interstellar medium (ISM) H I gas that leaves the shock resumes a non-shifted rotation pattern.

This conclusion of kinematic decoupling is inconsistent with our observations. However, Burton & Bania do concede that many interpretations of their findings are possible, and the above model remains qualitative and tentative. Should there be a kinematic correlation between H II and H I? Our model, which actually seeks a spatial and kinematic correlation, measures distances to H I clouds (with a given velocity) that are consistent with photometric distances to H II regions with similar velocities to the H I. The initial assumption of kinematic and spatial coincidence reproduces the independent photometric re-

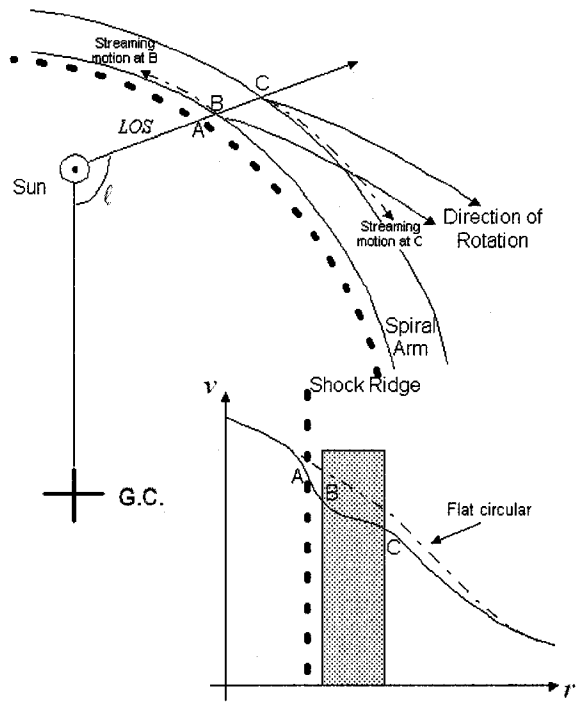

Figure 5.13: Cartoon sketch of H I streaming motions parallel to the axis of a spiral arm, as suggested by Lin et al. (1969). The Galactic Centre (G.C.) and the Sun's position are shown. This model traces a velocity field whose behaviour out to just past the spiral arm is similar to that observed in the author's predicted fields.

sults, and for this reason we can strongly argue that H I and H II remain coupled kinematically, even through the spiral arms.

5.6 Conclusions

It is likely then that more is going on in the Outer Galaxy, beyond the effects of a declining rotation curve and a single spiral shock. Whether or not the observed velocities of distant H I indeed derive from circular motions, the thin H I disk in this quadrant must be undergoing some intense shearing, as higher latitude H I does not appear to be undergoing similar motions to those of the gas closer to the plane. Certainly, the "rolling" motion of the arm is one example, and its relation to streaming motions must be investigated.

Nevertheless, this work has shown some exciting results. For the first time we directly observe the Perseus Arm spiral density wave from Roberts' 1972 prediction, and importantly conclude that the wavefront is closer to the Sun than predicted. The detail available in the velocity fields predicted by the author's method calls for future mapping of the shock and the spiral arm through this region of the Galaxy.

As well, we show that the velocity field near to the Sun is undisturbed by the shock, and that the local Oort constants are consistent with a near-flat rotation law in the solar neighborhood. Using high-latitude velocity fields, this rotation curve is derived out to a distance of $2R_0$ and is found to gently decline through the outer Galaxy. This curve underlies complex streaming motions of H I observed in the Galactic plane that are quite likely related to the Perseus Spiral Arm.

Bibliography

[1] Allen, C., & Santillan, A. 1991, Rev. Mexicana Astron. Af., 22, 255

[2] Binney, J., & Dehnen, W. 1997, MNRAS, 287, L5

[3] Blitz, L., & Spergel, D. N. 1991, ApJ, 370, 205

[4] Brand, J. & Blitz, L. 1993, A&A, 275, 67

[5] Brand, J. 1986, Ph.D. Thesis, University of Leiden, Sterrewacht

[6] Burton, W. B., & Bania, T. M. 1974, A&A, 33, 425

[7] Diplas, A., & Savage, B. 1991, ApJ, 377, 126

[8] Feast, M., & Whitelock, P. 1997, MNRAS, 291, 683

[9] Fich, M., Blitz, L., & Stark, A.A. 1989, ApJ, 342, 272

[10] Foster, T., & Routledge, D. 2003, in ASP Conf. Series Milky Way Surveys, eds. D. Clemens & T. Brainerd (San Francisco: ASP)

[11] Foster, T., & Routledge, D. 2003, ApJ, 589

[12] Hansen, R. B. 1987, AJ, 94, 409

[13] Hron, J. 1989, A&A, 222, 85

[14] Kerr, F. J., & Lynden-Bell, D. 1986, MNRAS, 221, 1023

[15] Kothes, R., & Kerton, C. 2002, A&A, 390, 337

[16] Knapp, G. R., Tremaine, S. D., & Gunn, J. E. 1978, AJ, 83, 1585

[17] Kulkarni, S. R., & Heiles, C. 1988, in Galactic and Extragalactic Radio Astronomy, eds. G. L. Verschuur & K. I. Kellermann, Springer-Verlag, New York, 95.

[18] Lin, C. C., Yuan, C., & Shu, F. H. 1969, ApJ, 155, 721

[19] Mebold, U. 1972, A&A, 19, 13

[20] Merrifield, M. R. 1992, A.J., 103, 1552

[21] Olling, R. P., & Dehnen, W. 2003, ApJ, submitted

[22] Olling, R. P., & Merrifield, M. R. 1998, MNRAS, 297, 943

[23] Pont, F., Mayor, M., & Burki, G. 1994, A&A, 285, 415

[24] Press, W., Teukolsky, S., Vetterling, W., & Flannery, B. 1992, Numerical Recipes in C, Cambridge University Press, New York

[25] Reid, M. J. 1993, ARA&A, 31, 345

[26] Roberts, W. 1972, ApJ, 173, 259

[27] Sackett, P. D. 1997, ApJ, 483, 103

[28] Schmidt, Maarten. 1965, in Galactic Structure, eds. Adriaan Blaauw & Maarten Schmidt, The University of Chicago Press, Chicago, 513

[29] Taylor, A. R., Gibson, S. J., Peracaula, M., Martin, P. G., Landecker, T. L., Brunt, C. M., Dewdney, P. E., Dougherty, S. M., Gray, A. D., Higgs, L. A., Kerton, C. R., Knee, L. B. G., Kothes, R., Purton, C. R., Uyaniker, B., Wallace, B. J., Willis, A. G., & Durand, D. 2003, AJ, 125, 3145

[30] Wouterloot, J. G. A., Brand, J., Burton, W. B., & Kwee, K. K. 1990, A&A, 230, 21

Chapter 6

Conclusions

6.1 Review and Future Directions

The work in this dissertation describes a new neutral hydrogen mass model for the outer Galaxy, and the development of this model into an original and accurate distance method and into a new tool for uncovering the dynamics of H I gas beyond $R = R_0$. The method is based on the premise that there exists a function relating increasing distance with decreasing LOS velocity, an assumption that must be true of the second quadrant H I if circular motions are the dominant source of observed LOS velocities. The possibilities for further study of the Outer Galaxy using the methods established herein are remarkably broad. The following are avenues of future research that exist in the author's mind at the time of this writing.

The work in Chapter 5 is beginning to reveal the first-ever direct observations of the Spiral Shock as Roberts (1972) described it, confirming this thirty year old theoretical model. The author's velocity fields suggest the shock ridge is moderately closer to the Sun than predicted. As well, some velocity fields show evidence for multiple shock ridges along the line of sight (e.g. $\ell = 103.7°$, $b = 2.2°$, see Fig. 5.4), the more distant one perhaps indicating the Outer Spiral Arm extends into the second quadrant (see Fig. 1.1). Much remains to be done with these exciting new observations.

The new work on the rotation curve is not finished either. Other high-latitude velocity fields from across the second quadrant would help to more firmly establish the curve calculated toward $\ell = 93.3°$, $b = 6.9°$ (Fig. 5.10). Chapter 5 has shown that the H I method of the author is a better way to proceed with Outer-Galaxy rotation studies than with individual H II regions. The high-latitude extension of the CGPS II ($100° \leq \ell \leq 117°$ reaching to $b = +18°$) will make available the data necessary for this project.

Certainly, an avenue that must be explored is the non-circular dynamics of H I through the plane of the Outer Galaxy. It is clear from this study that H II regions indeed show a velocity imprint from their involvement with the shock, as suggested by the qualitative model of Burton & Bania (1974). H I gas that precedes the Perseus Spiral Arm also exhibits behavior consistent with a spiral potential, but H I that has passed through the Arm seems to retain a significant

non-circular component to its velocity, and remains spatially and kinematically coupled with the H II. This is a surprising result that suggests H II regions are not readily separable from their large-scale H I environments. Further investigation into the cause of this behavior is clearly called for.

As the warping of the Milky Way's disk is most prominently visible in surveys of H I, the author's method is naturally suited to investigating the form of the Galactic Warp spatially. Fig. 6.1 demonstrates this idea towards $\ell = 90°$, using the author's cubic-function velocity field toward this direction (see Figure 5.3) and value for r_w (the heliocentric distance at which the midplane begins to bend) to transform Eqn. 2.5 into velocity-space. Excellent correlation is seen in the plane (to $b = 3°$), beyond which the velocity field from $b = 1.7°$ does not work. The gently declining rotation curve of Fig. 5.10 (Eqn. 5.15 with R_0=7.9 kpc, θ_0=214 km s^{-1} & α=0.13) works very well for higher latitudes $b \geq 5°$. The remapping demonstrated here, though somewhat simplistic (a single velocity field does not necessarily apply to the range of latitudes shown), demonstrates the potential for spatial studies of the warped H I disk of the Outer Milky Way.

I have shown the importance of the new distance method to studies of individual objects. One can now find distances to individual objects for which alternative distance methods are unreliable (e.g. supernova remnants), and there is no shortage of such objects in new high-resolution surveys like the CGPS. The study of the H I shell around SNR 3C434.1 (Chapter 3) is so very complete *because of* the independence and correctness of its distance measurement (for example, the discovery of the stars responsible for the bubble's formation, and deduction of the spectral type of the SNR progenitor would not have been easy with a kinematic distance approach).

On a somewhat larger scale, the distribution of extinction A_V and its correlation with the total hydrogen column $N_{HI} + 2N_{H_2}$ is now a more tractable study. An intriguing possibility exists for study of the large-scale spatial distribution of *dust*, via the total dust column found from N_H =H I+^{12}CO (which is shown to be proportional to extinction A_V towards $\ell = 93°$). The proper distances to molecular clouds (traced by ^{12}CO) are now more accurately calculable, and a better understanding of the relationship between these clouds and stars (through stellar distances and reddenings) can perhaps be found.

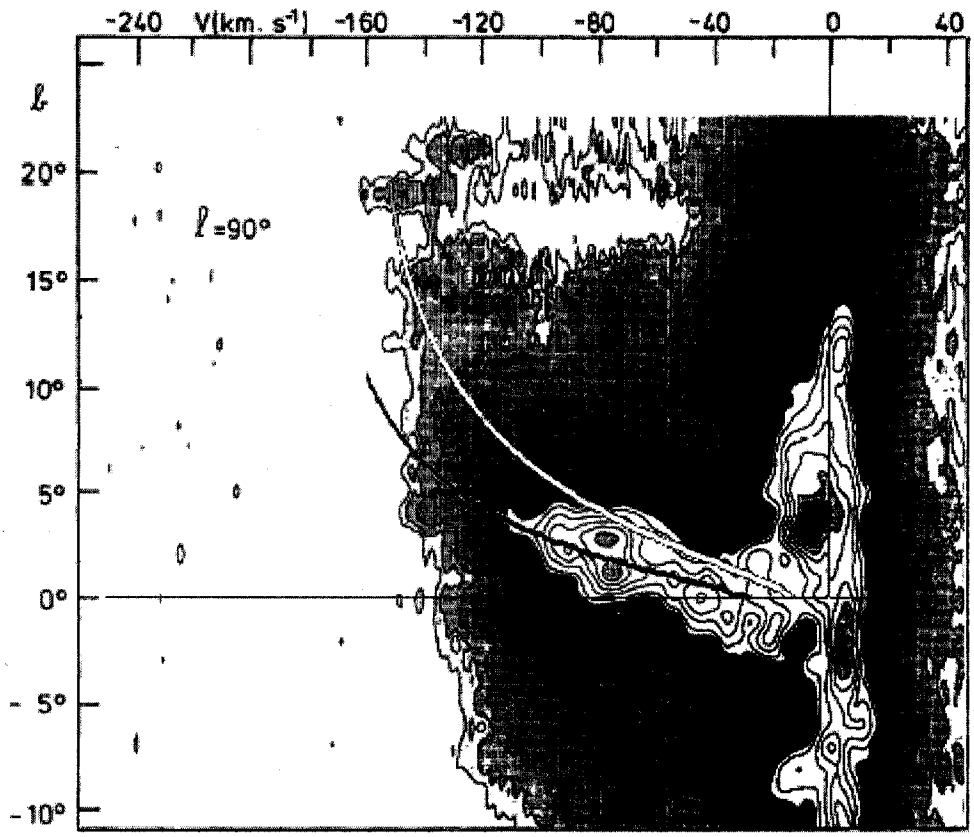

Figure 6.1: A latitude-velocity (b, v) plot of the H I distribution towards $\ell = 90°$, from the survey of Burton (1985) with the 140-ft NRAO Greenbank telescope. The warping of the midplane is plainly visible. Overlaid is a remapping of the form of the Warp (dark curve, Eqn. 2.5) using a single velocity field towards $\ell = 90.2°$, $b = 1.7°$ and r_w=2.5 kpc. The correlation is excellent out to $b \sim 3°$, $v \sim -100$ km s^{-1}. The equation for the Warp is also shown remapped by the author's rotation curve (light curve, Eqn. 5.15), which somewhat more poorly represents H I close to the plane ($b \leq 5°$), but traces the Warp remarkably well beyond.

The author sincerely hopes that the significant contribution to Galactic structure and physics contained in this thesis, and future work on projects descended from this will continue to help make great advances toward the goals of the Canadian Galactic Plane Survey, and other projects that endeavor to understand our origins ultimately through study of the interstellar medium of our Galaxy.

Bibliography

[1] Burton, W. B. 1985, A&A Suppl. Series, 62, 365

[2] Burton, W. B., & Bania, T. M. 1974, A&A, 33, 425

[3] Roberts, W. 1972, ApJ, 173, 259